Theory and Experiments on
Unstable-Resonator and
Quantum Well GaAs/GaAlAs Lasers

Thesis by

Michael Mittelstein

In Partial Fulfillment of the Requirements

for the Degree of

Doctor of Philosophy

California Institute of Technology

Pasadena, California

1989

(submitted March 3, 1989)

II

III

Acknowledgements

My deep and sincere gratitude goes first of all to Professor Amnon Yariv, my research advisor, who provided an environment for me to learn, to experiment, to develop, and to invent what led to this thesis and to my scientific and personal growth during these years. He provided me the freedom to expand. I could always obtain his keen advice to guide me. Sharing his scientific intuition and his profound knowledge in physics and research has been highly inspiring. I also want to thank the organizations that have provided support for the research in Dr. Amnon Yariv's quantum electronics group, of which I was a beneficiary.

My appreciation goes to my colleagues, who contributed so much to the joy of working at Caltech and who made possible the team efforts that produced or contributed to the innovative research results. Special thanks go to Dr. Joseph Salzman for introducing me to the basic skills of semiconductor laser fabrication, to Anders Larrson for providing the material and close collaboration for the early quantum well laser experiments, and to David Mehuys for being an enduring partner in grinding out many fragments so that the overall picture became clear in some of our research, and for the hundreds of hours of discussions and inspiring conversations.

The following list of coworkers is long but it does not even include all of the colleagues with whom I had stimulating discussions; I want to thank all of them: Dr. Robert J. Lang, Dr. Venky (T.) Venkatesan, Dr. Yasuhiko Arakawa, Haila Wang, Dr. T.R. Chen, Yu-Hua Zhuang, Ya-Yun Liu, Majanto Kajanto, Dr. Pamela L. Derry, Joel Paslaski, Harold A. Zarem, Dr. Kerry J. Vahala, Dr. Hadis Markoç, Howard Z. Chen, Ali Ghaffari, and, more recently, Lars Eng, Thomas Schrans,

Steve Sanders, and Bin Zhao, as well as Dr. Kam-Yin Lau, Dr. Nadav Bar-Chaim, Dr. Rona Sarfaty, and Jeffery E. Ungar of Ortel Corporation. In this thesis only a fraction of these collaborative efforts is presented.

I thank Desmond Armstrong not only for ordering and maintaining all the equipment which was used but also for his valuable suggestions and for building some of the electronic equipment that I designed. And I thank Jana Mercado for her invaluable help, and for her always encouraging words.

I would like to thank Claude H. Adams, Marty Gould, Dana Roth, L. Bruce Kahl, and Linda L. Dozsa and many others for providing support in the various facilities at Caltech. I also want to thank the people who supported me in Germany and in applying at schools in the United States before I came here. In particular, I thank Professor Dr. Hans Günter Danielmeyer, and Professor Dr. Fritz Peter Schäfer.

I am grateful to my parents for providing me with the fundamental skills that have enabled me to advance to this level, and to my mother for her continued encouragement. Finally I thank my wife, Dr. Soheila Mirhashemi, for her unfailing support, love and all the time and effort she put into editing the many versions through which this thesis evolved.

Dedication

to my father

Dr. Rainald Mittelstein

1924-1975

VI

Abstract

Structures of GaAs/GaAlAs lasers and their performance characteristics are investigated experimentally and theoretically. A self-consistent model for the longitudinal gain and intensity distribution in injection lasers is introduced. The model is applied to unstable-resonator semiconductor lasers to evaluate their lateral losses and quantum efficiencies, and an advanced design is presented. Symmetric, unstable-resonator semiconductor lasers are manufactured and a virtual source point inside the laser more than an order of magnitude narrower than the width of the near field is demonstrated. Young's double-slit experiment is adopted for lateral coherence measurements in semiconductor lasers. A high degree of lateral coherence is found, indicating operation of the unstable-resonator lasers in predominantly one mode.

In the pulsed measurements on broad-area, single-quantum-well, graded-index wave-guide, separate-confinement-heterostructure lasers, very high quantum efficiencies, very low losses, and very high output powers are observed. The devices are found to exhibit beam divergence narrower than two times the diffraction limit in single-lobed, far-field patterns. Using these single-quantum-well lasers, the "second quantized-state lasing" is found experimentally, and a simple model is developed to explain it.

A general model for the gain spectrum and required current density of quantum-well lasers is introduced. The eigenfunctions and eigenvalues of the charge carriers and optical mode of the transverse structure are used to derive the gain spectrum and current density from the Einstein coefficients. The two-dimensional

density of states for the charge carriers and the effective width of the optical mode (not the width of the quantum well) are identified as the dominant parameters. The model includes a new heuristic approach to account for the observed smeared onset of subbands, eliminating convolution calculations.

Applications of the model for a typical structure, a conventional double heterostructure and an advanced structure are presented. Structures providing two- and three-dimensional confinement are discussed and are directly compared to conventional and quantum-well structures in terms of laser parameters. The length scale of confinement structures for the optical mode is found to be two orders of magnitude larger than the corresponding length scale for carrier confinement, implying that the single-quantum-well laser is the most adapted structure.

The gain-flattened condition that single-quantum-well lasers exhibit near the onset of the second quantized-state lasing is introduced. An external grating-tuned resonator is analyzed, and the coupled cavity formalism is employed to examine conditions for continuous tuning. Predictions for tuning ranges of conventional, double-heterostructure and single-quantum-well lasers are made, and the superiority of the latter on account of pump current density is clarified. Experimentally, broadband tunability exceeding a 10% spectral tuning range of an uncoated quantum-well laser in a simple grating-tuned resonator is demonstrated.

VIII

Table of Contents

Chapter 6: Gain Spectra of Quantum-Well Lasers

Chapter 7: Gain Calculations of Semiconductor Lasers

Chapter 8: Semiconductor Lasers with an External Tuning Resonator

Chapter One

1: Introduction

1.1 Terminology and Background

The first part of the theoretical foundation of lasing was discovered by A. Einstein in 1916. The interaction of radiation and matter treated as a two-level system was discussed, and the concept of *stimulated transitions* from the energetically higher level to the energetically lower level was introduced. Adding the concept of *inversion* (larger population of the higher level with respect to the lower level) completes the basic requirement for *light amplification by stimulated emission of radiation (LASER)*. Inversion is a nonequilibrium condition (otherwise, the corresponding temperature would be negative). Inversion is reached in steady state by *pumping*. Pumping involves one or more *extra levels*, which are energetically higher than the upper or lower than the lower level. These extra levels are coupled to their adjacent level for fast relaxation. Then an energetically upward transition between the outer levels by an outside agent (pumping) allows inversion for the pair of originally considered levels to be established.

If a resonator is added, the light amplification by simulated emission of radiation can be used to achieve oscillation (output without input). Following the common terminology used in the semiconductor laser community, the word *"laser"* is assigned to laser oscillators, and the word *"laser amplifier"* is assigned to devices that do not oscillate.

A *semiconductor* is a material with a medium-wide *bandgap* (0.5 to 2.5 *eV*). At zero temperature, the bandgap separates the last-filled electron states (called *valence-band states*) from the unoccupied next higher electron states (called *conduction-band states*). Room-temperature thermal excitation, therefore, will result in a low density of electrons in the conduction band and a corresponding low density of vacancies of electrons in the valence band. For the vacancies in the valence band, the particle picture of *holes* has been introduced; this concept originates from P.A.M. Dirac. If the electrons make up a sea (a liquid in a gravitational field) and there is some perturbation on the surface, then elevated droplets of the liquid as well as downward "elevated" bubbles have excess potential energy with respect to a flat surface without perturbation. The *energy scale* for holes in the valence band is, therefore, *inverted* with respect to the energy scale of the electrons in the conduction band; this concept is consistently used in this thesis.

The intraband relaxation is much faster than the interband relaxation (about the order of a *ps* versus a *ns*); therefore, the intraband distribution will be nearly thermal. Only thermal contributions will be considered. Consequently, the two bands can be decoupled with respect to the thermal distribution. Under steady-state pumping conditions, individual a *"quasi-Fermi level"* for each of the two bands is introduced.

A convenient property of the semiconductor lasers is that they can be pumped directly with electric current at low voltages. A p-n junction is introduced so that electrons as well as holes are *injected* into the active region of the crystal. A *direct* bandgap semiconductor is required for efficient lasing transition. The direct bandgap is defined by having the energetically lowest electron and hole states at the same position in *k-space*. The two popular semiconductors, silicon (Si) and

germanium (Ge), have an indirect bandgap. However, *gallium arsenide* (GaAs), indium phosphide (InP), indium arsenide (InAs), and indium antimonide (InSb) are examples of direct bandgap materials. The GaAs/GaAlAs system is considered in this thesis.

In the case of injection lasers, the density of electrons and holes in the active region is made so large that inversion is achieved between the band edges. Therefore, lasing can take place by stimulated recombination of an electron with a hole across the bandgap, where the excess energy is radiated in the form of an additional photon.

After the first demonstration of laser action in 1960, the theoretical prerequisite for lasing in semiconductor material was clarified (specifying the inversion condition). The first semiconductor lasers were GaAs p-n junctions pumped with very high current density at low temperature. The principal deficiency of these devices was poor carrier and optical-mode confinement. The idea of using a heterostructure was put forward; its implementation, however, had to await advances in material science and growth technology of the crystals. The *conventional double heterostructure* became the standard structure for semiconductor laser production, once the technology was mastered. Basically, a three-layer sandwich was implemented with a central layer of lower bandgap, higher index of refraction material to provide carrier confinement and optical-mode guiding simultaneously. The implementation of the double-heterostructure technology was an evolutionary step that allowed the semiconductor lasers to advance from a laboratory study object to an industrial product for numerous applications such as communication and data storage and retrieval. The number of semiconductor lasers produced per week is now comparable to the total production of all other lasers combined.

1.2 Outline

In this thesis, some of the structures of semiconductor lasers and their performance are explored. The GaAs/GaAlAs system is investigated, but most of the findings are applicable to other semiconductor materials, as well. In *Chapter 2*, the theoretical model of unstable resonators is reviewed and applied to semiconductor lasers. A self-consistent, nonlinear saturation model is developed to predict high output power and good quantum efficiency for advanced unstable-resonator structures. In *Chapter 3*, the suppression of filaments in conventional double-heterostructure lasers was experimentally demonstrated by applying an unstable resonator. The concept of the virtual source point inside the unstable-resonator, semiconductor laser is verified experimentally. The application of a modified Young's double-slit experiment is introduced to measure lateral coherence in broad-area semiconductor lasers and is applied to verify improvements that are due to an unstable resonator. In *Chapter 4*, the record-breaking performance of broad-area, single-quantum-well lasers is presented. Extremely high differential and absolute quantum efficiencies as well as very low internal losses have been measured. Far-field patterns of these broad-area lasers have been found to be below twice the diffraction-limited width. In *Chapter 5*, the concept of the second quantized state lasing of quantum-well structures is introduced, and experimental results supporting the discontinuous transition towards shorter wavelength emission of injection lasers are presented. In *Chapter 6*, a detailed theoretical model of quantum-well lasers is presented. The gain spectra and associated pump current densities are derived from the Einstein coefficients. It is made clear that the gain and current density depend on the two- (not three-) dimensional density of states and on the effective width of the optical mode (not quantum-well thickness). A heuristic treatment accounting for the observed smooth gain spectra is introduced. In *Chapter 7*, the quantum-well-laser model is applied

to several structures: The popular parabolic-graded index structure with a single quantum well, a conventional double heterostructure, and an advanced wide-optical mode with a narrow and deep single-quantum-well structure are investigated. The current density of 0-, 1-, 2-, and 3-dimensional quantum confined laser structures are compared. The requirement for carrier confinement and optical-mode guidance via material-dependent scaling laws is examined. This scaling law implies that the single-quantum well is a highly optimized structure. In *Chapter 8*, broadband tuning of semiconductor lasers is investigated. It is clarified that quantum-well lasers are superior to double-heterostructure lasers in providing wide gain spectra on account of pump-current density. The second quantized state transition can be utilized to provide a gain-flattened condition, which is particularly desirable. Experimentally, broadband tuning is demonstrated with a simple external-grating-tuned cavity exceeding 10% tuning range.

1.3 Units

Basically, international units (SI, MKS) are used. Following the dominant usage in the semiconductor laser community, some compromises are made; namely, the length unit of cm and correspondingly the unit for gain coefficient $\frac{1}{cm}$ are used. For small lengths, the angstrom is used ($1\ \text{Å} = 10^{-10}\ m$), while the unit nm is reserved for wavelength. For photon energies and related potentials, the energy unit eV is used frequently ($1\ eV = 1.6021 \cdot 10^{-19}\ J$).

For tables and figures, variables divided by their units are specified; consequently, the entries are pure numbers.

2: Theory of Unstable-Resonator Semiconductor Lasers

Abstract

The spreading of the output beam and the ultimate ability to focus the light of an unstable resonator are discussed. The limit of ray tracing is defined, and Siegman's formulae for the geometric paraxial approximation of unstable resonators are introduced. The strip, rather than disk geometry, as it applies to unstable-resonator semiconductor lasers and the concept of magnification are clarified.

The lateral losses of unstable-resonator semiconductor lasers are accounted for using a new, self-consistent model, which is introduced to derive the quantum efficiency of these devices. Comparison with simpler theories indicates that a self-consistent model is necessary to avoid gross overestimation of the performance of these devices. Finally, an advanced design is presented, which (with its optimized parameters and a spherical output facet) holds promise for greatly improved performance in the future.

2.1 Introduction

Unstable resonators were considered shortly after the invention of the laser [1-3]. It was first used to increase the spatial dimension of the optical mode in solid state lasers, since large optical-mode, stable resonators are very sensitive to perturbations. These resonators are unstable in the sense that upon round-trip propagation through a fully transparent medium and reflection off ideally reflecting mirrors, the initial light is not reproducing itself. Rather, the *intentional spreading*

of the light causes a fraction of the reflected beams to miss the reflector and to be lost. The portion of the light missing the reflector is used as the output of resonators of this design in the majority of applications. It should be stated that the above-mentioned criterion is to a very small degree unintentionally fulfilled by all resonators because of diffraction. The difference is that the intentional spreading in the unstable resonators is significant; it can be described by a parameter *magnification*, which is most easily done in the ray-tracing model as described in the following section.

Large, stable resonators possess (in the linear theory) small filling factors; the high-intensity portion of the beam occupies a small fraction of the volume of the amplifying medium [3]. Unstable resonators force the mode to occupy most of the gain volume by spreading out the beam at the expense of higher losses. As a result, the sensitivity to perturbations is reduced (small additional spreading is insignificant), and at an operation well above threshold, the efficiency increases.

2.2 Geometric Theory, Ray Tracing

The lateral dimensions of unstable-resonator semiconductor lasers reported up to date are around 100 μm, which amount to a few hundred wavelengths in the material, since the wavelength in the material λ is close to 1/4 μm. The fundamental effect of diffraction is an uncertainty in the direction of propagation. This uncertainty in angle $\Delta\alpha$ depends on the width, W, of the underlying beam:

$$\Delta\alpha = \lambda/W \tag{2.1}$$

Therefore, geometric optics is a good approximation as long as the interpretation involves specifying angles only to a precision $\Delta\alpha$. Actually, the size of operational,
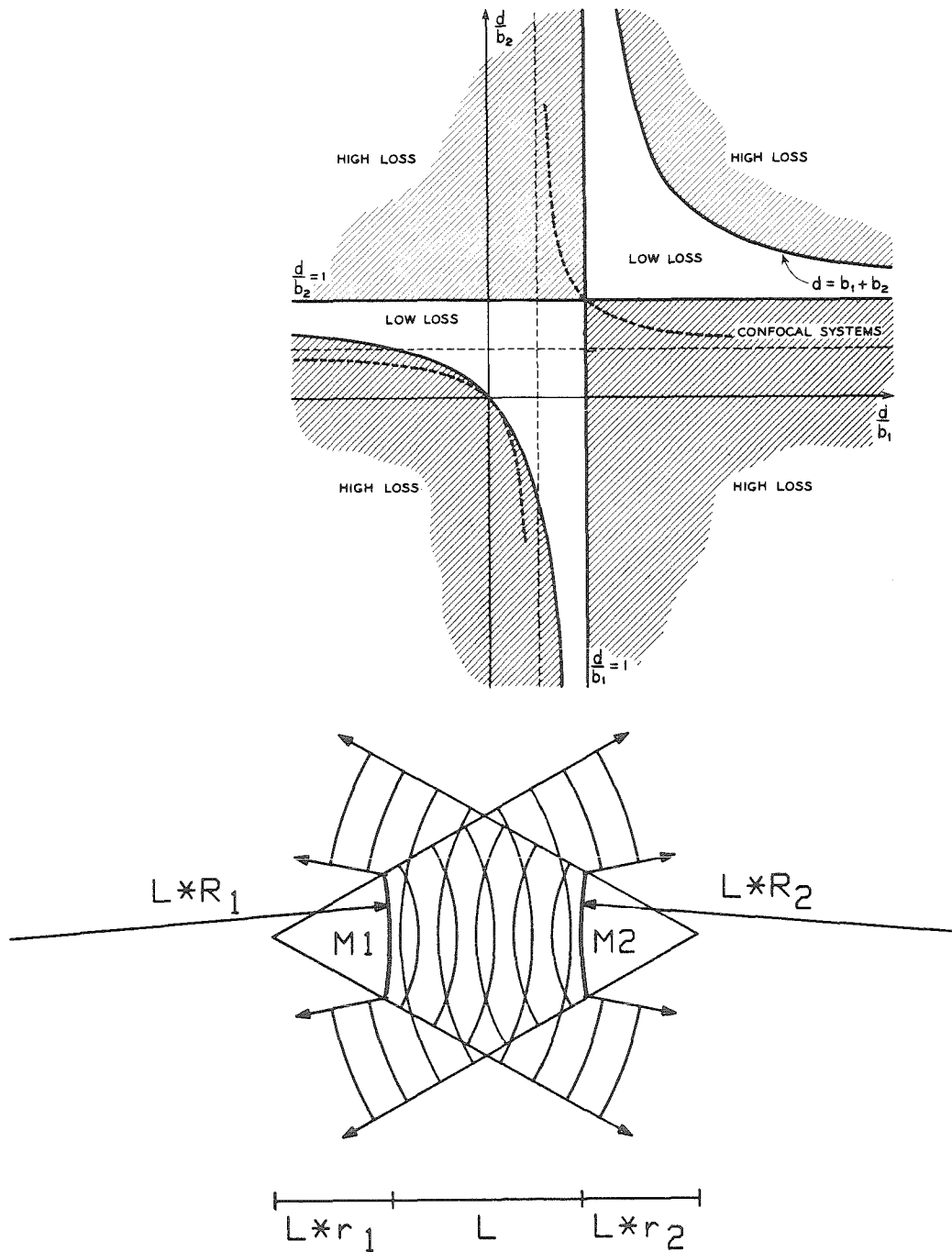
Figure 2.1 (a) Confinement diagram for optical resonators [Ref. 2, page 1364]. The shaded part of the parameter space presents unstable resonators (high loss). The nomenclature used in this thesis for this parameter space is $1/R_1, 1/R_2$. (b) presents a specific unstable-resonator semiconductor laser design and an introduction to the variables r_i, R_i and L, here called $(d/b_1, d/b_2)$.

unstable-resonator semiconductor lasers allows the geometric optics theory to provide a good estimate and an intuitive picture of their operation. It should be noted that the angles involved tend to be large, so the *paraxial approximation* of a Gaussian beam treatment has at least the same magnitude of error as the "geometric optics" picture, and in addition fails to identify some of the properties altogether.

First, the relevant formulae from the geometric theory of unstable resonators as presented by Siegman [4] will be given. One example of an unstable-resonator geometry is shown in *Figure 2.1* together with a diagram indicating the whole range of possible unstable resonators. All dimensions are normalized to the distance along the optical axis between the two mirrors, L, the length of the resonator. In the paraxial treatment, the two mirrors M_1 and M_2 are taken as circular, with radii R_1 and R_2, respectively; and the counterpropagating beams are assumed to have spherical (circular) phase fronts (lines) with virtual sources located at relative distances r_1 and r_2, respectively, measured outward from the two mirrors. The established theory of spherical-mirror resonators characterizes such a resonator by a set of g-parameters,

$$g_i = 1 + \frac{1}{R_i} \tag{2.2}$$

and the sign of R_1, R_2 is defined as positive for the curvatures shown in *Figure 2.1b*. To simplify the algebra, a set of h-parameters is defined by

$$h_i = \frac{1}{g_i} = \frac{R_i}{1 + R_i} \tag{2.3}$$

Self-consistency requires that the virtual sources of waves 1 and 2, at r_1 and r_2, respectively, are imaged onto each other after reflection in the opposing mirror [4]. This leads to

$$r_1 = \frac{\sqrt{1 - h_1 \cdot h_2} - (1 - h_1)}{(1 - h_1) + (1 - h_2)} \tag{2.4}$$

where the positive square root is meant. Exchanging the indexes 1 and 2 gives the expression for the other virtual source location.

The original unstable-resonator theory was for *strip* (i.e., 1-dimensional, that is, cylindrical) mirrors, although the major applications were to *disc* (2-dimensional, that is, spherical) mirrors. Semiconductor lasers exhibit a strong transverse waveguide structure implemented by means of the layer structure, for which the separated solution can be found, so that the problem is equivalent to the cylindrical mirror case. Therefore, the 1-dimensional mirror theory applies.

For a laser with mirrors of lateral width a_1 and a_2, the fraction of energy emitted from one mirror that subtends the opposite mirrors is in paraxial approximation for a uniform beam emitted from mirror 1:

$$|q_1|^2 = |\frac{a_2 \cdot r_2}{a_1 \cdot (r_1 + 1)}| \tag{2.5}$$

Exchanging the indexes 1 and 2 gives the expression for the beam emitted from mirror 2. Consequently, the fraction of energy that remains in the cold cavity (full transparency and total reflection are assumed) after one round trip is

$$|q|^2 = |\frac{r_2 \cdot r_1}{(r_2 + 1) \cdot (r_1 + 1)}| = |\frac{1 - \sqrt{1 - h_1 \cdot h_2}}{1 + \sqrt{1 - h_1 \cdot h_2}}| \tag{2.6}$$

where $|q|^2 = |q_1|^2 \cdot |q_2|^2$. The expression inside the absolute signs on the right-hand side of *Equation (2.6)* may be negative; this feature is indicative of an internal focal point within the resonator, a *negative branch* structure. The term *magnifications*, M, of an unstable resonator is a geometrical concept. The magnification in this context is defined as the relative change in size after one round trip. The magnification defined via ray tracing is a well-defined quantity and is related to the cavity losses as follows:

$$M_{roundtrip} = q^{-2} \tag{2.7}$$

The *per-pass* magnifications are:

$$M_1 = q_1^{-2}$$

$$M_2 = q_2^{-2} \tag{2.8}$$

2.3 Quantum Efficiency and Optimized Resonator Design

The main effect of introducing an unstable resonator is to spread the light upon propagation, leading to an increased power flux away from the optical axis. Upon spreading, the intensity decreases in transparent media, and the possible losses in the lateral boundaries have to be considered. Consequently, the gain has to compensate not only for internal losses and the nonreflected portions of the optical mode but also for the spreading. The useful output is affected by the internal losses, the portion of the optical mode that propagates out of the laser, but does not contribute to the output beam and possible scattering losses. The last term is more significant in etched facet lasers than in conventional, double-cleaved lasers because of their inferior surface quality.

If some of the light is lost laterally, its amount can be determined accurately only if the lateral mode pattern and the relative longitudinal intensity are known. The lateral mode pattern can, in a zero-order approximation, be considered flat till it enters the guiding boundaries. The longitudinal intensity distribution can, in this approximation, be solved by requiring *self-consistency in the saturated gain*. A numerical model has been developed to calculate the saturated gain. The round-trip propagation can be computed if the intensity of the two counterpropagating beams is known. With some heuristic programming, iteration on the longitudinal intensity distribution leads to self-consistency; that is, the round-trip gain equals one, and the
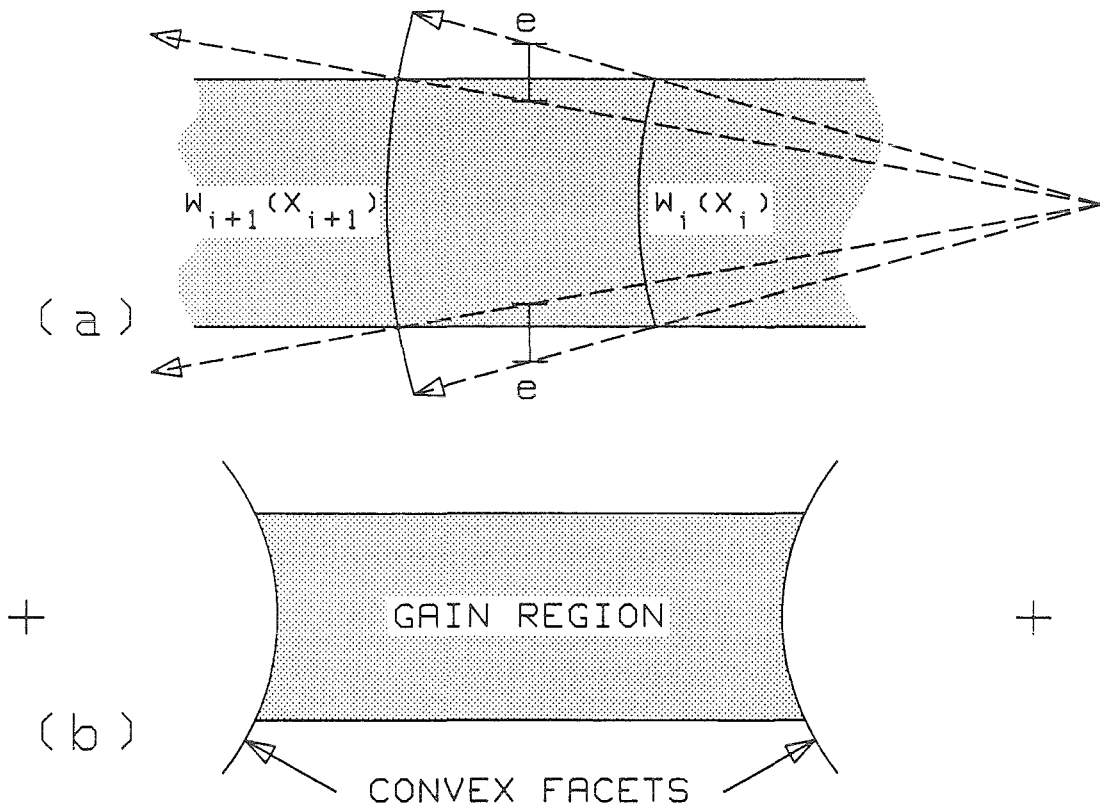
Figure 2.2 (a) Explanation of treatment of lateral losses in unstable-resonator lasers. Upon propagation from x_i to x_{i+1}, the leftward propagating beam spreads in width from w_i to w_{i+1} resulting in an excess width $2 \cdot e$. . The power accounted by $(I_i^{\leftarrow} + I_{i+1}^{\leftarrow}) \cdot e$ is considered dumped and does not contribute to the beam at x_{i+1}. (b) Scheme of symmetric unstable resonator with convex facets and a gain region of constant width.
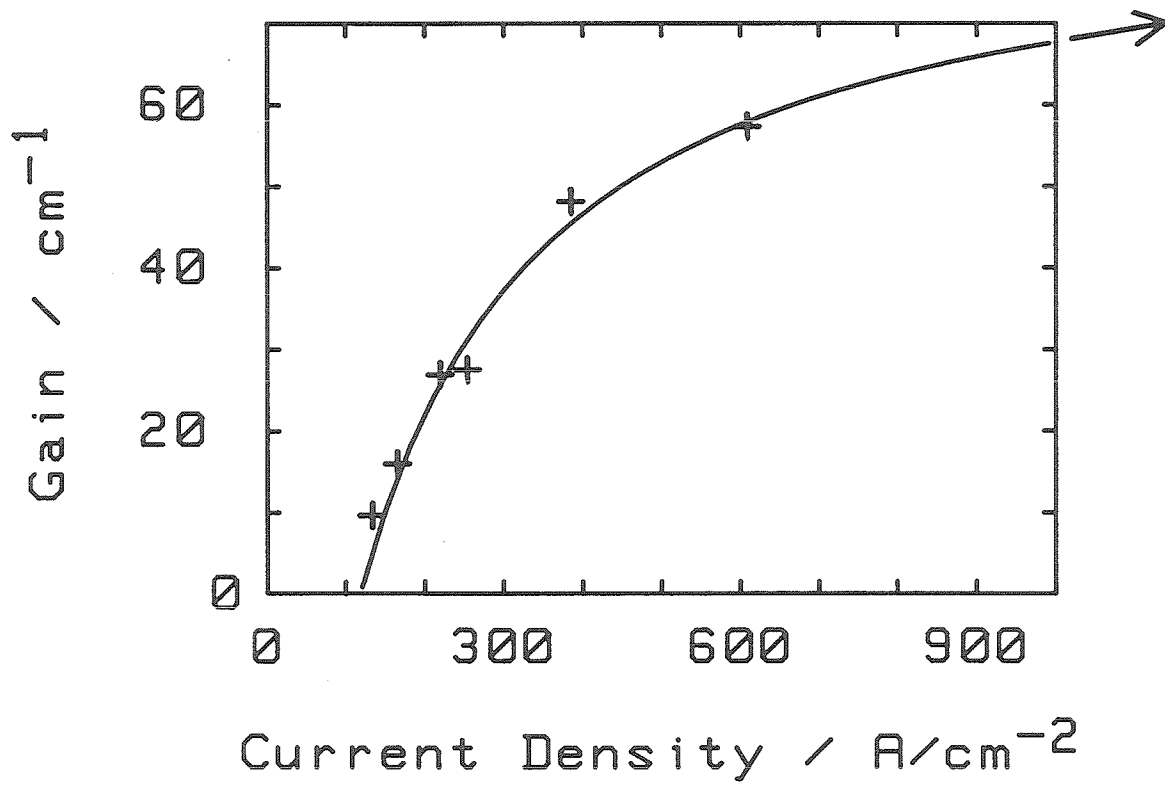
Figure 2.3 Gain vs. current density for the single-quantum-well structure described in *Chapter 5*. Crosses and the arrow to the right-hand side present measured values; a curve presents the analytical formula given by *Equation 2.9*.

local gain is the saturated gain given for the pumping current density and the local intensity of the two counterpropagating beams. In conclusion, the losses depend on the vertical and the lateral, as well as on the longitudinal structure.

In the model, the length of the resonator is divided into sections, each of which is considered to have a constant local gain, g. Spherical-phase fronts with no lateral-amplitude variation are used (in this case there are no diffraction effects, but the boundaries are not treated). Upon propagation, the radius of curvature increases as much as the propagation of the phase front on the optical axis, as is evident from *Figure 2.1b* and the definitions of r_i. The intensity is scaled down in inverse proportion to the radius of curvature. The gain is calculated, using the intensity of the two counterpropagating beams via the nonlinear saturation model as described below. The excess width of the phase front (as obtained by propagation starting from the actual width of the active region at the location before propagation), over the actual width of the active region at the location after propagation, is accounted for (see *Figure 2.2a*). The average intensity is considered dumped and lost laterally, not contributing to the output of the unstable-resonator laser.

The self-consistent, nonlinear saturation model is based on the measurements of threshold current density for different gain requirements as presented in *Figure 2.3* and discussed in *Chapter 5*. The current density, j_o, required to achieve gain, g, at the lasing wave length is fitted by the following expression for the single-quantum-well material:

$$g(j) = \frac{a \cdot j_o}{d + j_o} + b \tag{2.9}$$

with $a = 170 \; \frac{cm}{A}$, $b = -84 \; \frac{1}{cm}$, and $d = 120 \; \frac{A}{cm^2}$. This analytical formula fits the gain in the range of 20 to 60 $\frac{1}{cm}$ very closely. It expresses the observed gain flattening, the sublinear gain, current-density relation. Conventional saturation

models are based on an approximate linear gain versus pumping strength relation. They present a poor approximation for quantum-well lasers. Therefore, in this model, the fundamental equation for the saturated local gain is used:

$$j = j_o(g) + g \cdot C \cdot Q \qquad (2.10)$$

where j is the local injected current density; $j_o(g)$ is the current density consumed to establish the local gain, g ; C is a conversion constant, and Q is the total optical power per width at the lasing wavelength. The conversion constant is $C = \frac{e}{E_{ph} \cdot \eta_{in}}$, where e is the charge of the electron, E_{ph} is the laser photon energy, and η_{in} is the internal quantum efficiency. The second term expresses the portion of the local current density consumed to generate new photons via stimulated emission. Q is the sum of the counterpropagating optical power per width at the location of interest. *Equation (2.10)* can be used to find the implicit local gain, given Q and j as input parameters. Performing this procedure in a self-consistent manner and treating the facet reflectivity of the resonator allow the saturated gain profile along the laser cavity to be found.

In the first application of the model introduced above, a symmetric unstable resonator with convex facets of magnification M as shown in the diagram in *Figure 2.2b* is investigated. A constant width-gain region without additional lateral confinement with a conventional, double heterostructure is considered. Assumed is a scattering loss of S of the power approaching the facet, a power reflection of R and the balance, the power transmission of $1 - S - R$ and an internal quantum efficiency of η_i and distributed losses of α_i. A simpler model based on a cold cavity (no gain saturation, spatial independent gain) has been developed [5, 8, 9], and results for the case of $S = 0$ an $\alpha = 0$ cm^{-1} have been reported [8]. Their graph for $\eta_i = 1$, $M = 1$ *(g=1)*, $M = 4$ *(g=0.5)*, and $M = 25$ *(g=0.2)* is shown in comparison to the
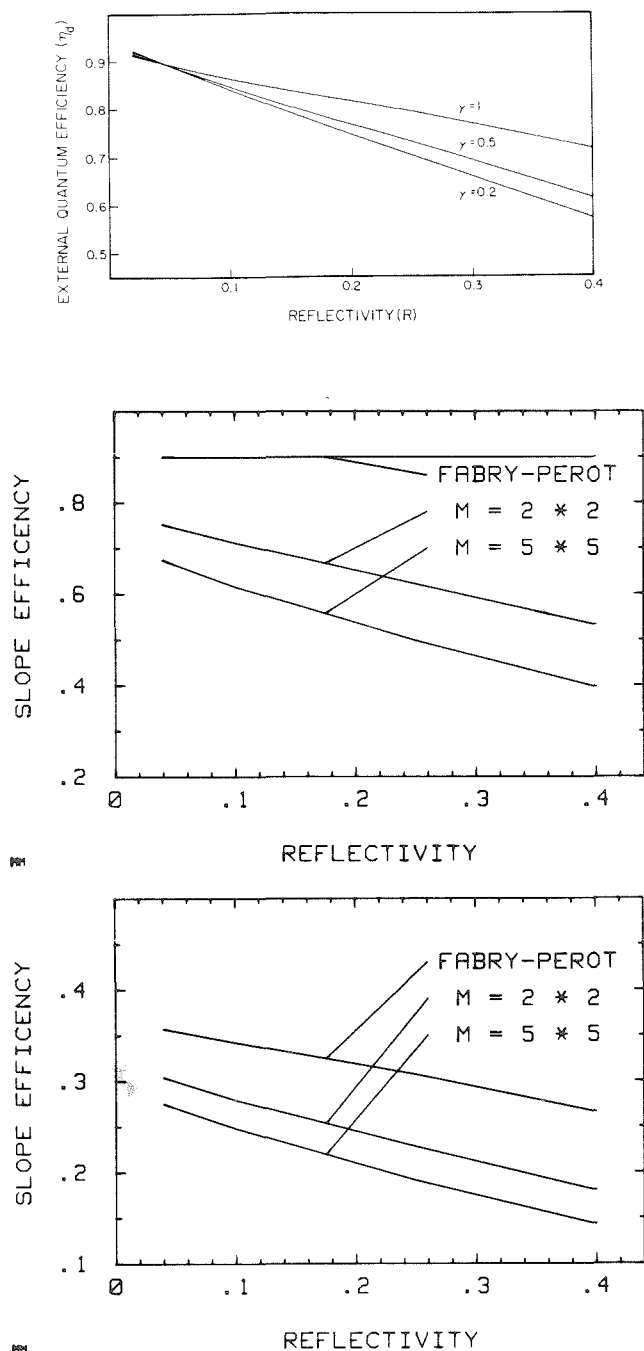
Figure 2.4 External slope quantum efficiency of symmetric, constant-width unstable-resonator semiconductor laser as a function of power reflectivity. (a) from Salzman et al. [8], for internal quantum efficiency (η_i=1) no scattering losses (S =0), and no distributed losses (α_i=0). (b) results from the self-consistent model introduced here for the same parameters as in (a), apart from η_i=0.9. (c) results from the self-consistent model for realistic parameters: η_i=0.9, S=0.1, α_i=15 cm^{-1}, and the scale is changed to efficiency per side.

results of the model presented here in *Figures 2.4a* and *2.4b*. More important is the bottom graph of *Figure 2.4c*; the case of $S = 0.1$ and $\alpha = 15\ cm^{-1}$ is presented. These values should be expected for a fairly high-quality, double-heterostructure material. In *Figure 2.4c*, the quantum efficiency per side is indicated as a more application-orientated measure, while the upper part of the figure gives the overall quantum efficiency, which is twice as high for this symmetric design. In conclusion, too simple a model is not very useful, since it overestimates the performance characteristic, quantum efficiency.

In the following, an advanced design is presented. For single-sided output a symmetric design is not favorable. Apart from the standard technique of low, reflective coatings on the output side and high, reflective coatings on the back side, the unstable resonator offers the option of *asymmetric magnification* in that the spreading in one direction is unequal to the spreading in the opposite direction. For instance, the confocal, positive-branch resonator of which a semiconductor laser version has been investigated [10] has no spreading upon propagation towards the output facet, that is, a single path gain of 1, like a double-cleaved, standard Fabry-Perot resonator. The spreading makes one more variation useful, that is, the absolute lateral width as a function of longitudinal position. The width of the active region can be increased with longitudinal position up to the amount of the spreading of the beam. For semiconductor, unstable-resonator lasers, it is worthwhile to investigate the possibility of one flat facet, because it could be manufactured by a cleaving process offering the very high-surface quality of conventional designs. All of these concepts are incorporated in the second example.

The second application of the self-consistent, unstable-resonator model is the case of a linear, tapered-width, gain region without additional lateral confinement in
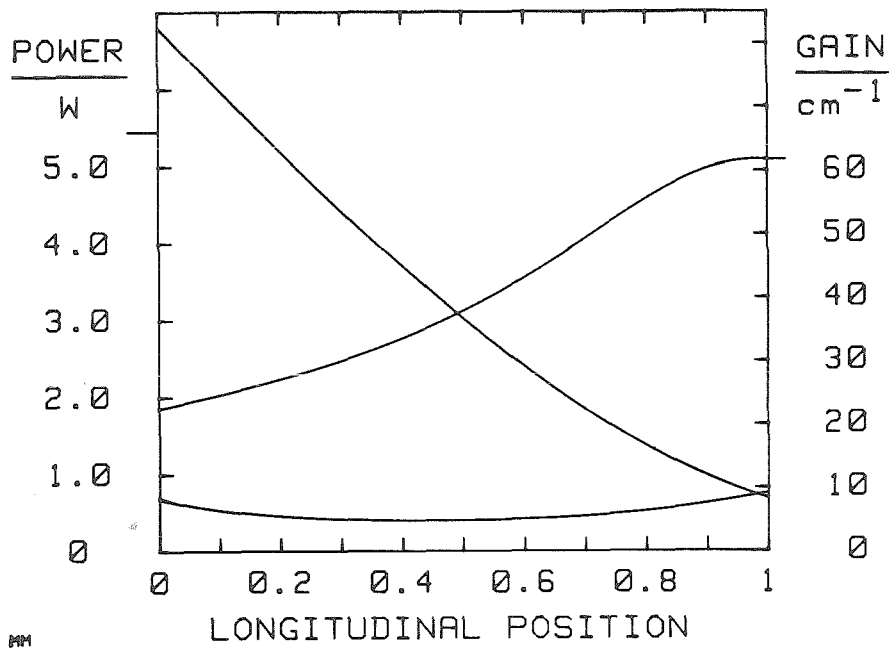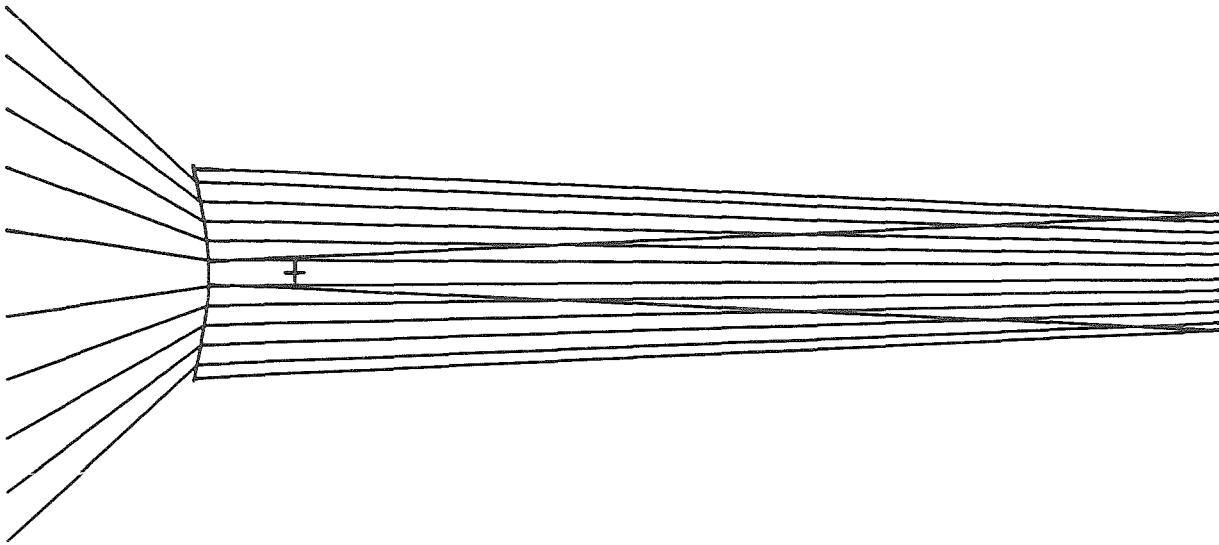
Figure 2.5 Optimized, unstable-resonator semiconductor laser (a) top view to scale. (b) intensity versus longitudinal position of the counterpropagating beams and (rising to the right) the local gain. The parameters are: width 100 μm, length 600 μm, taper ratio 1.8, magnification 9. Facets: left aspherical with central curvature 169 μm, right flat. Pump current is 6 A and internal quantum efficiency is 0.9. The reflectivity and the scattering losses are on the out-coupling side 0.1 and 0.1, and on the other side 0.9 and 0.02, respectively.

an asymmetric, unstable resonator (see *Figure 2.5a*) with convex output facets and a flat backside facet, a moderate round-trip magnification and a single quantum well, graded-index wave-guide, separate-confinement heterostructure (for details refer to *Chapter 4*). The taper is chosen to follow the spreading of the beam propagating towards the output facet. Consequently, the absolute lateral losses encountered for this propagation direction are equivalent to a conventional, broad-area laser, that is, very small. To keep the lateral losses for the other propagation direction small (relative to the intensity in the beam, the losses are large because the beam spreads out, while the width of the wave-guide decreases), the intensity of the backwards propagating beam is made as small as is practical by strongly asymmetric, facet reflectivity. The result is a substantially nonuniform gain caused by saturation by the nonuniform intensity distribution. The flat back facet makes a very high reflection feasible. The wider output facet reduces the relative intensity with respect to the average lateral width of the active region.

In an implementation, the output facet could be made aspherical to improve output beam geometry. An aspherical facet also eliminates the restriction posed on the width when spherical facets are used. In *Figure 2.5*, the longitudinal and lateral structure of the proposed resonator is illustrated in the top. The intensities of the propagating beams and the saturated gain, both as a function of longitudinal position, are shown in the bottom of *Figure 2.5*.

2.4 Conclusion

Fundamental concepts of unstable resonators are introduced. The properties of diverging output beams are analyzed. A new, self-consistent model for the quantum efficiency of unstable-resonator semiconductor lasers is introduced, and the

computed quantum efficiencies are much smaller compared to approximations derived from previous models. Finally, the new model is applied to a new structure to optimize the quantum efficiency, indicating that more than a 50% single-sided output can be achieved under realistic assumptions for the parameters involved.

2.5 References

[1]. Boyd G.D., and J.P. Gordon: *"Confocal multimode resonator for millimeter through optical wavelength masers."* Bell System Tech. J. 40:489-508 (1961).

[2]. Boyd G.D., and H. Kogelnik: *"Generalized confocal resonator theory."* Bell System Tech. J. 41:1347-1369 (1962).

[3]. Fox A.G., and T. Li: *"Modes in a maser interferometer with curved and titles mirrors."* Proc. IEEE 51:80-89 (1963).

[4]. Siegman A.E.: *"Unstable optical resonators for laser applications."* Proc. IEEE 53:277 (1965).

[5]. Salzman J., T. Venkatesan, R.J. Lang, M. Mittelstein, and A. Yariv: *"Unstable resonator cavity semiconductor lasers."* Appl. Phys. Lett. 46:218-220 (1985).

[6]. Salzman J., R.J. Lang, T. Venkatesan, M. Mittelstein, and A. Yariv: *"Modal properties of unstable resonators with a lateral wave-guide."* Appl. Phys. Lett. 47:445-447 (1985).

[7]. Salzman J., T. Venkatesan, R.J. Lang, M. Mittelstein, and A. Yariv: *"Erratum: Unstable resonator cavity semiconductor lasers with a lateral wave-guide."* Appl. Phys. Lett. 48:198 (1986).

[8]. Salzman J., R.J. Lang, and A. Yariv: *"Efficiency of unstable-resonator semiconductor lasers."* Electron. Lett. 21:821-823 (1985).

[9]. Wilcox J.Z.: *"Power characteristics of unstable-resonator cavity semiconductor stripe lasers."* Appl. Phys. Lett. 47:1019-1021 (1986).

[10]. Salzman J., R.J. Lang, A. Lars, and A. Yariv: *"Confocal unstable-resonator semiconductor lasers."* Opt. Lett. **11**:507-509 (1986).

Chapter Three

3: Experiments with Unstable-Resonator Semiconductor Lasers

Abstract

The historical background of the unstable-resonator semiconductor laser is reviewed, and the performance figures obtained are presented. The emission characteristics of unstable-resonator semiconductor lasers are measured. The output of an $80\mu m$ wide laser consists of a diverging beam with a *virtual source* $5\mu m$ wide located about $50\mu m$ behind the laser facet, in agreement with an analytical derivation. A high degree of spatial coherence of the laser output is measured, indicating single lateral mode operation for currents not exceeding three times threshold. In this chapter, additional measurements aim at showing that the unstable-resonator, semiconductor-laser radiation consisting of a diverging, single lateral mode is presented that can, in principle, be focused into a spot of about, or smaller than, $5\mu m$ diameter.

3.1 Introduction

In semiconductor lasers, the resonant cavity is generally formed by two flat, parallel mirrors. This Fabry-Perot cavity is easily produced by cleaving the crystal perpendicular to the optical axis. Such a resonator lies on the boundary between the stable and the unstable regions of the stability diagram of optical resonators (*Figure 2.4a*) [1]. However, the high, single-pass-gain capability of semiconductor lasers suggests that an unstable-resonator cavity may be advantageous, since this

cavity provides a large mode volume and in its conventional applications is known to provide a substantial discrimination against higher-order lateral modes [2]. Furthermore, the self-focusing behavior of lasing filaments can be counterbalanced by the magnifying effect of the cavity, making it possible to obtain higher-optical output powers.

The first attempts at fabricating unstable-resonator semiconductor lasers came in the late 1970s, when Bogatov et al. coated a string with abrasive and sought to grind a circular concavity into one facet of a broad-area laser [3]. The result was a hybrid of an unstable resonator with a broad-area laser (as only a portion of the facet was curved), which yielded a narrow far field superimposed upon a wide-board plateau. Although the mirror quality undoubtedly left something to be desired, the presence of the diverging perturbation appeared to stabilize the operation of the device.

The initial crudeness of the unstable-resonator semiconductor lasers was overcome by the introduction, in 1984, of chemical etching and standard photolithographic technique in the production of the curved laser facets [4, 5, 6]. Both unstable-resonator semiconductor lasers reported consisted of a normal, broad-area double heterostructure with a resonator exhibiting either one diverging mirror and one planar mirror [4, 5] or two diverging mirrors [6]. The powers reported were of the order of hundreds of mW under pulsed conditions. Since that time, further refinements and more sophisticated geometries have been reported [7, 8], suggesting that unstable resonators may indeed be useful alternatives to arrays in high-power devices. They possess an additional attraction in that the etched mirrors are fully compatible with optoelectronic integration.

Preliminary experiments with semiconductor lasers, in which one mirror was

(a)

(b)
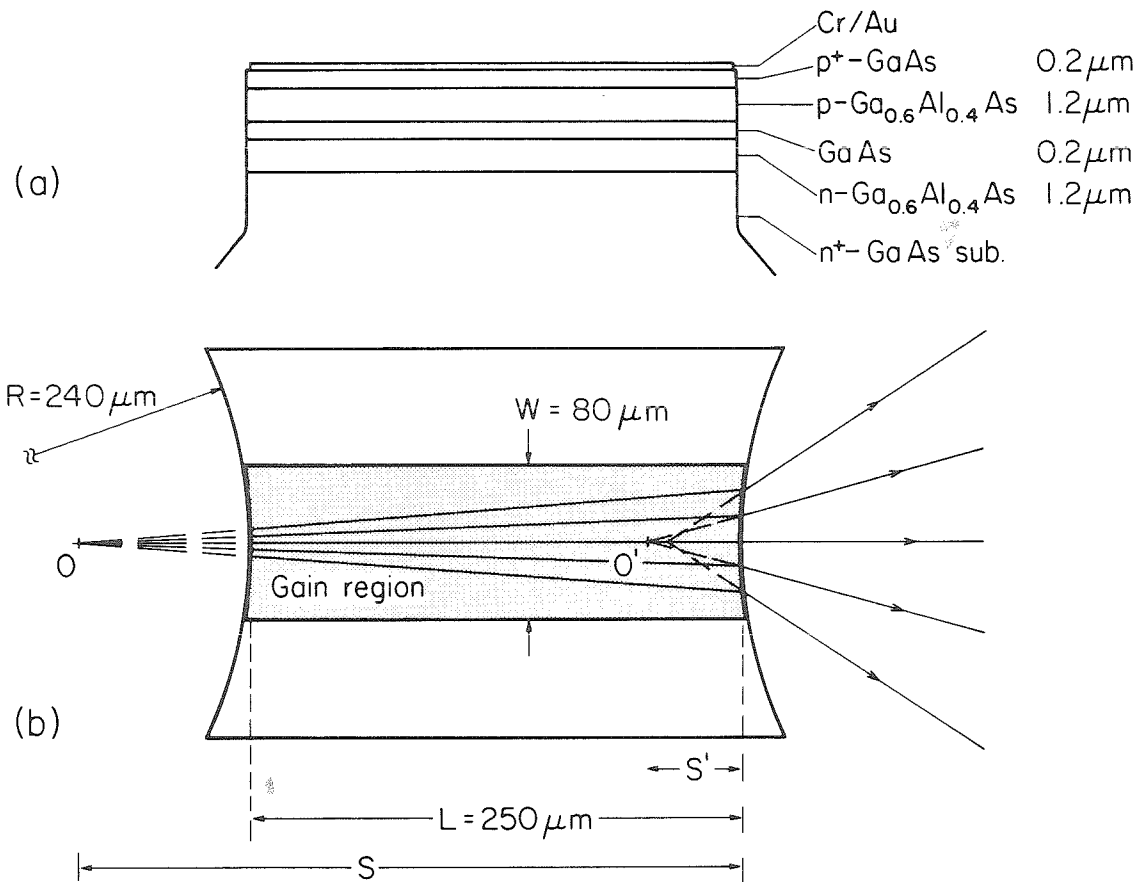
Figure 3.1 (a) Schematic of the layer structure. (b) Top view of the laser with geometrical ray description of the unstable-resonator semiconductor laser. Radiation emanating from a virtual source at point O is refracted through the output mirror, resulting in a virtual source of the output beam at point O'. Shown also is the spherical aberration at O'.

cleaved and the other mirror was convex, have been reported [3, 4, 5]. The operation of GaAs/GaAlAs lasers with two convex-mirror surfaces with no planar feedback in any part of the cavity was demonstrated [6]. Measurements of the near-field distribution of these lasers verified that the unstable resonator is indeed a means of overcoming the filamentation problems of conventional, double-heterostructure, broad-area lasers. Furthermore, high-output power (0.35 W) in a stable, highly coherent lateral mode and relatively high-external quantum efficiency ($\eta = 0.22$) were demonstrated in these devices [6].

3.2 Focusing Properties of Unstable-Resonator Semiconductor Lasers

The unstable-resonator lasers used for these measurements are presented (drawn to scale) in *Figure 3.1b*. The symmetric, unstable resonator is defined by etched facets with a radius of curvature $R = 240\mu m$ and a length of $L = 250\mu m$ on a double-heterostructure GaAs/GaAlAs wafer as shown in *Figure 3.1a*. The gain region is defined by a metal contact whose width is $W = 80\mu m$ [6]. This provides a structure without additional lateral guiding apart from the gain guiding and a single-path magnification of $M = 2.04$, leading to a round-trip magnification of $M_{roundtrip} = 4.17$ via the formula given in *Chapter 2*. An additional amount of gain, 28.6 $\frac{1}{cm}$, is required to compensate for the intentional spreading.

Since the output beam of the unstable-resonator laser is expected to be highly astigmatic, the minimum spatial extension of the beam in the principal planes is investigated. In the plane perpendicular to the p-n junction, the beam waist is at the facet, whereas in the plane of the junction, the light appears to originate at a virtual source located deep behind the laser facet. These observations imply that the wave-guiding effects determine the beam characteristics in the direction
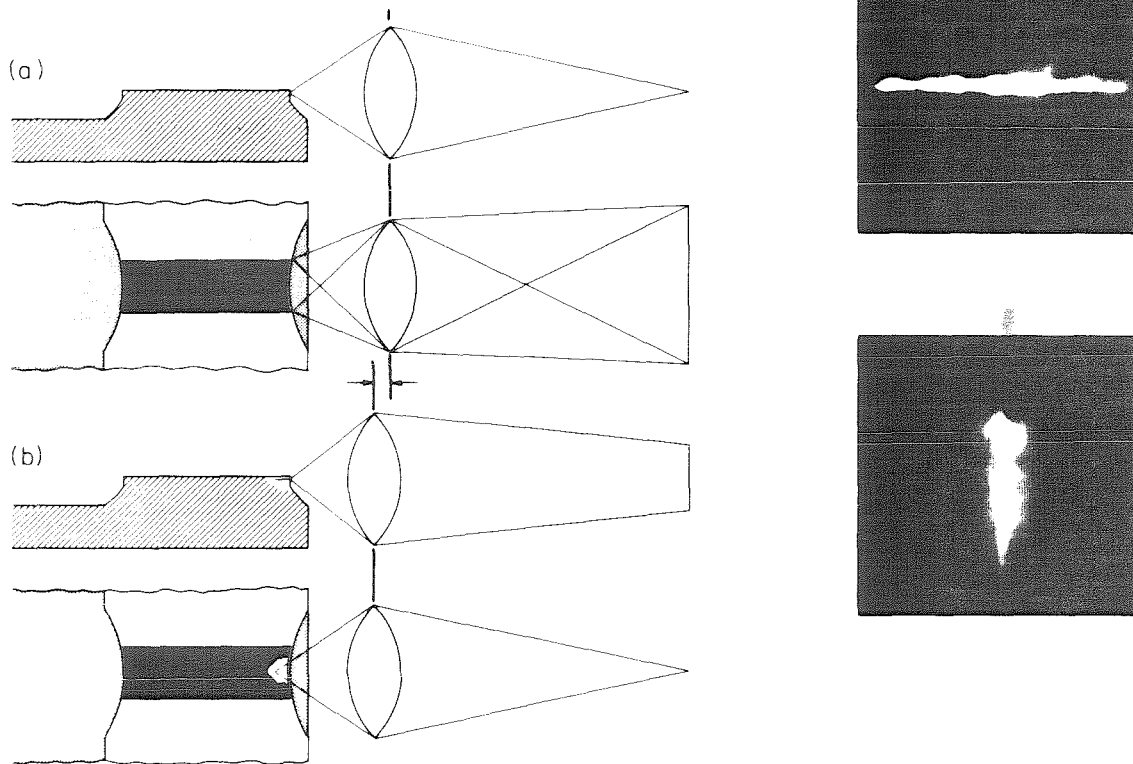
Figure 3.2 Schematic of near-field (a) and virtual-source point (b) measurement or an unstable-resonator semiconductor laser. Each of (a) and (b) shows the side view (transversal) cross section and below it the top view as well as the observed light-intensity distribution on the right-hand side. In (a) the horizontal extent is the image of the width of the wave-guide. In (b) the horizontal extent is the image of the width of the virtual-source point, while the vertical extent is the *out-of-focus* view of the confinement in the wave-guide.
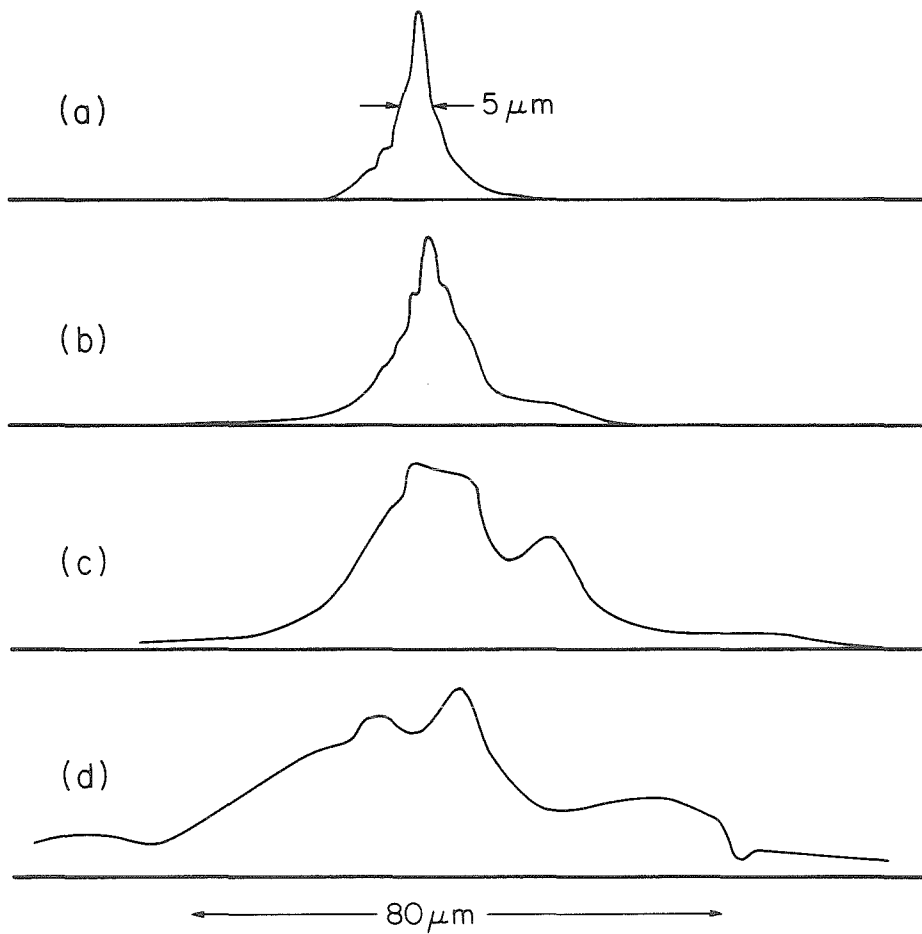
Figure 3.3 Normalized intensity profiles at the virtual-source plane as a function of injection current I, (a) $I = 3\ I_{th}$ (b) $I = 1.9\ I_{th}$ (c) $I = 1.4\ I_{th}$ (d) $I \simeq I_{th}$.

perpendicular to the p-n junction, while the cylindrical, unstable resonator governs the beam characteristics in the plane of the junction.

The depth of this virtual source (S' in *Figure 3.1b*) was measured with the aid of a microscope objective, and a value of $S' = 50\pm5\mu m$ was obtained. *Figure 3.2* shows the measurement technique used. The concept of being *out of focus* at least on one of the two principal planes becomes evident. The familiar condition of observing the beam waist in both principal planes simultaneously for an image of the magnified near-field pattern does not exist for an unstable-resonator semiconductor laser. The intensity distribution of this virtual source in the plane of the p-n junction was studied as a function of injection current, and a dramatic narrowing was observed when the injection current was increased from threshold (I_{th}) at $I \simeq 700mA$ to $3 \cdot I_{th}$. The measured full width of this virtual source (FWHM) at $3 \cdot I_{th}$, was $5\mu m$, with negligible intensity in the wings (*Figure 3.3*).

These results can be explained with the aid of the following simple model: The light inside the unstable resonator that propagates toward the output-coupling facet (*Figure 3.1b*) can be described in the geometrical optics approximation as a spherical wave originating at a point O, whose distance from the exit facet is given by [2]:

$$S = \sqrt{\frac{R \cdot L}{2} + \left(\frac{L}{2}\right)^2} + \frac{L}{2} = 339 \ \mu m \tag{3.1}$$

where R is the magnitude of the radius. After reflection at the cylindrical surface, the depth of the virtual-source point in the small-angle approximation [9] is obtained:

$$S' = \left(\frac{n-1}{R} + \frac{n}{S}\right)^{-1} = 48\mu m \tag{3.2}$$

where the index of refraction of the laser medium is $n = 3.5$. This result is in very good agreement with the measured value. The apparent sharpening of the
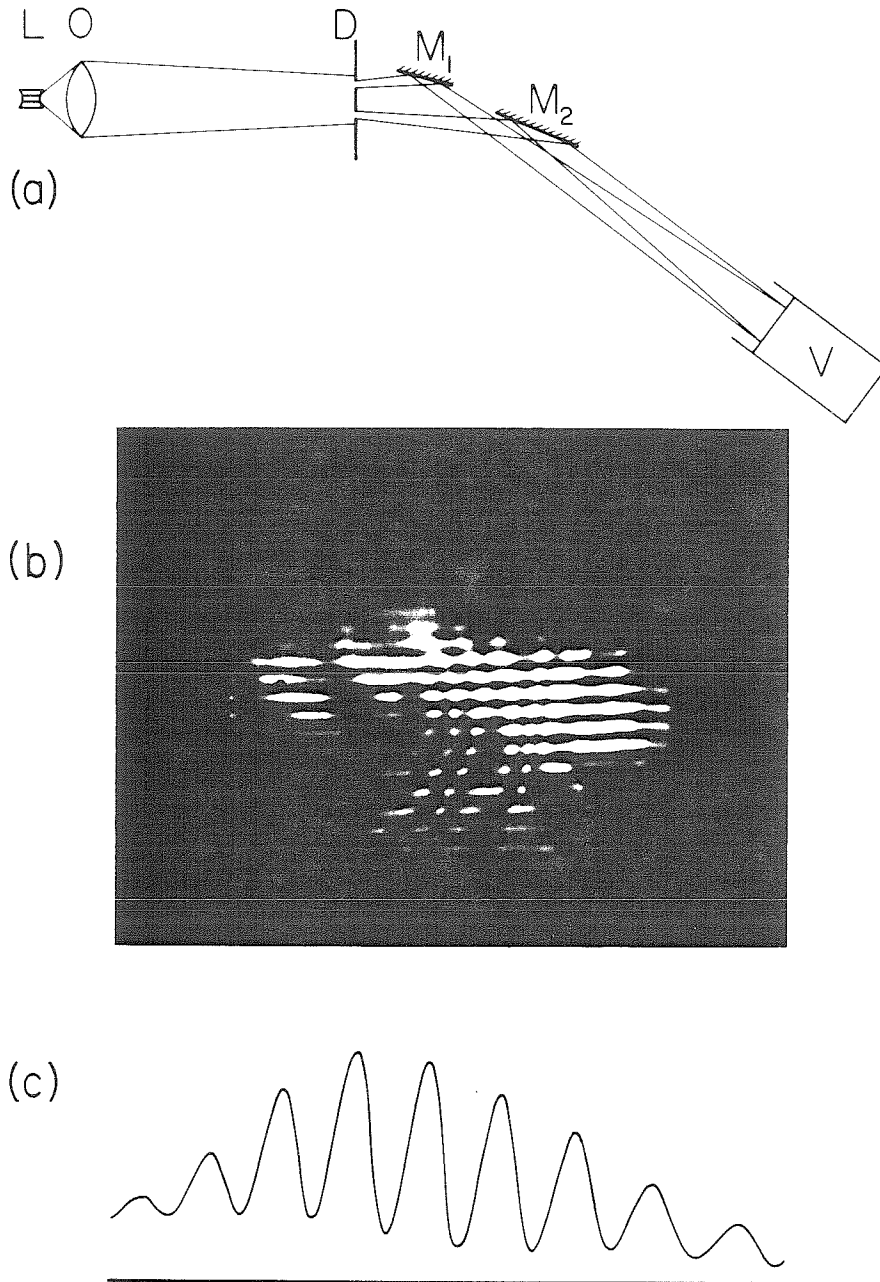
Figure 3.4 *Modified Young's double-slit experiment.* (a) Schematic of the optical layout of the interference experiment; L = unstable-resonator laser; O = microscope objective; D = double-slit in the image plane of the microscope objective with respect to the laser facet; M_1, M_2 = plane mirrors; V = vidicon camera in the far field of the slits. (b) Photograph of interference pattern. (c) Intensity trace of interference pattern.

intensity distribution with increasing injection current at the virtual-source plane is expected from the fact that below threshold, the light output is due mainly to spontaneous emission and amplified spontaneous emission, which are not governed by the resonator feedback. At higher currents the feedback effect dominates, and the laser output exhibits the mode properties of the unstable resonator. It should be noted that the FWHM of the virtual source in the lasers reported here is affected by a strong spherical aberration. A sharper image may be obtained from an aspherical output coupler.

3.3 Coherence Properties of Unstable-Resonator Semiconductor Lasers

The lateral mode characteristics of the unstable-resonator laser can be studied by measuring the spatial degree of coherence of the output beam as a function of the lateral position. In the multimode case, high spatial coherence is expected only between two points corresponding to comparable intensities of the same lateral mode, whereas two points whose intensities correspond to different modes will exhibit a low degree of spatial coherence. Spatial coherence between two points can be measured by observing the fringe visibility function (FVF) in an interference pattern produced by the radiation transmitted through two narrow slits placed at these points (*Young's double-slit experiment*). By scanning the slits across the near field of the laser, the coherence function between any two points on the laser output facet can be obtained.

In the experiment (*Figure 3.4a*), the laser near field was imaged and magnified to the plane D, which contained the double-slit screen. The slit separations and their positions relative to the imaged-laser near field could be varied. It should be noted that a magnified image of a near field is not a near-field amplitude distribu-

tion, because the magnification introduces phase-front curvature. As long as the two sources whose interference is to be measured are nearly diffraction-limited and the two corresponding beams are made to overlap, the phase-front curvature will cause only a shift in the position of the interference fringes (a property not considered in this measurement). The beams exiting from each slit were traced and found to be nearly diffraction-limited. Because of the angular separation between these two beams, additional mirrors were required in order to produce two overlapping (and interfering) beams as shown in *Figure 3.4a*. A high degree of spatial coherence was observed over the entire spatial extent of the laser output, independent of the lateral position. *Figures 3.4b* and *3.4c* are examples of the interference patterns recorded with a fringe visibility function of approximately 0.6. When the injection current was increased over $3 \cdot I_{th}$, the fringe visibility of the function decreased, presumably indicating the onset of higher-order modes. Similar measurements with broad-area lasers with cleaved facets (Fabry-Perot cavity), fabricated from the same wafer, showed substantially lower visibility of the interference pattern, and a spatial degree of coherence varying with position and injection current. These experimental findings provide ample evidence that the unstable-resonator structure supports operation dominantly in one lateral mode at moderate injection currents in spite of the very wide ($80\mu m$) width of the laser mode.

3.4 Conclusion

Some of the emission characteristics of unstable-resonator semiconductor lasers have been measured. The output beam is highly astigmatic, with a virtual source corresponding to that expected from the modal analysis of unstable resonators. Single-mode operation was demonstrated by measuring the spatial degree of coherence of the laser output. If the highly astigmatic beam is corrected for by ap-

propriate external optics, the focusing capability of these lasers may lead to power densities in a single mode higher than that emitted by any other semiconductor source reported until now.

3.5 References

[1]. Boyd G.D., and H. Kogelnik: *"Generalized confocal resonator theory."* Bell System Tech. J., 41:1347-1369 (1962).

[2]. Siegman A.E.: *"Unstable optical resonators for laser applications."* Proc. IEEE. 53:277-287 (1965).

[3]. Bogatov A.P., P.G. Eliseev, M.A. Man'ko, G.T. Mikaelyan, and Yu.N. Popov: *"Injection laser with an unstable resonator."* Sov. J. Quantum Electron. 10:620 (1980).

[4]. Craig R.R., L.W. Casperson, G.A. Evans, and J.T.J. Yang: *"High loss resonators for semiconductor diode lasers."* Presented at the Conference on Lasers and Electro-optics, Anaheim, CA, USA, 18th-24th June 1984.

[5]. Craig R.R., L.W. Casperson, O.M. Stafsudd, J.T.J. Yang, G.A. Evans, and R.A. Davidheiser: *"Etched mirror, unstable-resonator, semiconductor lasers."* Electron Lett. 21:62-63 (1985).

[6]. Salzman J., T. Venkatesan, R.J. Lang, M. Mittelstein, and A. Yariv: *"Unstable resonator cavity, semiconductor lasers."* Appl. Phys. Lett. 46:218-220 (1985).

[7]. Salzman J., R.J. Lang, T. Venkatesan, M. Mittelstein and A. Yariv: *"Model properties of unstable-resonator, semiconductor lasers with lateral wave-guide."* Appl. Phys. Lett. 47:445-447 (1985).

[8]. Salzman J., R.J. Lang, R. Larsson, and A.Yariv: *"Confocal unstable-resonator, semiconductor laser."* Opt. Lett. 11:507-509 (1986).

[9]. Born M., and E. Wolf: *Principles of Optics.* Pergamon: London (1965) Chapt. 4.4, pp.157-160.

Chapter Four

4: Experiments with Broad-Area, Single-Quantum-Well Lasers

Abstract

Lasing characteristics of broad-area stripe contact lasers fabricated from single-quantum-well, graded-index wave-guide, separate confinement heterostructures are measured. External absolute quantum efficiencies of 0.79, distributed losses below $2 \frac{1}{cm}$, and output powers exceeding 5 W were found for 100 μm-wide devices. These lasers exhibited beam divergence below two times the diffraction limit in single-lobed, far-field patterns. Spectrally resolved near-field, high-resolution far-field, and coherence measurements showed lateral modes with nearly planar phase fronts across most of the widths of the device.

4.1 Introduction

During the last ten years, a great effort in the field of semiconductor laser research has been devoted to the development of high-power semiconductor lasers that emit into a stable and narrow, single-lobed, lateral, far-field pattern in the plane of the junction. In order to overcome the filamentation problems in conventional, double-heterostructure, broad-area lasers, different approaches such as array lasers [1], unstable-resonator lasers (see *Chapters 2* and *3*) and gain-tailored lasers [2, 3, 4] have been used. The objective is to achieve a large area beam at the output facet and to avoid oscillation in several lateral modes simultaneously as well as to overcome the filamentation problems.

$1.5\,\mu$m p – $Ga_{0.5}Al_{0.5}As$

$\begin{cases}0.2\,\mu$m graded p – \\ $Ga_{0.8}\,Al_{0.2}\,As \rightarrow Ga_{0.5}\,Al_{0.5}\,As\end{cases}$

$100\,\overset{\circ}{A}$ Ga As

$\begin{cases}0.2\,\mu$m graded n – \\ $Ga_{0.5}\,Al_{0.5}\,As \rightarrow Ga_{0.8}\,Al_{0.2}\,As\end{cases}$

$1.5\,\mu$m n – $Ga_{0.5}\,Al_{0.5}\,As$

$\begin{cases}0.1\,\mu$m n$^+$– \\ $5\times(Ga\,As/Ga_{0.5}\,Al_{0.5}\,As)$ \\ Superlattice\end{cases}$

$\begin{cases}0.5\,\mu$m n$^+$–Ga As \\ Buffer\end{cases}$

n$^+$–Ga As Substrate

0.0   0.5   Al content in $Ga_{1-x}Al_xAs$

3.6   3.3   Index of Refraction at 850 nm
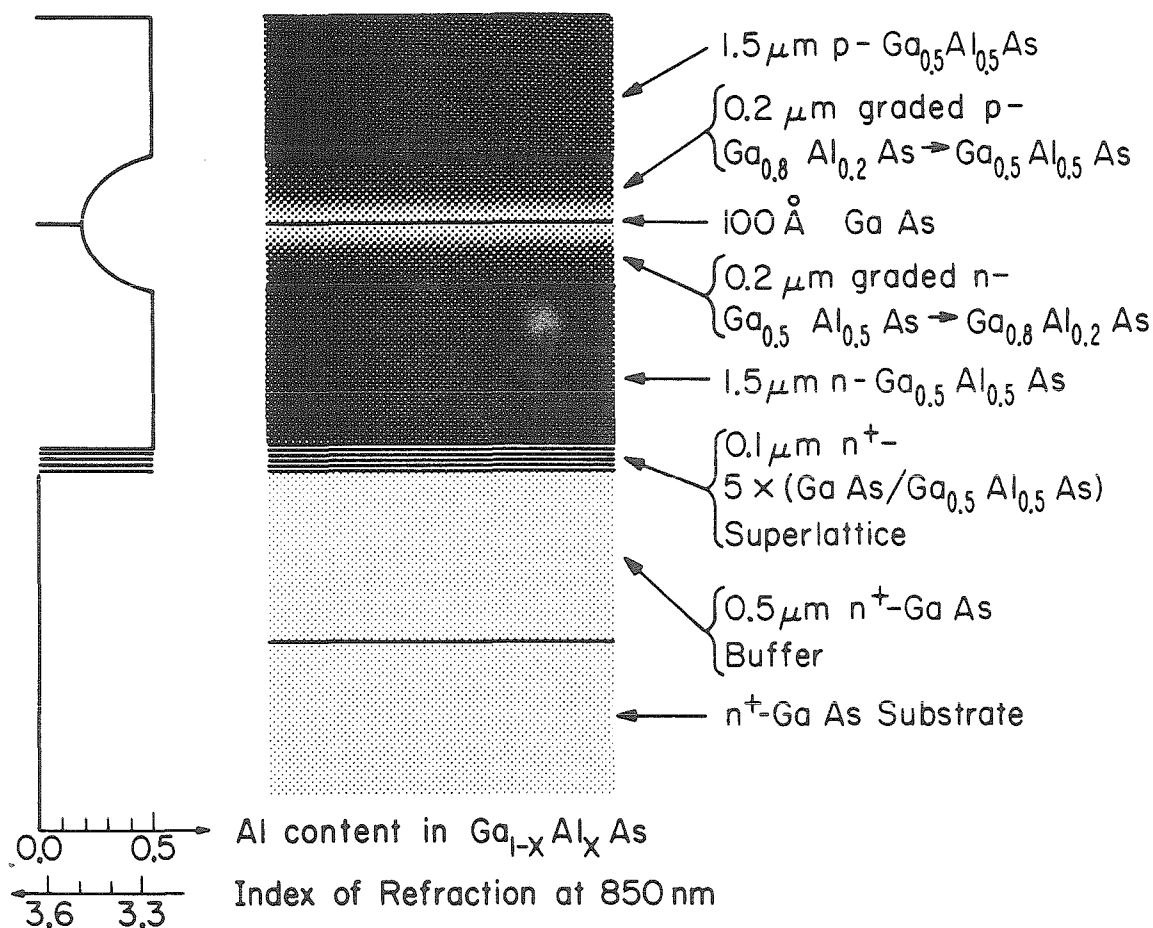
Figure 4.1 Single-quantum-well, graded-index wave-guide, separate-confinement heterostructure (SQW-GRINSCH) as used in these experiments. The transverse profile of the aluminum concentration of the GaAlAs/GaAs structure is shown together with its index of refraction in the vicinity of the lasing wavelength. In the center the shading gives the Al content. On the right, the thickness of the layers and their doping are given.

All of the above-named approaches involve increased processing complexity and suffer from a variety of specific problems. Consequently, the taming of the simple broad-area laser remains a worthwhile goal. Initial progress in this direction was indicated by Tsang [5], who demonstrated high-lasing uniformity and a stable single-lobed, far-field pattern with devices prepared by molecular beam epitaxy (MBE). In this chapter, the design and performance characteristics of broad-area, single-quantum-well, graded-index wave-guide, separate-confinement heterostructure lasers (SQW-GRIN SCH) are presented.

4.2 Design and Basic Performance

The broad-area lasers used in the experiments described here had 100 μm wide stripe contacts with gold metallization over a shallow Zn diffusion. No additional means of lateral guiding is employed. The MBE-grown layer structure of the laser was based on a superlattice buffer and was composed of a parabolic, graded, optical wave-guide of a total width of 4000 $\mathring{A}$ and a central, single-quantum-well of 100 $\mathring{A}$ width confining the carriers. *Figure 4.1* shows the transverse structure. The fabrication of different laser lengths was facilitated by orientating the crystal with its cleaving plane perpendicular to the stripe contacts.

The length of the Fabry-Perot resonator for optimum performance was about 480 μm, resulting in pulsed threshold currents of 110 mA equivalent to 230 $\frac{A}{cm^2}$ threshold current density (for more experimental results, see *Chapter 5*). All the following measured quantities were taken under pulsed excitation of 100 to 400 ns and individual pulse to 5 kHz repetition rate on unmounted lasers at room temperature. The maximum, single-sided output power for 2.4 A driving current of these symmetric devices was 1.35 W. Driving with substantially larger currents
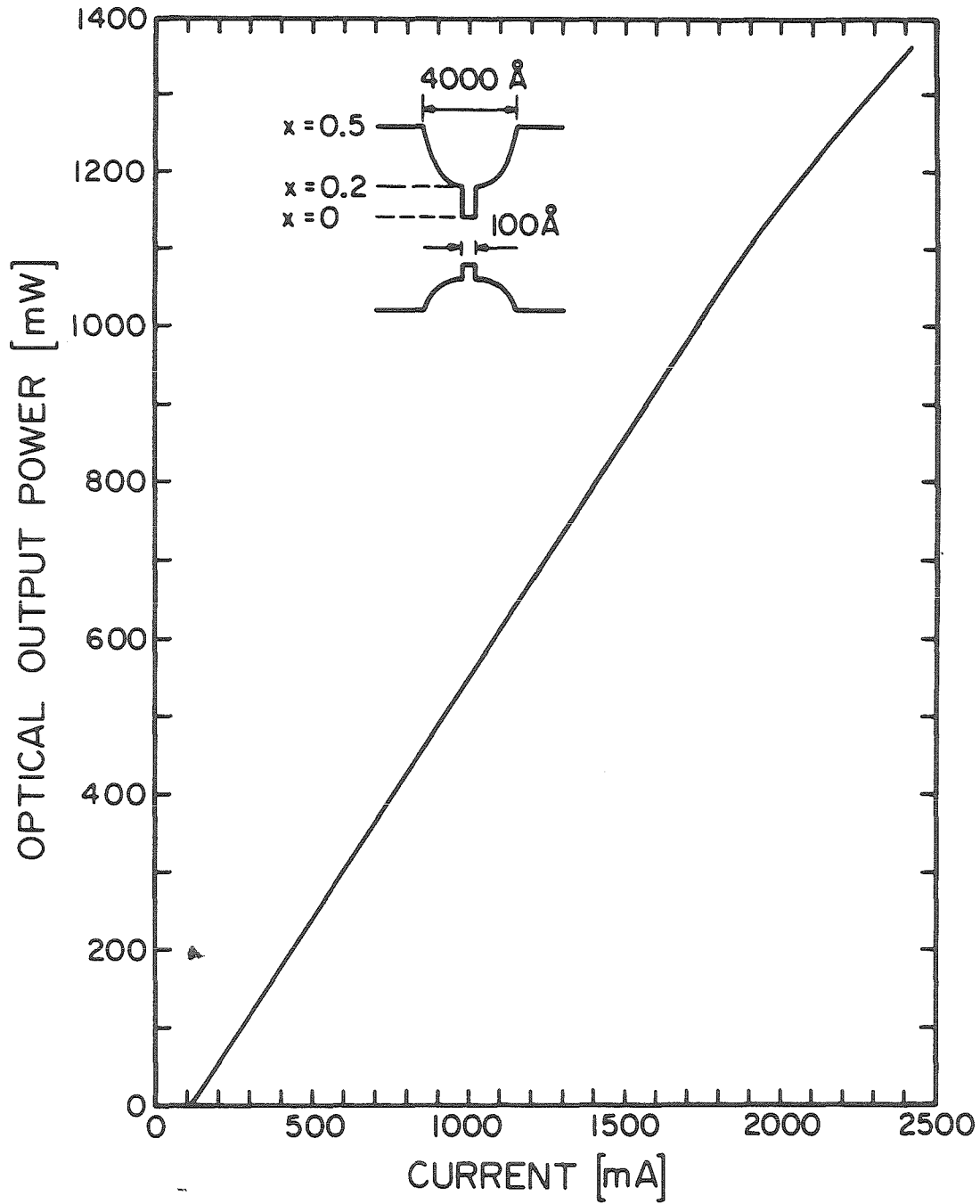
Figure 4.2 Optical output power against current under pulsed conditions (400 ns, 25 Hz) for a broad-area laser with a stripe width of 100 μm and a cavity length of 480 μm.

nearly doubled the output power; similar devices with slightly higher threshold currents exhibited a single-sided output power well in excess of 5 W [6].

In *Figure 4.2*, the pulsed, single-sided output power versus driving current of the broad-area, single-quantum-well laser is shown. For currents starting at threshold and up to 15 times threshold, a differential quantum efficiency of 0.84 is derived under the consideration of the symmetrical resonator, resulting in a maximum, absolute quantum efficiency of 0.79. This high-external quantum efficiency is a combined result of the low threshold current density and the very high-differential quantum efficiency. The distributed internal losses were found to be as low as 1.8 $\frac{1}{cm}$ according to the data of differential quantum efficiency measurements for cavity length ranging from 480 to 1540 μm, assuming a linear behavior over that range. In the meantime, several other groups have reported equally high quantum efficiencies, for example, [7]. The overall efficiency is the highest of any reported lasers.

4.3 Near- and Far-Field Pattern and Coherence

In agreement with Tsang's observations [5], a high uniformity in the near-field distribution with intensity profiles preserved up to very high injection levels ($10 \cdot I_{th}$) was observed. While his reported result was a stable, far-field pattern with a single central lobe of constant width some 18 times diffraction-limited, very narrow, single central lobe far-field patterns were observed at least near threshold. Actually, at $1.2 \cdot I_{th}$ the 100 μm wide lasers emitted a beam whose full width at half maximum was measured to be as low as 0.8 degrees. This value compares to the lower limit of a beam from an aperture (box-type intensity without phase front curvature) of 0.43 degrees, thus corresponding to 1.9 times diffraction-limited. In the measurements
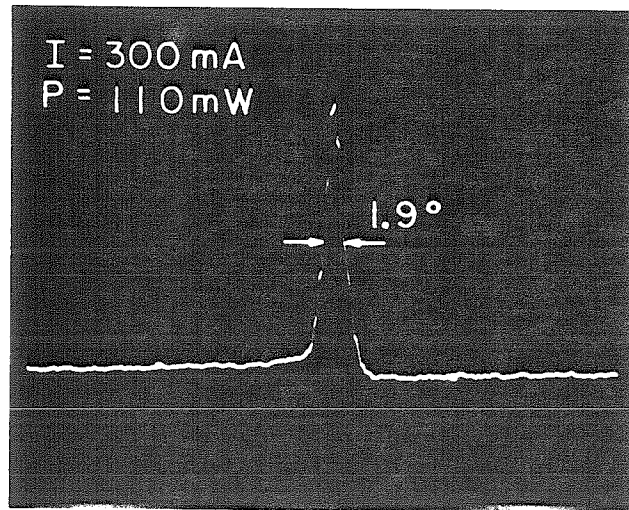
(a)
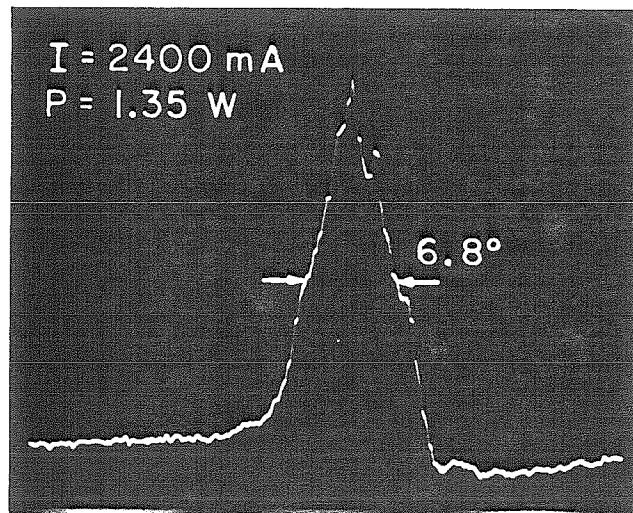
(b)

Figure 4.3 Far-field pattern parallel to the junction plane for a 100 μm-wide, broad-area laser at two different pump currents as indicated. Note the increase in width without an introduction of any pronounced structure.
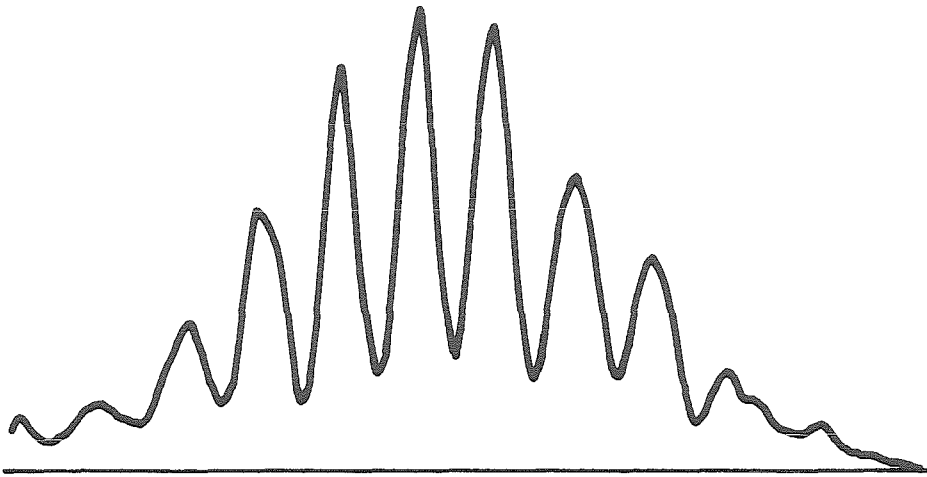
Figure 4.4 Interference pattern between two points at the laser facet, 50 μm apart.

reported here, the far-field pattern remains a symmetric, single central lobe, but it broadens continuously with increasing power, reaching a width similar to Tsang finding near an output power of 1 W. Two far-field patterns at different pump currents are shown in *Figure 4.3*. The distributions shown, which are typical, are free from any significant structure but are of several times diffraction-limited widths. The extremely narrow far field was observed in a minority of the lasers, but many lasers showed a value of the beam divergence of 2 degrees up to 100 mW as in *Figure 4.3*.

The lateral coherence of these broad-area lasers was investigated by means of the modified version of Young's double-slit experiment as introduced in *Chapter 3*. A typical interference pattern from two source points of the near field some 50 μm apart is shown in *Figure 4.4*. The observed fringe visibility function is two-thirds, indicating good coherence. A high degree of spatial coherence was measured up to lateral separations of 80 μm, but some regions of the laser near field exhibited lower coherence even at a small separation of the source regions used for interference. In many lasers, the measured lateral coherence was increasing with increasing injection current up to 3 times the threshold value. At 8 times the threshold value, the fringe visibility function degraded considerably.

4.4 Spectrally Resolved Near-Field Pattern

To gain further insight into the operational conditions of the broad-area, single-quantum-well laser, the spectrally resolved near-field images at different pumping levels were observed. These devices operate in multiple longitudinal modes in basically all cases. At high power, the spectrum of a contributing mode tends to be wider. One feature emerges from looking at many spectrally resolved near-field
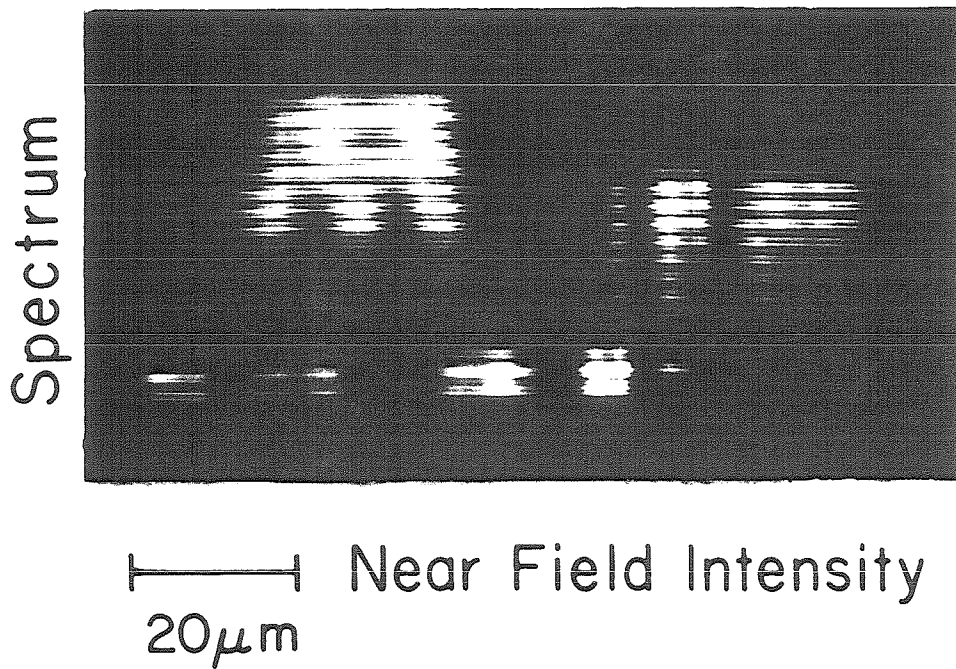
Figure 4.5 Spectrally resolved near-field intensity distribution for $I = 1.6 \cdot Ith$. The vertical axis corresponds to wavelength, and the horizontal axis is the lateral dimension. The longitudinal mode is $\Delta\lambda = 2.2$ $\overset{\circ}{A}$. The patterns are discussed in the text.
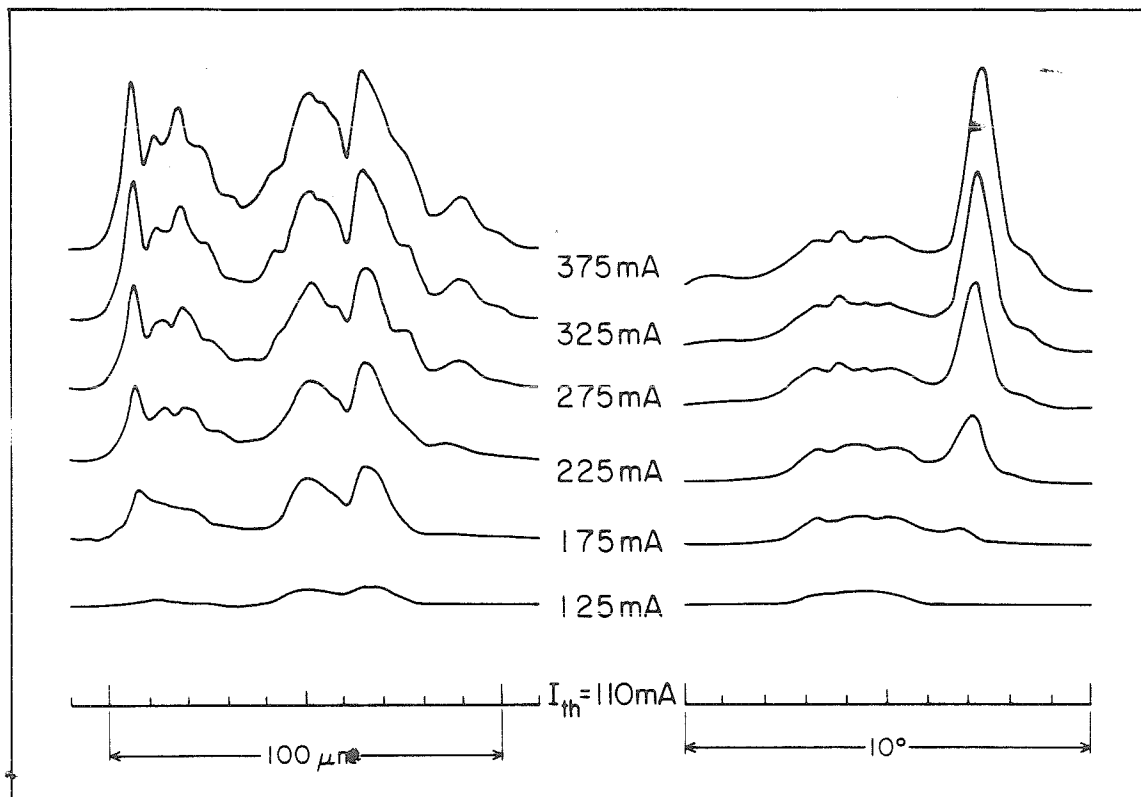
Figure 4.6 Near-field and corresponding high-resolution far-field patterns of a 100 μm wide broad-area laser at several pump currents up to $3.4 \cdot I_{th}$. See text for interpretation.

images: there are groups of mostly adjacent longitudinal modes of similar lateral pattern. More precisely, the lateral modes within a group show trends. The dissimilarities increase with spectral distance. Several of these lateral modes do not show high intensity over more than a fraction of the width of the active region. As an example, the spectrally resolved, near-field intensity distribution of a device emitting into a fairly narrow, far-field pattern is shown in *Figure 4.5*. The group of lateral modes showing high intensity in the upper left-hand quadrant show the mentioned trend; three lobes in the lower end go over into a more uniform intensity distribution with probably two intensity maxima in the upper end. Also, the lower half of the picture shows a mode whose lateral width makes it a candidate for a very narrow, far-field distribution, if its phase is nearly flat and the other modes do not make its contribution subdominant.

One of several particular lasers is chosen and examined, to emphasize the importance of individual longitudinal modes, or a group of them, causing a very narrow contribution to the far-field pattern. In *Figure 4.6*, many lateral, near-field intensity profiles and corresponding far-field patterns are shown to illustrate a case where the additional pumping was dominantly channeled into lateral modes that had a very narrow, far-field pattern. In this case, the narrow, far-field contribution may be off center, indicating a slant in the nearly flat phase front of the contributing lateral modes. As can be seen from the near fields, the mode is not specially located at a small portion of the width of the device but rather spans the whole width, which is a prerequisite for a far-field contribution that narrow.

4.5 Conclusions

The experimental findings present evidence that a close-to-ideal, broad-area

laser can be fabricated. The measured overall efficiency of this type of laser is the highest of any reported lasers. The high-power behavior shown in the experimental findings exhibits a gradual width increase of far-field patterns. This gradual change and in particular the nearly structureless, single-lobed symmetrical shape is yet unexplained. The multiple, longitudinal-mode operation may be of fundamental importance. The most significant conclusion from the experimental findings is that more than half of the width of the broad-area lasers described is coherent and in phase and that filamentation in its destructive sense does not exist in these high-quality, single-quantum well lasers.

4.6 References

[1]. Scifres D.R., C. Lindström, R.D. Burnham, W. Streifer, and T.L. Paoli: *"Phased-locked (GaAl)As laser diode emitting 2.6 W CW from a single mirror."* Electron. Lett., 19:169-171 (1983).

[2]. Lindsey C.P., P. Derry, S. Margalit, and A. Yariv: *"Tailored-gain-phased array of semiconductor lasers with single-lobed far field."* Paper TU-F1 presented at Conference on Lasers and Electro-Optics, Baltimore, Maryland, USA. 21st-24th May (1985).

[3]. Lindsey C.P., P. Derry, and A. Yariv: *"Fundamental lateral-mode oscillation via gain tailoring in broad area semiconductor lasers."* Appl. Phys. Lett., 47(6):560-562 (1985).

[4]. Lindsey C.P., P. Derry, and A. Yariv: *"Tailored-gain broad-area semiconductor laser with single-lobed, diffraction-limited, far-field pattern."* Electron. Lett., 21(16):671-673 (1985).

[5]. Tsang W.T.: *"Symmetric separate-confinement (SCH) (AlGa)As lasers with low threshold and narrow beam divergence grown by molecular beam epitaxy."* Electron. Lett., 16:939-941 (1980).

[6]. Chen H., and M. Mittelstein; unpublished.

[7]. Harder C., P. Buchmann, and H. Meier: *"High-power ridge-wave-guide AlGaAs GRIN-SCH laser diode."* Electron. Lett., 22:1081-1082 (1986).

5: Second Quantized State Lasing of Single-Quantum-Well Lasers

Abstract

Newly observed features of quantum-well lasers are presented and explained with the aid of a simple model. These involve lasing with gain contributions not only from the fundamental ($n = 1$) state, but simultaneously from the second quantized ($n = 2$) state as well. Experimental data for current-pumped GaAs/GaAlAs single-quantum-well lasers are presented. Very high resonator losses (≥ 100 cm^{-1}) force the lasers to augment their gain with major contributions from the second quantized state. The main signature of $n = 2$ lasing, a sudden and large increase in the lasing photon energy, is observed and explained by the theory.

5.1 Introduction

In this chapter, an experimental and theoretical investigation of the gain of quantum-well lasers is presented, and experimental evidence of lasing involving the second quantized ($n = 2$) state is introduced [1]. Lasing at a higher energy is induced by intentionally increasing the losses in a single-quantum-well laser, which is attained by decreasing the cavity length of Fabry-Perot lasers. This causes a disproportionate increase in the threshold current. This feature was predicted by Arakawa and Yariv [2] and by McIlroy et al. [3] and was also observed by P.S. Zory et al. [4] but was not specifically related, previously, to the second quantized-state lasing. Additional experimental results and a theoretical explanation, [5-11], have been published since this research was performed.

50
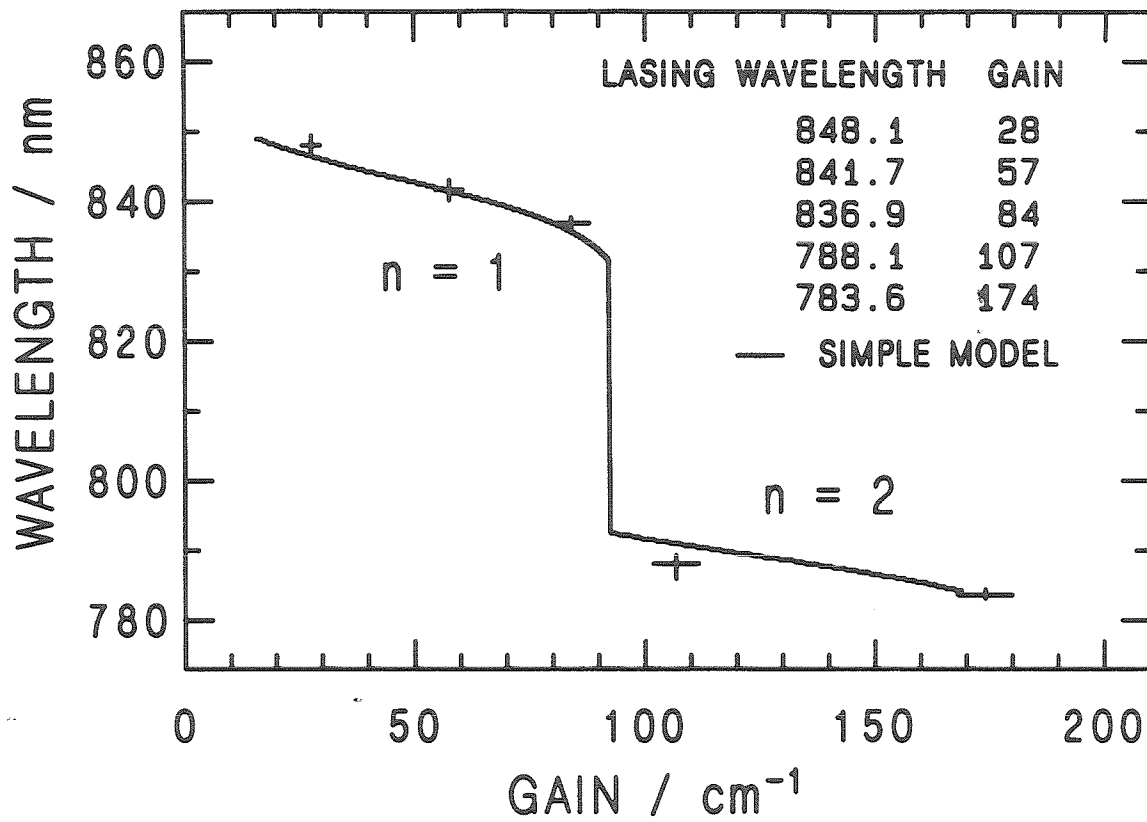
Figure 5.1 Measured lasing wavelength versus modal gain (derived from measured length via in Equation 5.1) shown in comparison to predictions of the simple model.

5.2 Experimental Approach

The experimental approach utilizes the fact that at lasing the modal gain constant g is equal to the modal losses; that is, in the Fabry-Perot resonator,

$$g_{mode} = a_i + \frac{1}{2 \cdot L} \cdot ln(\frac{1}{R \cdot R}) \tag{5.1}$$

Cleaved, uncoated, broad-area, gain-guided lasers are used (refer to *Chapter 4* for details of the structure), and a power reflectivity of $R = 0.3$ is assumed. The single-quantum-well devices were grown by molecular-beam epitaxy [12]; they show very low internal losses measured to be $a_i \leq 2$ cm^{-1} (refer to *Chapter 4*). Therefore, the modal gain at lasing can be selected by simply cleaving devices to the appropriate length L [1].

A set of lasers was characterized and then cleaved to progressively shorter lengths for further characterization, resulting in lasers with lengths spanning 70 to 470 μm. This method eliminates the possibility that variations in separate devices affected the interpretation of the measurements, leaving only the quality of the cleave and nonuniformity along the original devices as potential problems. In *Figure 5.1* the measured wavelength of the first mode to lase (at threshold) is shown as a function of the modal gain constant. The vertical bar indicates the *spread* of the data, while the horizontal bar gives the average value. The curve shows the results of a theoretical model, which is discussed in the following section. The most striking feature of the data is the very abrupt change of lasing wavelength in the vicinity of 100 cm^{-1}, which is identified with the onset of *second quantized-state lasing* $(n = 2)$.

n=2

n=1

D(E)

E

n=1 ELECTRON to n=1 HOLE TRANSITION

n=2 ELECTRON to n=2 HOLE TRANSITION

FOR MINIMUM ENERGIES SHOWN ON LEFT SIDE
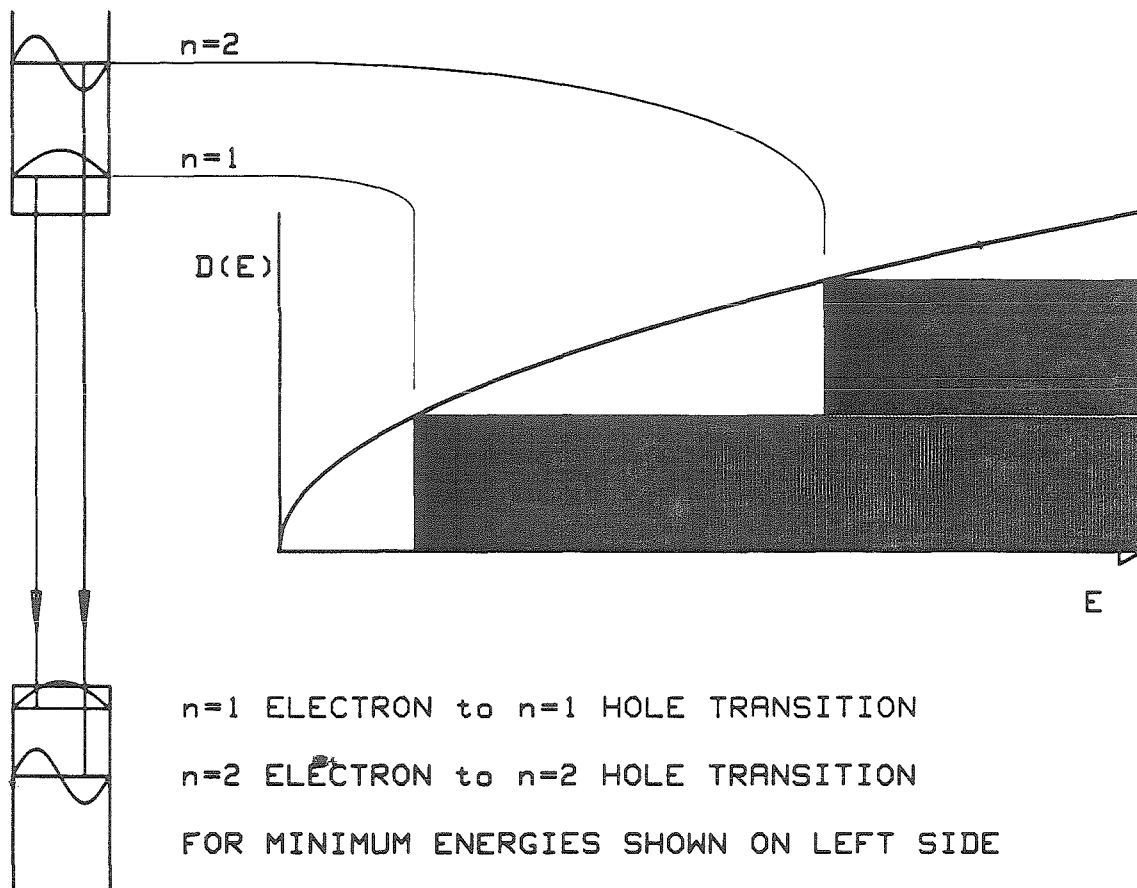
Figure 5.2 Schematic of a quantum well and its confined states causing a staircase density-of-states function.

5.3 Basic Theoretical Approach

A simple model is employed to describe the essential characteristics of a quantum-well laser and their implications with respect to our measurements. The one-dimensional carrier confinement in a quantum well leads to a staircase like density-of-states function. Considering the $n = 1$ and $n = 2$ states only, the modal gain at photon energy E is calculated from

$$g_{mode}(E) = C \cdot \sum_{n=1}^{2} H\left[(E - E_g) \cdot S - E_n\right] \cdot \left[2 \cdot f_c(E) - 1\right] \qquad (5.2)$$

The constant C, the maximum available modal gain per quantized state, is estimated from the data to be 100 $\frac{1}{cm}$. The conduction band offset as a fraction of the total bandgap offset, S, is taken to be 0.85 [13]. The staircase nature of the density-of-states function is represented by the Heaviside function H. For E_g, the bandgap energy of bulk GaAs 1.42 eV was used. The Fermi function for the electrons with the quasi-Fermi energy E_{fc} is

$$f_c(E) = \frac{1}{1 + e^{\frac{(E - E_g) \cdot S - E_{fc}}{K \cdot T}}} \qquad (5.3)$$

Figure 5.2 shows a schematic of how the confined states give rise to the steplike density-of-states function. With $m_c^* = 0.067 \, m_e$, where m_e is the electron mass, a 100 $\overset{\circ}{A}$ infinite wall well implies that the first quantized energy is $E_1 = 0.056 \, eV$ and that E_2 is four times as large. In the particular structure used in our experiments (as described in *Chapter 4*), the actual values are computed by numerical solution of the Schrödinger equation to be $E_1 = 0.0314 \, eV$ and $E_2 = 0.1196 \, eV$ (refer to *Chapter 6*). In this calculation, $E_g(X) = (1.42 + 1.247 \cdot X) \, eV$, where X is the Al mole fraction. The *Equation (5.2)* is a simplification that ignores specific features concerning the holes and does not include collision-broadening. It is a simple model,
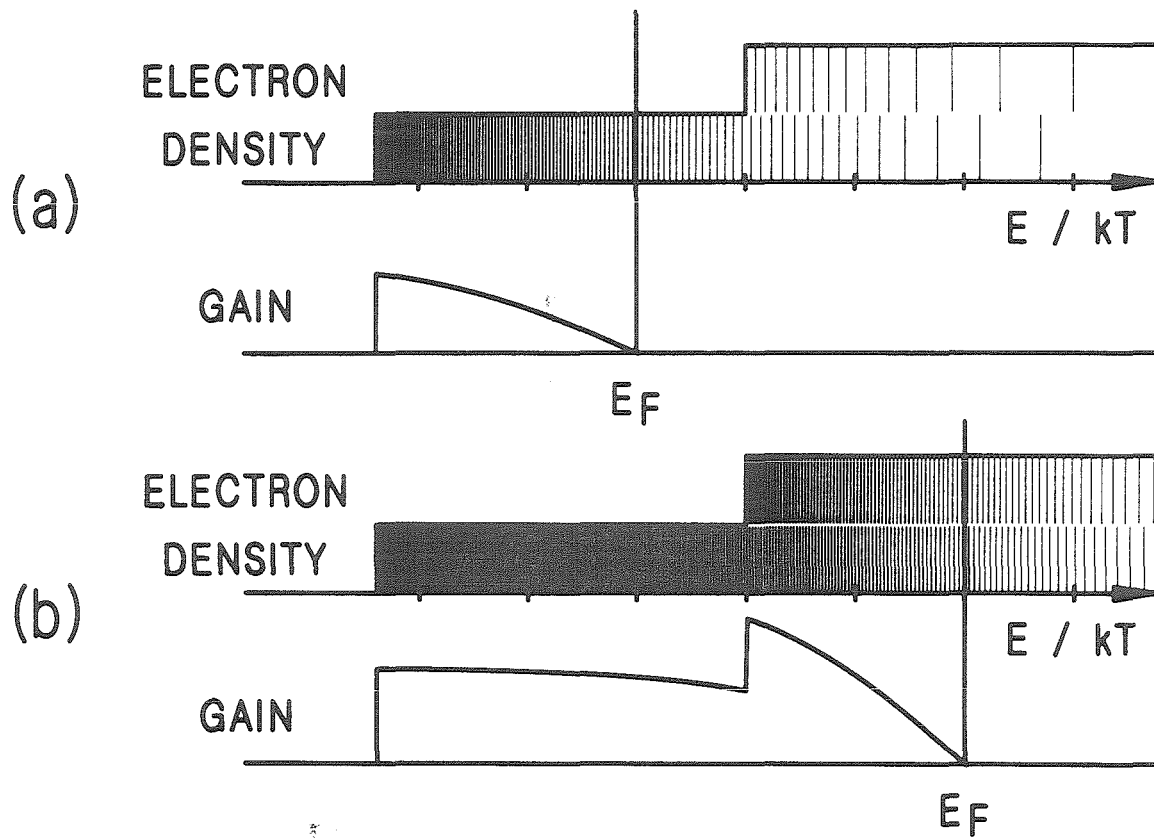
Figure 5.3 Gain spectra as computed using *Equation (5.2)* from the shown electron density. The occupation of the staircase density-of-states function is indicated by shading. The vertical bar indicates the quasi-Fermi energy. The energy is drawn to scale for room temperature. Part (a) shows conditions of high pump density, part (b) of very high pump density, resulting in the gain maximum at the onset energy of the second quantized state.
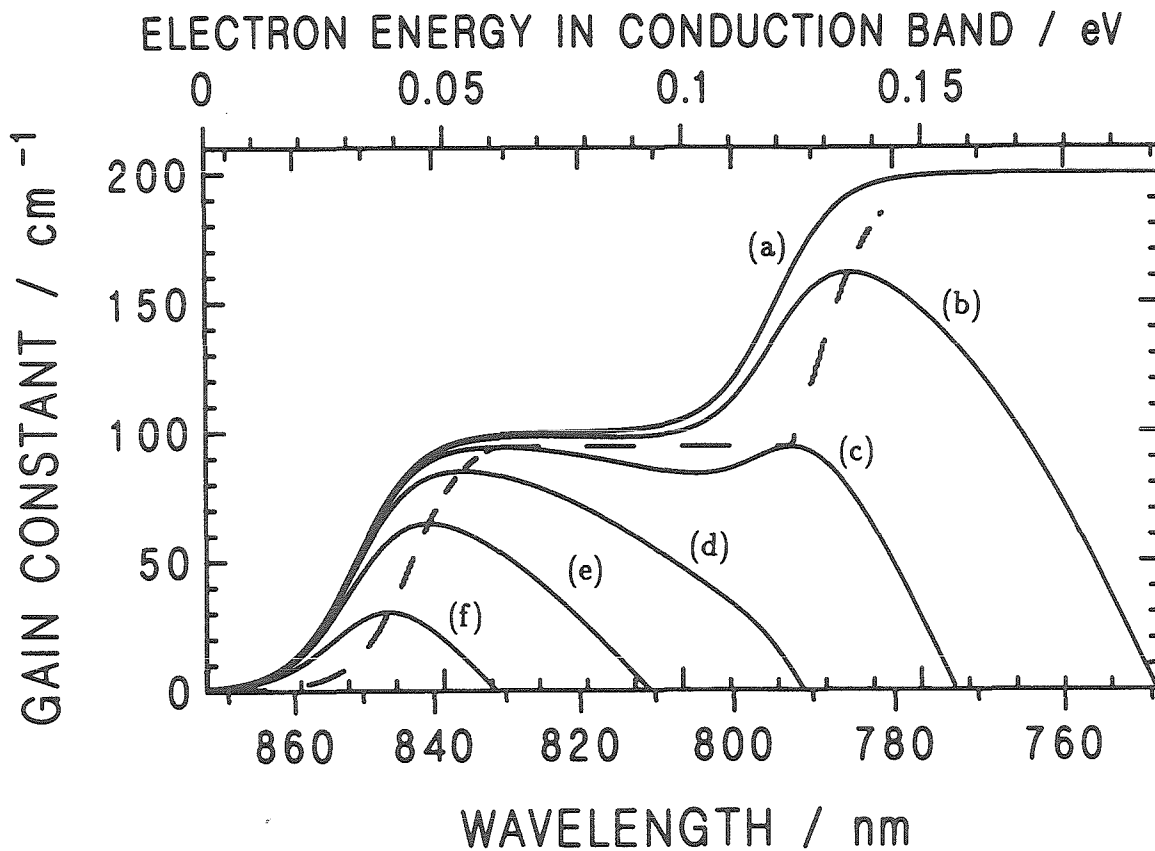
Figure 5.4 Gain spectra as computed using *Equation (5.4)* for various quasi-Fermi energies are shown as solid lines. The curve (a) gives the maximum available gain, which is limited by the density-of-states function. The curves (b) to (f) give gain spectra for deceasing pumping strengths coresponding to deceasing quasi-Fermi energy. The broken curve traces the maximum gain of the spectra with varying quasi-Fermi energy.

but amply sufficient to explain quantitatively the basic effects under investigation in this chapter.

Figure 5.3 shows the electron-density distribution and gain spectrum of the basic model for two conditions: *Figure 5.3a* is for the case of high threshold current density; *Figure 5.3b* is for the case of a very high-pump current density. The gain spectrum at the higher pumping levels is very wide, and the one of highest current density shows a new peak at the onset energy of the second quantized state. Especially notable is the doubling of the gain at the onset energy of the second quantized state, where its gain adds to that of the first one. Furthermore, in this model, considerably higher quasi-Fermi energies (as obtained in very short lasers) lead to nearly double the gain in the high-energy region with respect to the maximum value obtainable from the $n = 1$ state alone.

5.4 Refined Theoretical Approach

For more realistic quantitative results, broadening is incorporated via an effective smearing of the steps in the density-of-states function in the basic model by an amount $\Delta E = \hbar/\tau$, where $\hbar$ is Planck's constant divided by 2π, and τ is the intraband scattering time of the electrons. A value of $\Delta E = 6.6 \; meV$ corresponding to $\tau = 0.1 \; ps$ is used. The broadening is altered to have exponential tails rather than a Lorentzian shape (for further elaboration refer to *Chapter 6*). Including broadening, the modal gain expression becomes

$$g_{mode} = C \sum_{n=1}^{2} \frac{2f_c(E) - 1}{1 + e^{\frac{E_n - (E - E_0) \cdot S}{\Delta E}}} \tag{5.4}$$

This equation gives gain spectra as shown in *Figure 5.4* for different quasi-Fermi energies. In this model, the gain curve crosses zero at the quasi-Fermi energy of

the conduction electrons. The higher quasi-Fermi energies (corresponding to larger pumping densities) are associated with the short-cavity lasers. The calculations show a wide gain spectrum, which leads to a high level of recombination radiation even before threshold is reached. We verified this conclusion by measuring gain spectra of short lasers below threshold. The lasers showed fairly flat gain over a region extending over more than 50 nm.

The uppermost curve in *Figure 5.4* shows the upper limit of available gain as a function of photon energy, that is, the value that would result from an infinite pumping current in this model. Therefore, the gain needed to overcome very high losses (≥ 100 cm^{-1} in this case) can be obtained from a single-quantum-well laser only by enlisting the added contribution of the second ($n = 2$) quantized state, which is available at higher photon energies and at higher pumping currents (refer to *Figure 5.4* curve (b)). Consequently, the lasing wavelength must shift to shorter wavelengths as the required gain (i.e., the loss of the cavity) is increased. By tracing the peak of the gain spectrum (*5.4*) for varying quasi-Fermi energies as indicated in *Figure 5.4*, the lasing wavelength as a function of modal gain is obtained in this model. This result is the curve shown together with the experimental data in *Figure 5.1*.

5.5 Threshold Current Density as a Function of Required Gain

The lasing-wavelength characteristics explained above are accompanied by an extraordinary increase in threshold current with increasing gain (that is, decreasing length). The two dominant reasons are first, the increasing width of the gain spectrum, and second, large contributions from amplified spontaneous emission caused by the large relative width of the devices, especially for the short lasers. The ob-
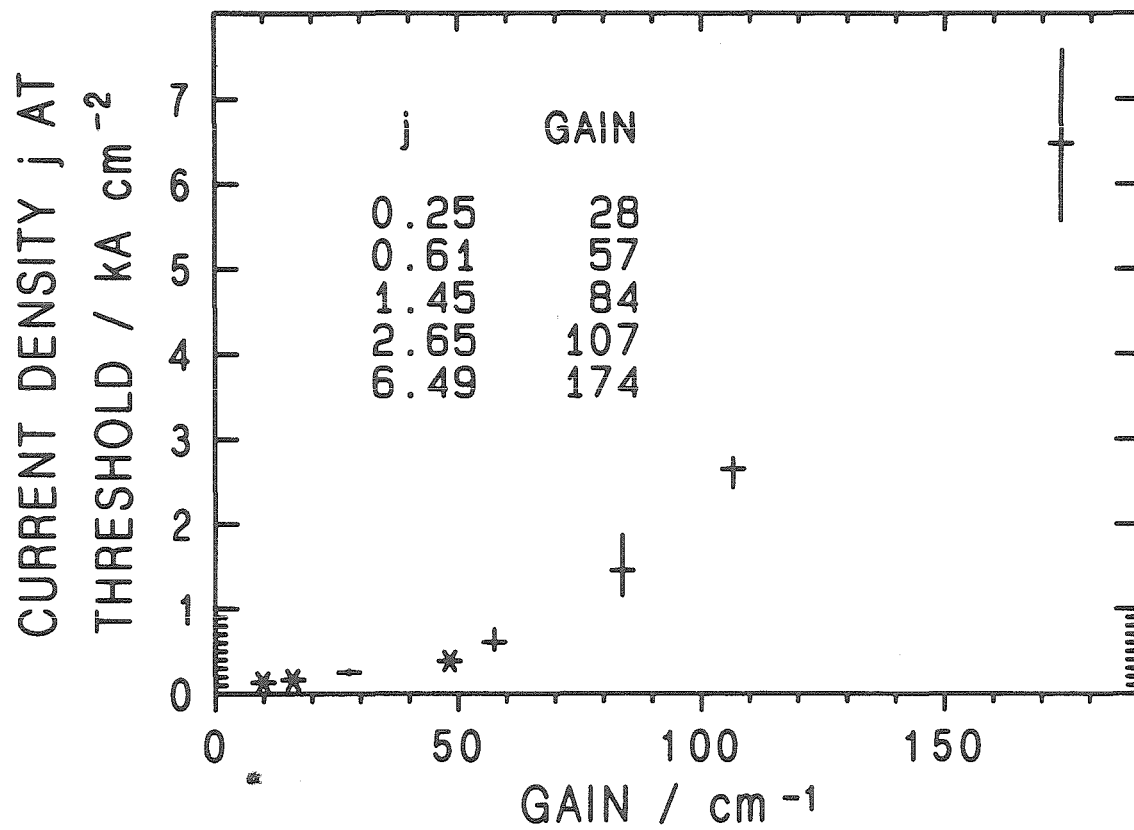
Figure 5.5 Threshold current density versus lasing gain measurements. For explanation, refer to text.
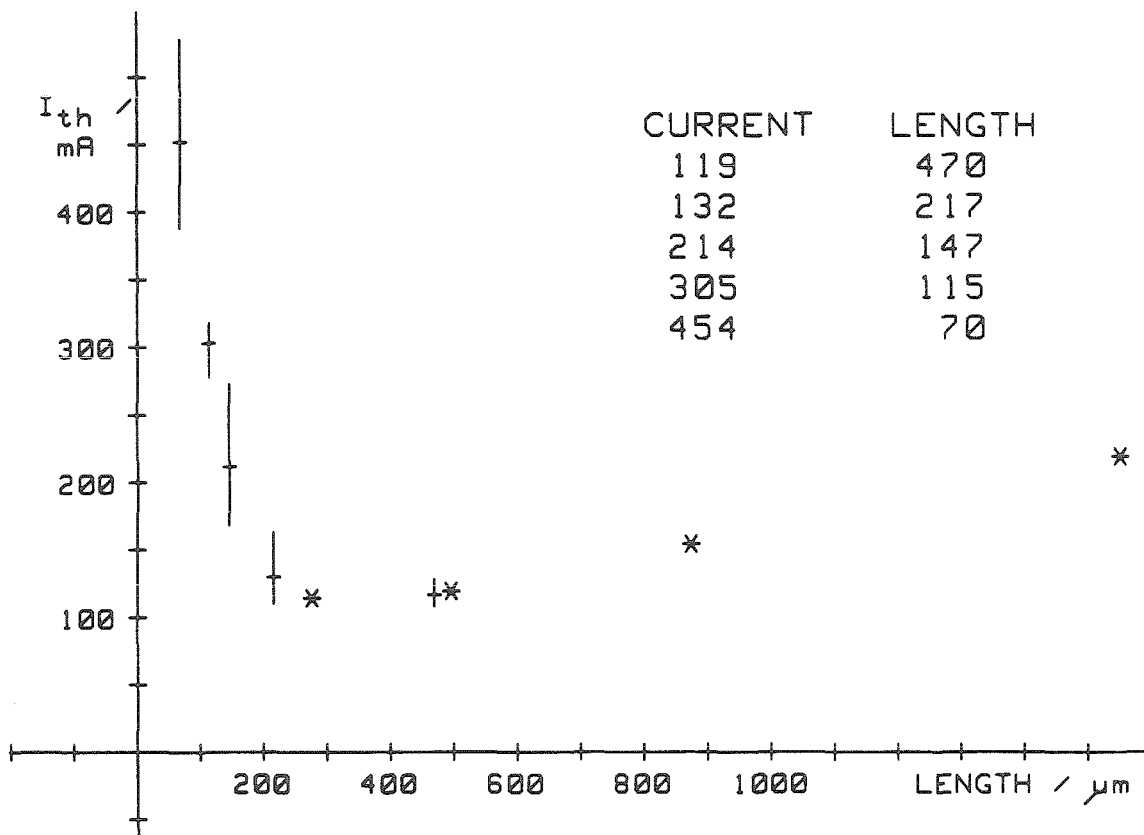
Figure 5.6 Threshold current versus laser length measurements. The bars indicate the spread of the data; the stars are results for individual devices.

served dependence of threshold-current density on the laser gain is shown in *Figure 5.5*. In *Figure 5.6* the actual threshold current for the broad area lasers is given. Again, the vertical bar indicates the *spread* of the data, while the horizontal bar gives the average value. The threshold current was determined from the first rapid change in intensity of any longitudinal mode with small increases in current. This method was necessary to determine the threshold since the short devices exhibited a high, spectrally integrated light intensity at threshold (about 10 mW for 100 μm width caused by the wide gain spectrum as explained above). It should be noted that the very high threshold-current densities limit measurements far above threshold. Thus, the conventional method of linearly extrapolating the light-current curve would be inaccurate for the short devices. This restriction does not apply for longer devices, and results of some individual lasers are shown as asterisks in *Figure 5.5*.

5.6 Conclusions

The lasing of a current-pumped, single-quantum-well laser from the second quantized state was demonstrated. A simple model explains the threshold current and spectral characteristics of the effect, especially the discontinuous change in lasing wavelength. The qualitative agreement of the presented measurements with the introduced model is good, and leaves little doubt concerning the participation of the second quantized state in the lasing at short wavelength.

The presented model is consistent with the qualitative features of the threshold current. The theoretical treatment of the threshold-current density as a function of gain is more complicated than that described above to explain the dependence of the oscillation wavelength on the gain. For the high-loss devices, it must take into account the density-of-states function at energies above the quantum well and

is thus a sensitive function of the transverse Al-profile outside the well region. Such analysis is described in *Chapter 6*. The considerations and data presented in this chapter have a strong bearing on the design for extremely short quantum-well lasers and on the quest for short-wavelength semiconductor lasers.

5.7 References

[1]. Mittelstein M., Y. Arakawa, A. Larsson, and A. Yariv: *"Second quantized state lasing of a current-pumped, single-quantum well laser."* XIV International Quantum Electronics Conference, PD16 (1986).

[2]. Arakawa Y., and A. Yariv: *"Theory of gain, modulation response and spectral linewidth in AlGaAs quantum-well lasers."* IEEE J. Quantum Electronics, QE-21, 1666 (1985).

[3]. McIlroy P.W.A., A. Kurobe, and Y. Uematsu: *"Analysis and application of theoretical gain curves to the design of multiquantum-well lasers."* IEEE J. Quantum Electronics, QE-21, 1958 (1985).

[4]. Zory P.S., A.R. Reisinger, L.J. Mawst, G. Costrini, C.A. Zmudzinski, M.A. Emanuel, M.E. Givens, and I.J. Coleman: *"Anomalous length dependence of threshold for thin quantum-well AlGaAs diode lasers."* Electronic Letters 22: 475 (1986).

[5]. Zory P.S., A.R. Reisinger, R.G. Waters, L.J. Mawst, C.A. Zmudzinski, M.A. Emanuel, M.E. Givens, and J.J. Coleman: *"Anomalous temperature dependence of threshold for thin quantum-well AlGaAs diode lasers."* Appl. Phys. Lett., 49:16-18 (1986).

[6]. Shealy J.R.: *"Optimizing the performance of AlGaAs graded-index separate confining heterostructure-quantum-well lasers."* Appl. Phys. Lett., 50:1634-1636 (1987).

[7]. Patel N.B., T.J.S. Mattos, F.C. Prince, and A.S. Nunes, Jr.: *"Narrow stripe

graded barrier single-quantum-well lasers - Threshold current considerations."
IEEE J. Quantum Elect., QE-23:988-992 (1987).

[8]. Nagle J., S. Hersee, M. Krakowski, T. Weil, and C. Weisbuch: *"Threshold current of single-quantum-well lasers: The role of the confining layers."* Appl. Phys. Lett., 49:1325-1327 (1986).

[9]. Tokuda Y., T. Matsui, F. Fujiwara, N. Tsukuda, and T. Nakayama: *"Lasing wavelength of an asymmetric double quantum-well-laser diode."* Appl. Phys. Lett., 51:209-211 (1987).

[10]. Yuasa T., T. Yamada, K. Asakawa, S. Sugata, M. Ishii, and M. Uchida: *"Short cavity GaAs/AlGaAs multiquantum-well lasers by dry etching."* Appl. Phys. Lett., 49:1007-1009 (1986).

[11]. Tokuda Y., K. Fujiwara, N. Tsukada, K. Kojima, and T. Nakayama: . *"Carrier-temperature and wavelength-switching in GaAs single-quantum-well laser diode."* Japanese J. Appl. Phys. 11:L931-L933 (1986).

[12]. Larsson A., M. Mittelstein, Y. Arakawa, and A. Yariv: *"High-efficiency, broad-area, single-quantum-well lasers with narrow, single-lobed far-field patterns prepared by molecular beam epitaxy."* Elect. Lett., 22:79 (1986).

[13]. The effect of changing S is primarily a vertical shift of the curve in *Figure 5.1*, while leaving its characteristic features unchanged. The value of $S = 0.55...0.7$ is more consistent with the majority of recent determinations; $S = 0.85$ is used because it was originally used and is a good value for this crude model because it provides about the right ratio for the effective masses. However, the model is too simple to draw conclusions regarding the appropriate value of S.

<div align="right">Chapter Six</div>

6: Gain Spectra of Quantum-Well Lasers

Abstract

A model for quantum-well lasers is introduced. The phase-density method described in the appendix is used to find the eigenfunction and eigenvalues for the charge carriers and the optical modes of the transverse structure under flatband conditions. The two-dimensional density of states for the charge carriers and the effective width of the optical mode are identified as the relevant parameters for gain calculations. An effective density of states is introduced to avoid the unsatisfactory use of the Lorentzian broadening. Quasi-Fermi levels and selection rules for the transitions are considered. The modal gain as well as the threshold-current-density is derived by applying the Einstein coefficients for the two-level system to the interband transitions in semiconductor lasers.

6.1 Introduction

Quantum-well structures have been realized in semiconductor material since 1974. Continuous crystal heterostructures have been grown, with variations of the material composition in one dimension on a scale so small that quantum effects are achieved [1-4]. The fabrication of these structures with low defect density led to superior characteristics in several laser parameters. On the other hand, the specific properties of quantum-well lasers are not generally appreciated, as yet. Quantum-well lasers are an evolutionary step in the development of semiconductor lasers, whose significance is comparable to that of the introduction of the double heterostructure.

The starting point for the experimental investigation of quantum-well structures in semiconductor material, and in lasers in particular, is the ability to produce heterostructures with a precision of one atomic layer. This precision corresponds to one-half a lattice constant in GaAs/GaAlAs material in the [100] direction, which is the most often used growth orientation. There are several systems that can perform this task. Among them are molecular beam epitaxy (MBE) [5, 6] and metalorganic chemical vapor deposition (MOCVD) [7, 8] systems. Today's high-quality materials possess high luminescence intensity, indicating that the crystal has low defect density. The high quality of state-of-the-art material allows the properties of the structure to be investigated without having the results heavily modified by imperfections.

In the following, the basic theoretical model of quantum-well lasers is developed, as it is used in this thesis. *Chapter 5* included a simple model of a single-quantum-well laser used to explain the experimental findings for the second quantized-state lasing. In this chapter, a more detailed model is developed, which is powerful enough to predict specific properties of quantum-well lasers. The model introduced in this thesis is substantially similar to models introduced elsewhere [9-15]; it differs, however, in several key aspects. New concepts in the calculations of the gain spectrum and the threshold-current density are introduced, which eliminate unsatisfactory methods used previously.

Fundamentally, the quantum-well laser is similar to the conventional, double-heterostructure laser, apart from the special effects of the very small layer thickness. In this chapter, the consequences of closely spaced interfaces that are due to the very small layer thickness, the fundamental property of quantum-well structures, are investigated.

The extreme confinement of the electrons and holes in one direction, the direction of the *very small layer thickness*, implies that the electron and holes behave as free particles only in the *two* dimensions normal to the quantization direction. The specifics of the confinement are included in the treatment of the third dimension. In the limit where the confinement distance approaches infinity, the theoretical results of the model merge with those of a conventional, three-dimensional semiconductor model. The infinite (or at least large) amount of space in a given dimension allows the continuum approximation to be used. *It is the validity of this approximation that ceases in the transition to small layer thicknesses.*

In the following, it is shown how to find the transverse eigensolutions for the electrons and holes in and near the quantum well. A one-dimensional structure of very small width is treated and then its solutions are combined with the two-dimensional continuum solutions to find the density-of-state function for the quantum-well structure. The effective transverse mass is introduced, a quantity that carries over from the solution of the one-dimensional problem into the effect that the two-dimensional solution has on the density of states. The effective width of the electromagnetic mode and the dependence of the modal gain on the lateral structure are discussed.

6.2 Eigensolutions of the Transverse Structure

The formalism of the transverse eigensolutions for the charge carriers and for the electromagnetic mode are very similar, which simplifies the algorithm to calculate the gain spectrum. Consequently, there is a scaling implied via the relation of the potential and the index of refraction, both as a function of the Al-concentration (refer to *Chapter 7.8*).

For the charge carriers, the eigensolutions are found by solving the Schrödinger equation for the eigenfunction $\psi(x)$ with the eigenenergy E. The equation accounting for a material-dependent effective mass is:

$$\frac{-\hbar^2}{2} \cdot \frac{d}{dx} \frac{1}{m(x)} \frac{d}{dx} \psi(x) + V(x) \cdot \psi(x) = E \cdot \psi(x) \qquad (6.1)$$

This is the envelope effective mass approximation with continuous probability current density [16]. The effective mass is a function of the Al-concentration, which changes in the transverse direction in the double heterostructure or quantum-well structure. The Al-concentration profile is the primary means of localizing the region of recombination of charge carriers, the region of gain. In general, the potential is a "well shape", implying confined states. For the electromagnetic mode, the eigensolutions are found by using the Helmholtz equation for the eigenfunction $\psi(x)$ with the eigenpermittivity E. Without going into all the details of setting up Maxwell's equations and the material properties of a nonmagnetic material, with no effective free-charge density and no effective current density but only piecewise constant permittivity, the one-dimensional, transverse eigenvalue problems are solved approximately by the following eigenequations for the TE-modes (the observed lasing mode):

$$\frac{1}{k_0^2} \cdot \frac{d^2}{dx^2} \psi(x) + \varepsilon(x) \cdot \psi(x) = E \cdot \psi(x) \qquad (6.2)$$

while the TM-modes are found from the following equation:

$$\frac{1}{k_0^2} \cdot \frac{d}{dx} \frac{1}{\varepsilon(x)} \frac{d}{dx} \varepsilon(x) \cdot \psi(x) + \varepsilon(x) \cdot \psi(x) = E \cdot \psi(x) \qquad (6.3)$$

where k_0 is the free-space wave vector, introducing the photon-energy dependents of the eigensolutions of the Helmholtz equation via $E_{ph} = \hbar \cdot c \cdot k_0$. The solutions of the transverse electromagnetic problem of physical interest are the guided modes of the laser. For these modes the active layers provide sufficient gain to compensate

for all distributed losses and provide growth of the optical power in the mode upon propagation for useful output at lasing. However, a real-valued eigenvalue problem is much easier to solve than the full problem with gain and loss. The resulting optical mode pattern of a typical structure has been found to change insignificantly upon neglecting gain and loss, provided that the boundary conditions are corrected. Physically, the active layers provide photons of which a fraction is lost by penetrating the barriers and radiating out. The cladding layers are the mentioned barriers. Mathematically, this penetration can be expressed in the real-valued eigenvalue problem by the boundary condition that the intensity functions are monotonously decreasing in the cladding layers with increasing distance from the active layers.

The potential for a heterostructure confining electrons and holes is lower in the center than in the cladding, while the permittivity, in contrast, is higher in the center than in the cladding. This opposite behavior coincides with the opposite sign in *Equation 6.1* in contrast to *Equations 6.2* and *6.3*. The material properties are causal for all modern semiconductor lasers because they allow a structure to confine both, an electromagnetic mode as well as the charge carriers.

In this thesis, the Al-concentration will be taken as a piecewise constant as a result of the steplike representation of Al-concentration in the transverse profile. In practice, the Al-concentration can be made to change gradually as well as abruptly. This approach is chosen so that the solutions to the differential equations are simple; they are either sinusoidal, linear, or exponential. Therefore, the eigenfunctions can be described as simple, piecewise analytic functions. Consequently, calculation of high precision can be achieved for a small number of subintervals for the region of interest. The details of finding the eigenfunctions and eigensolutions of the trans-
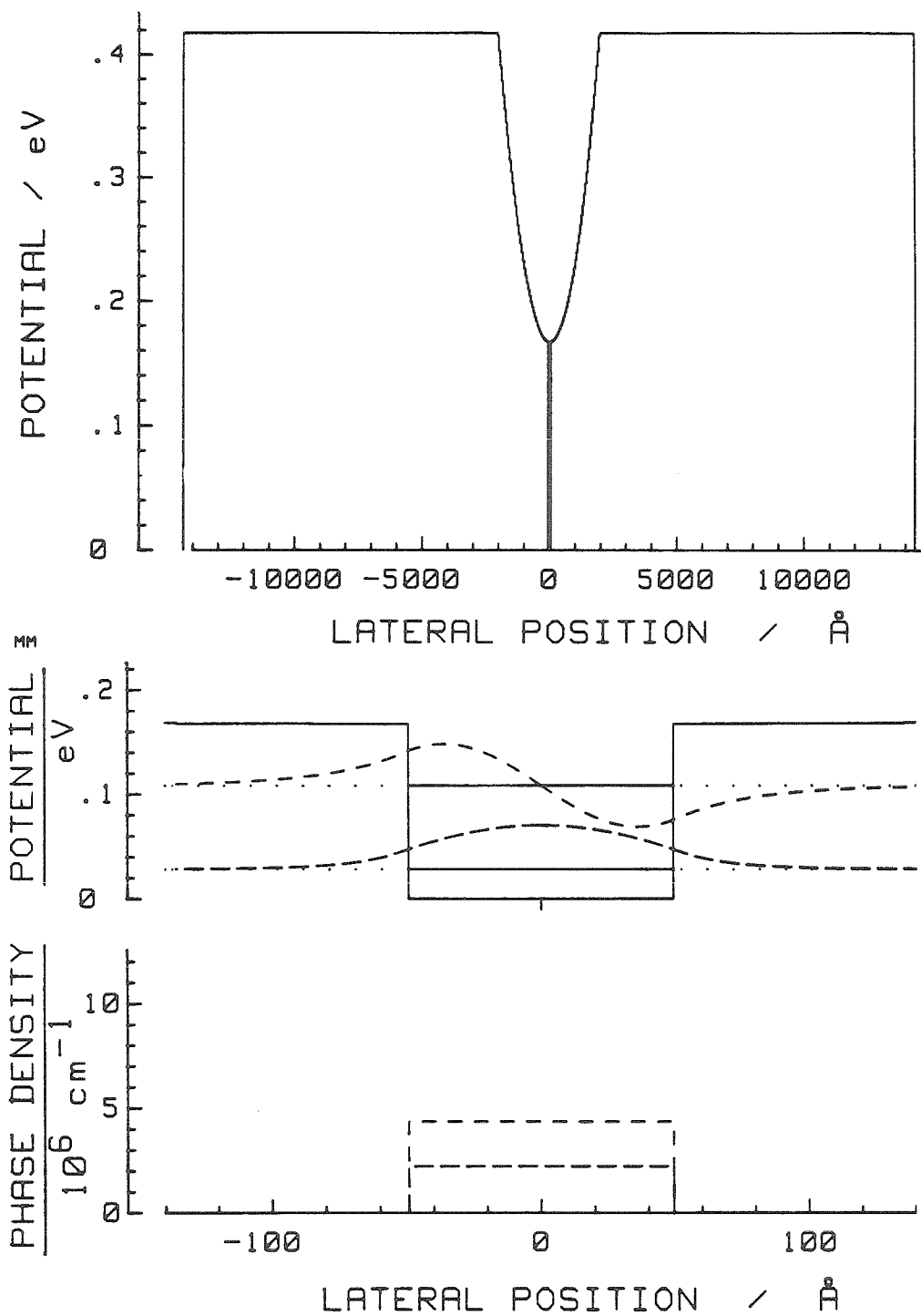
Figure 6.1 a. Overall transverse structure in the potential of the electrons. **b.** The central portion enlarged as well as the eigenvalues and the eigenfunctions for the lowest two confined states. **c.** Phase density corresponding to these two eigenfunctions.

verse structure according to *Equations 8.1, 8.2,* and *8.3* are given in the *Appendix* (*Section 6.8*).

6.3 Static Density-of-States Function

The density of states in the quantum-well laser is the two-dimensional density of states obtained by integrating out the third dimension (the direction of strong confinement). That third dimension governs the onset of the subbands, each of which is a Heaviside-like density-of-states function.

In *Figure 6.1a*, an overall transverse structure is presented; the potential for the electrons is shown. *Figure 6.1b* shows just the inner region of the confining structure, and the eigenvalues and eigenfunctions of the two energetically lowest eigenfunctions are shown. In this plot the realistic boundary effects are evident, in contrast to *Figure 5.2*. In *Figure 6.1b*, the first two eigenfunctions have phase in the quantum well of $0.702 \cdot \pi$ and $1.371 \cdot \pi$, respectively, while in *Figure 5.2*, the phases are π and $2 \cdot \pi$ because of the very simple model. *Figure 6.1c* shows the rate at which the phase varies with a change of position.

In this more realistic model, the eigenenergy is reduced from the value predicted from the simple box model in extreme cases to almost the value predicted by the simple model for the next lower quantum number. The effect that the integrated phase inside the quantum well is smaller than $n \cdot \pi$ and, consequently, that the eigenenergy is reduced, is significant in actual devices when quantum effects are noticeable.

The functional behavior of the masses has to be given. The relations of energy and wave vector of the charge carriers are, in general, complicated; however, in
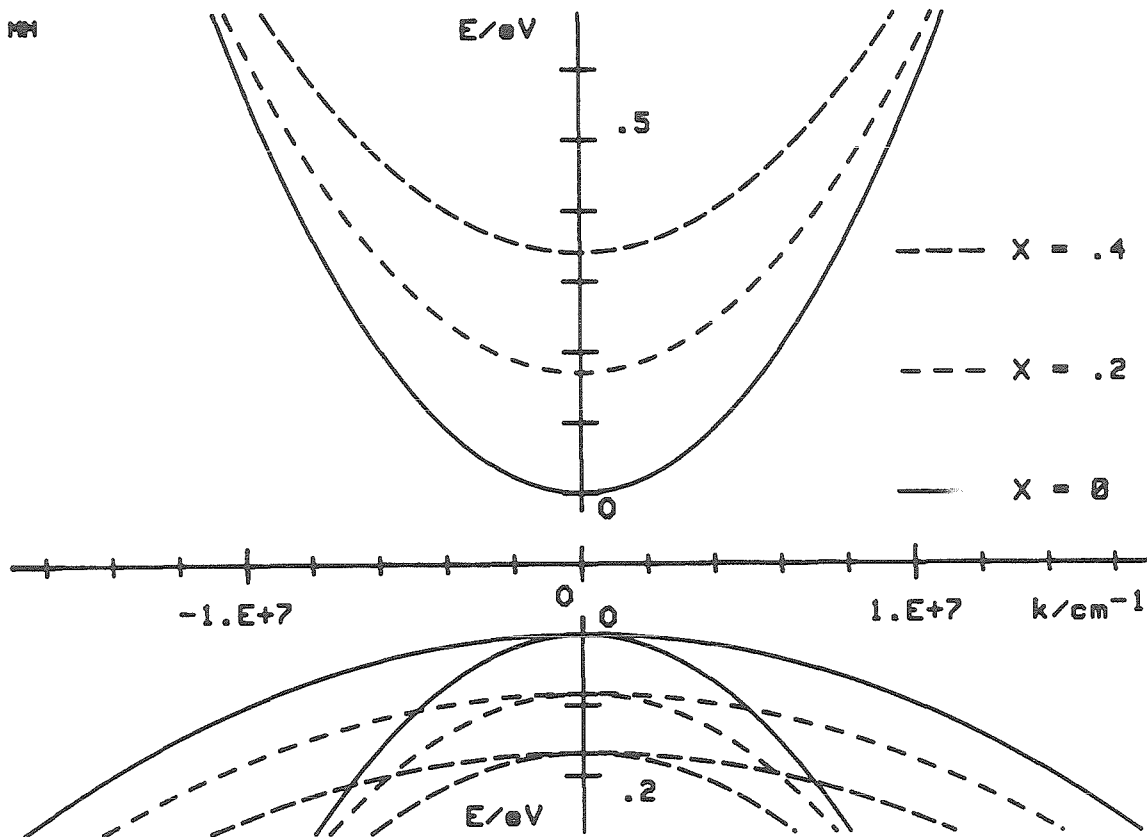
Figure 6.2 Scale drawing of the dispersion relation of the parabolic band approximation (as used in this thesis), k versus E. E is the energy in the conduction band shown upward in the upper half of the figure and E is the energy in the valence band shown downwards in the lower half of the figure. Three Al-concentrations (X) are shown. The k-vector is the two-dimensional in the-plane-of-the-layers vector; therefore, the drawing represents a cross section.

particular, near the direct bandgap of GaAs and GaAlAs with an Al-concentration smaller than 0.42, the band structure is close to parabolic; that is, the relation of energy and wave vector is approximately:

$$E = E_0 + \frac{\hbar^2 \cdot k^2}{2 \cdot m_{eff}} \tag{6.4}$$

where E_0 is the energy at the extreme, basically defining the offset of the energy scale, and m_{eff} is a fitting parameter with the dimension of mass. This parameter is called the *effective mass*, m_{eff}; it will be used in this thesis most often in the form of a number, M_{eff}, times the rest mass of the electron ($m_{eff} = M_{eff} \cdot m_e$). The approximation of using a constant parameter for every band (here, the electron, light-hole, and heavy-hole band) and Al-concentration, resulting in a parabolic $E(k)$, is called the *parabolic band approximation*. It also approximates the semiconductor crystal to be *isotropic*. Here, the parabolic band approximation will be used, which is more a means of making the problem tractable than of finding a precise solution. *Figure 6.2* is a scale drawing of the energy versus the k-vector, in the plane-of-the-small-layer thickness for several Al-concentrations. Several more sophisticated models have been presented in the literature [17, 18], but will not be incorporated, in order to stay within the scope of this thesis.

The advantages of using the parabolic band approximation are that the problem remains one-dimensional, and the side effects on the conjugated, two-dimensional problem are minimal. The parabolic band approximation is significant, especially for the electrons. For Al-concentrations in excess of about 0.42, the band structure in the conduction band causes the transition to be indirect; that is, the lowest electron energy is not the point at which the in-plane k-vector vanishes. Again, for the sake of manageability, the parabolic band approximation will be used.

The associated two-dimensional problem remains to be resolved. Fundamental

considerations give, for a spatial extent L, an eigenstate every $\frac{2 \cdot \pi}{L}$ in each direction of the wave-vector space. Each of the states in k-space can be occupied by two fermions because of the possible spin orientations. The number of states per area (N') with the k-value below the upper limit (k_{max}) is given in *Equation 6.5*. Via the parabolic band approximation, k_{max} corresponds to an upper energy E_{max},

$$N' = \frac{N}{L_1 \cdot L_2} = 2\pi \cdot \left(\frac{k_{max}}{2\pi}\right)^2 = \frac{1}{2\pi} \cdot \frac{2 \cdot m_{eff} \cdot (E_{max} - E_0)}{\hbar^2} \qquad (6.5)$$

Therefore, the density of states per area and per energy is

$$\aleph = \frac{m_{eff}}{\pi \cdot \hbar^2} \cdot H(E - E_0) \qquad (6.6)$$

a constant apart from being zero below the onset energy E_0. In the parabolic band approximation, this is a Heaviside function $H(*)$ with a weighting function proportional to the mass. For that mass, an effective mass model in the transverse direction is employed in this thesis. The *expectation value of the effective mass for the one-dimensional (transverse) solution* is used; that is, the value depends on the Al-concentration profile as well as on the eigensolution of the transverse potential profile. The onset energy of the Heaviside function is the eigenvalue of the one-dimensional problem. This model is compatible with large structures, also. For instance, for a large, flat-bottomed box, the boundaries are far apart, and the effective mass approaches the effective mass of the bottom of the box as it would for the three-dimensional case; therefore, the solution merges into the solution of the large-scale continuum approximation mentioned above.

Basically, the description of a state is changed from specifying its three components of the k-vector to specifying its two components of the in-plane k-vector and its quantum number, n. This quantum number is in general *not* associated with the value of a transverse k-vector. In the case of an underlying structure of constant

potential over nearly all its transverse width, however, an association is suggested. In that case, which does not include quantum wells, the phase density is constant over nearly all the transverse structure and therefore, the transverse k-vector and the eigenenergy are nearly equal to the value associated with that k-vector. Therefore, the very small layer thickness introduces effects that cause the character of the eigenstates to be different from what an equally thick piece of bulk would suggest.

6.4 Effective Density-of-States Function

In this section, the effective density-of-states function based on the static density of states (*Section 6.3*) is introduced. The effective density of states is introduced to model collective and dynamic effects of the large number of charge carriers, electrons in the conduction band and holes in the valence bands, in inverted semiconductor material. It should be noted that both heavy and light holes are considered and the split-off band is neglected in the model. The error introduced by neglecting the split-off band is estimated to be smaller than the error introduced by using the parabolic band approximation.

First, the *intraband* relaxation time will be introduced as a dynamic effect, achieving a change in the effective density of states with respect to the static density of states. This approach is conceptually different from the commonly used models where a Lorentzian broadening is introduced in the effect which the static density of states has on the gain. It should be noted that several predictions of the commonly used model are close to the observed properties of devices, for instance, the rounding of sharp features in the gain spectrum as predicted from the static density of states alone. But the model using the Lorentzian broadening of the transition produces errors of more than an order of magnitude in some subtle properties, for instance,

the spectral transition rate near the transparency region of the energy gap, which a correct broadening model should be able to predict.

The approximations involved in applying the Lorentzian broadening are to be examined. The Lorentzian broadening is the standard method of incorporating the finite lifetime of the transition in a two-level system. The time evolution of a two-level system with a finite lifetime, τ, starting at $t = 0$ from a single occupation of the excited state, is as follows. Quantum-mechanically an $e^{-t/\tau}$ probability of remaining in the excited state is superimposed on a $1 - e^{-t/\tau}$ probability to be in the ground state, for the case in which no re-excitation is considered. In this case, the Fourier transformation of the amplitude function results in a Lorentzian-broadened energy spectrum of the transition energy proportional to $[(E - E_0)^2 + (\frac{\hbar}{2\tau})^2]^{-1}$. The full width at half maximum (FWHM) of the above Lorentzian is $\frac{\hbar}{\tau}$. A prerequisite of applying the Lorentzian broadening is that the broadening in energy is very small compared to the energy splitting of the two levels. Otherwise, the description involves a significant contribution of negative energies for a transition from the higher- to the lower-energy state, which is physically unreasonable. For the simple exponential description introduced above, the uncertainty in energy is associated with the limited lifetime of the inverted state (energy and time are conjugated variables with respect to Heisenberg's uncertainty principle). This is a suitable description for the spontaneous emission in a laser, where the two levels are the upper- and lower-energy level of the lasing transition, and the rate is associated with the transition rate between these two levels.

A Lorentzian-broadening function is commonly used to describe the lasing transition. For the valence band and for the conduction band, an *intraband* transition rate has been identified; quoted values are near $\frac{1}{0.1\ ps}$ for both. These transition

rates within each of the bands will cause an uncertainty in the energy. For a transition rate of $\frac{1}{0.1\ ps}$ (corresponding to an energy breadth of $\Delta E = 6.6\ meV$), the dipole approximation is good if the transition energy is large compared to $\Delta E \cdot \left(\frac{3}{4}\right) \cdot 137$ [19], that is, about $\frac{2}{3}\ eV$. An example of intraband transitions with energies larger than $\frac{2}{3}\ eV$ is excited-state absorption. These processes exhibit a rate far smaller than the quoted $\frac{1}{0.1\ ps}$ (otherwise, lasing would not be possible because these processes present absorption). Consequently, there is no physical justification to apply the dipole approximation with a 0.1 ps lifetime to the *interband* transition in semiconductor lasers.

If broadening causes the density of effective states to be reduced by a factor of two, this reduction happens in the conduction band as well as in the valence band. Therefore, the transition rate is reduced by a factor of four, unless the reductions in the density of states are correlated. The commonly used model reduces the transition rate by a factor of two, not four. Another element of the commonly used model is that broadening is introduced after the population of the available states is considered. To justify this approach, it has to be reasoned that the thermal distribution is established slowly compared to the broadening.

In conclusion, the commonly used model of Lorentzian-broadened, interband transitions can be used for several general features, but in detail it is unsatisfactory theoretically and experimentally. The concerns with the commonly used model are mainly that the Lorentzian broadening has very long wings; that is, even several FWHM away from the center the contribution is still significant. Secondly, the uncertainty introduced in the energy of the states is reflected only in the transition, not in the density-of-states function. Both of these shortcomings can be overcome in a heuristic model, introducing an effective density of states, essentially a smeared-out
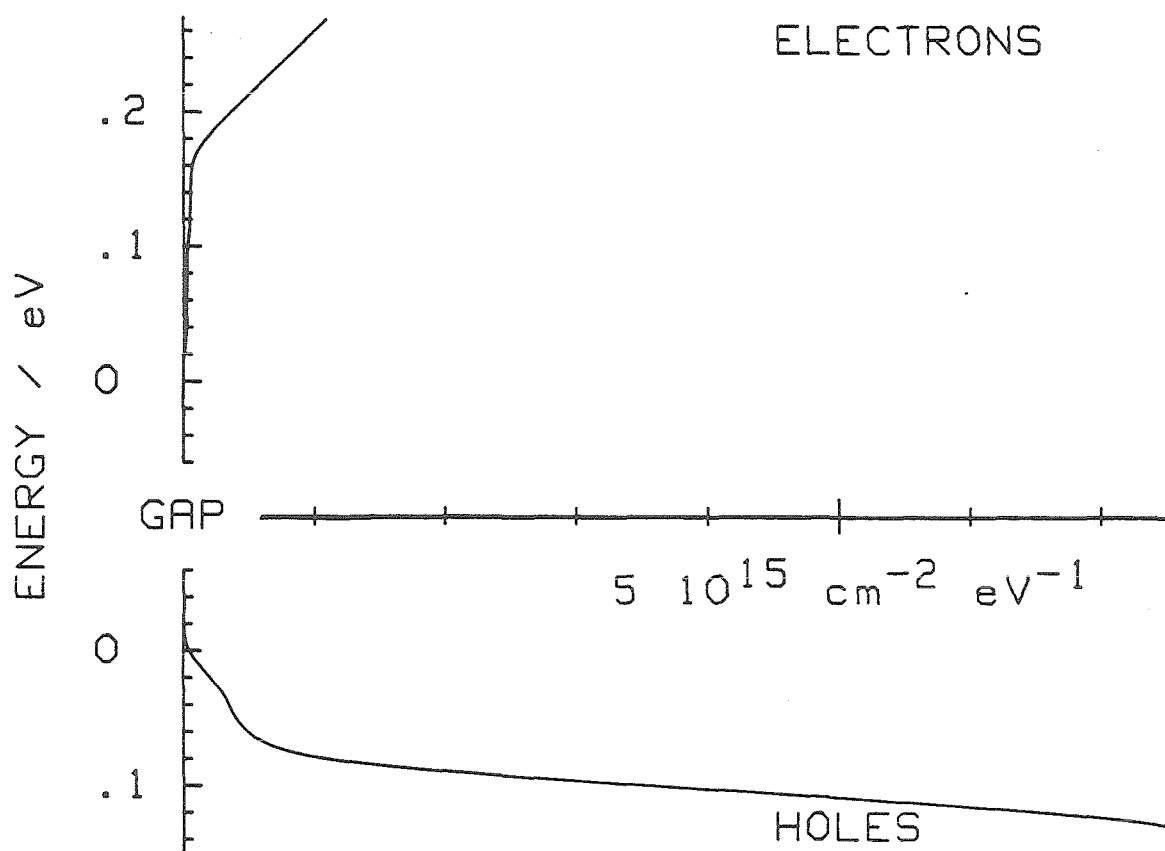
Figure 6.3 Effective density of states for a structure as in *Figure 6.1*. The smearing of the onset of the subbands is evident; the scale does not allow the effect of the outer parabolic structure on the density of states in the valence band to show but makes the quantum well in the conduction band hardly visible (for a scaled version refer to *Figure 6.5*). Note the drastic asymmetry of the small density of states in the conduction band as compared to the large density of states in the valence band.

version of the original density of states with a smearing function with exponential tails, rather than the subexponential tail of the Lorentzian, and not as radical as the superexponential tails of the Gaussian distribution.

A distribution whose cumulative value is a function like one minus the Fermi function is a distribution that satisfies these conditions; it is a function with a single, adjustable parameter, which is the width of the transition ΔE. Therefore, the two-dimensional, static density-of-states function is replaced by the two-dimensional, effective density-of-states function.

$$D_{st}(E) = C \cdot \sum_{i=1}^{N} M(i) \cdot H(E - E(i))$$

$$\Downarrow$$

$$D_{eff}(E) = C \cdot \sum_{i=1}^{N} \frac{M(i)}{1 + e^{\frac{E(i)-E}{\Delta E}}} \tag{6.7}$$

where $H(*)$ is the Heaviside function, and $E(i)$ and $M(i)$ are, respectively, the eigenvalues of the transverse potential and the transverse expectation value of the mass of the charge carrier in units of the rest mass of the electron m_e. The C includes the fundamental constants, $C = \frac{m_e}{\pi \hbar^2} = \frac{2.607 \cdot 10^{37}}{m^2 \cdot J} = \frac{4.18 \cdot 10^{14}}{cm^2 \cdot eV}$. The resulting effective density of states for a structure (as in *Figure 6.1*) is shown in *Figure 6.3*. The effective density of states are used in the model introduced in this thesis. It will be adapted in the model; no further broadening will be considered. This functional form has been published (refer to [20], also to *Chapter 5*).

Recently, the phase damping of optical dipole moments and gain spectra in semiconductor lasers were discussed by Yamanishi and Lee [21]. They included non-Markovian processes in the model of the relaxation phenomenon and ended up with a line shape shown together with the Lorentzian, Gaussian, and the broadening
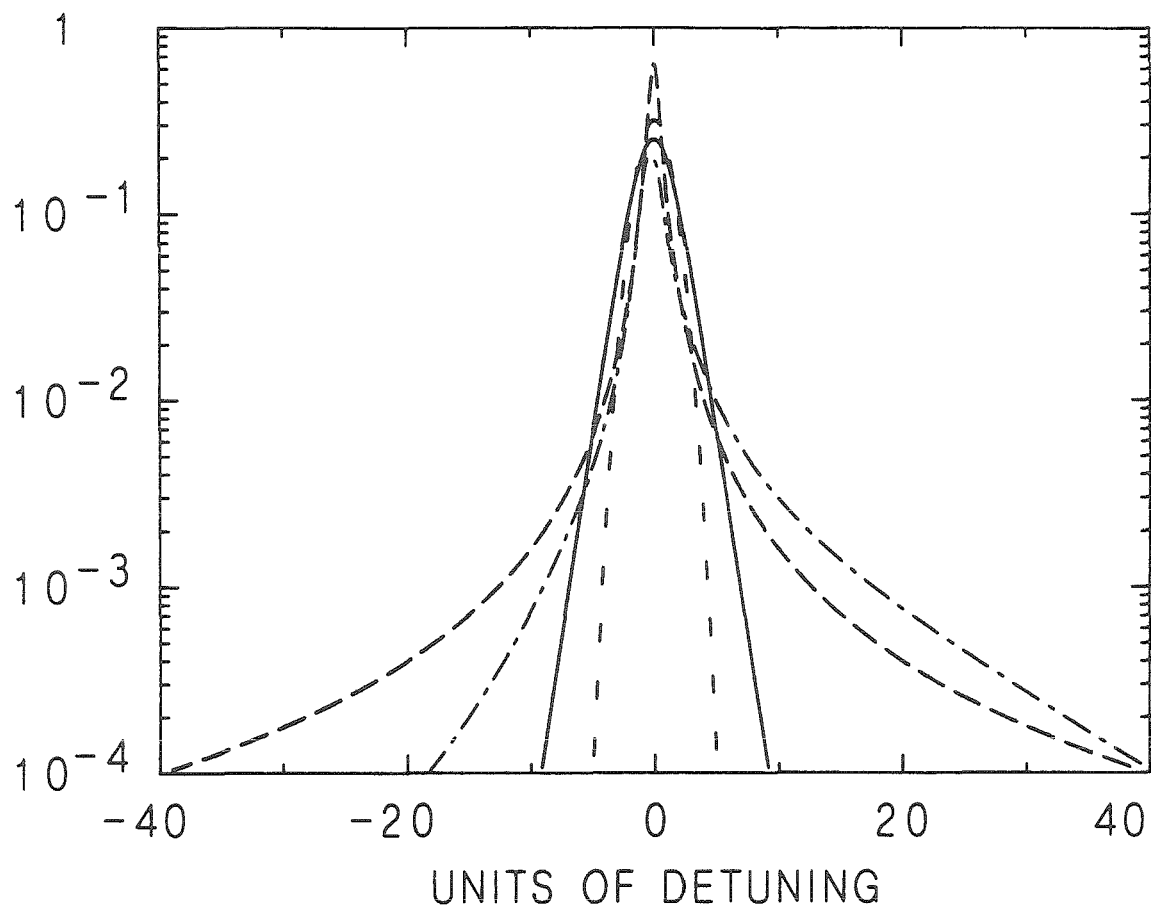
Figure 6.4 Comparisons of broadening functions, the density versus detuning is shown. The Lorentzian (long dash) with its long tails and the Gaussian (short dash) with its superexponential tails are the extreme cases. The asymmetric curve by M. Yamanishi and Y. Lee (dotted dash) [12] is derived by including non-Markovian processes in the relaxation model. Finally, the heuristic model (solid curve) introduced in this thesis shows exponential tails.

introduced in the thesis in *Figure 6.4*. Their model is beyond the scope of this thesis and is not incorporated.

There are two more mechanisms by which the effectiveness of the density of states is altered. Both of them change the effective potential and therefore the static density of states has to be recalculated. The process becomes involved because self-consistency is required in this highly nonlinear problem. The first effect is called bandgap renormalization or energy-gap shrinkage [22]; it is caused by the fact that the conditions for finding the density of states are dependent on the number of occupied exceeded states. It has been demonstrated, experimentally, that the bandgap shrinkage can be as large as 50 *meV* [23].

The second effect is that any considerable occupation of states leads to a non-balanced spatial distribution of the negative and positive charge carriers across the small confining structure and across the regions of the barriers nearby. This effect is caused by the different effective masses of the electron and holes and by the different changes of the potential that are due to changes in the Al-concentration, resulting in different penetration into barriers and bounding regions for the transverse eigen-functions of the electron and the holes. The consequence is a substantial electrical potential, which is in such a shape as to reduce the asymmetry.

6.5 Quasi-Fermi Levels and Selection Rules for Transitions

Above, the density-of-states function has been discussed, including its modification that is due to the high density of occupation for energetically higher states. It was emphasized that an imbalance of negative and positive charge carriers will create an electrical field and, thereby, electrical potentials. In applications as in quantum-well lasers, the fields outside the confining structure are small (caused by

high conductivity of the material); therefore, the density of negative and positive charge carriers integrated across (transverse) the confining structure has to vanish or very nearly vanish.

It is customary to specify the density of carriers, that is, occupied states as a density in three dimensions in semiconductor lasers; however, it is evident that this way of quoting densities is useful only when the density is nearly constant over the region of interest; otherwise, the spatial profile needs to be discussed. The condition of uniformity is approximately fulfilled for thick active regions, but they are the very ones that do not show the quantum effects. For thin active regions (that is, < 200 $\mathring{A}$ at room temperature), which show the quantum effects, the density of carriers is a continuously varying transverse function.

The three-dimensional, density-of-states function is not distinctive for quantum wells and tends to encourage viewing the quantum well as a thin piece of bulk material, which excludes rather than emphasizes the specific characteristics. By integrating over the transverse dimension, that is, the continuously varying spatial distribution, the two-dimensional density-of-states function is found. However, it is easier to start directly with the characteristic, two-dimensional density-of-states function as has been done in previous sections. The two major reasons why the two-dimensional density is more useful are as follows: First, the current pumping the structure enters as a two-dimensional current density, and second, it is not the three-dimensional density of states that enters in the gain, but the two-dimensional one as will be described below.

The two-dimensional density of occupied states (electrons in the conduction as well as holes in the valence band) is found by integration over energy of the effective

82
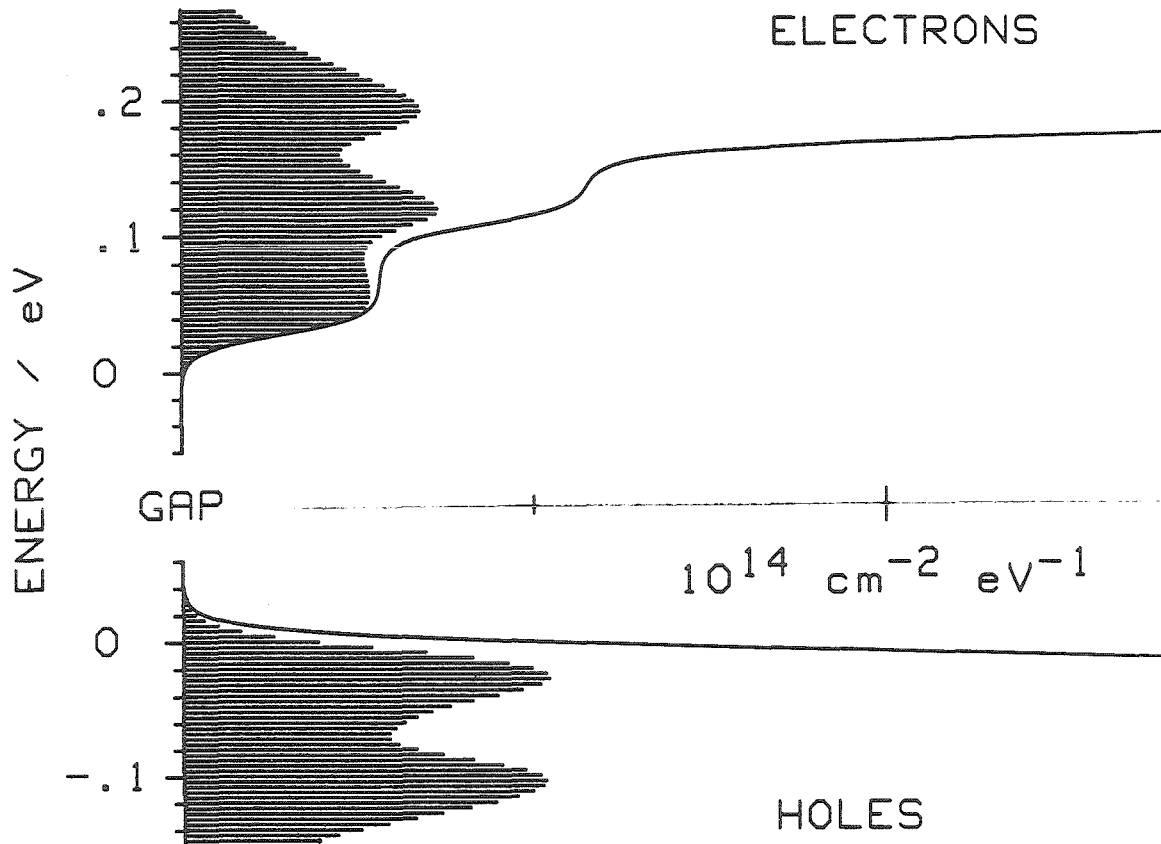
Figure 6.5 Effective density of state for a single quantum-well structure (Scaled from *Figure 6.3* by a factor of 42). The distribution of occupied states for a particular density of occupied states is indicated by shading. This occupation gives inversion providing 30 $\frac{1}{cm}$ gain for the optical mode. Note the considerable occupation of energetically high states that contribute to the threshold current but not to the gain. The quasi-Fermi energies are 0.14 *eV* and −0.01 *eV* inside the conduction and valence band of GaAs, respectively. The negative value indicates that the Fermi energy of the conduction band is actually in the bandgap.
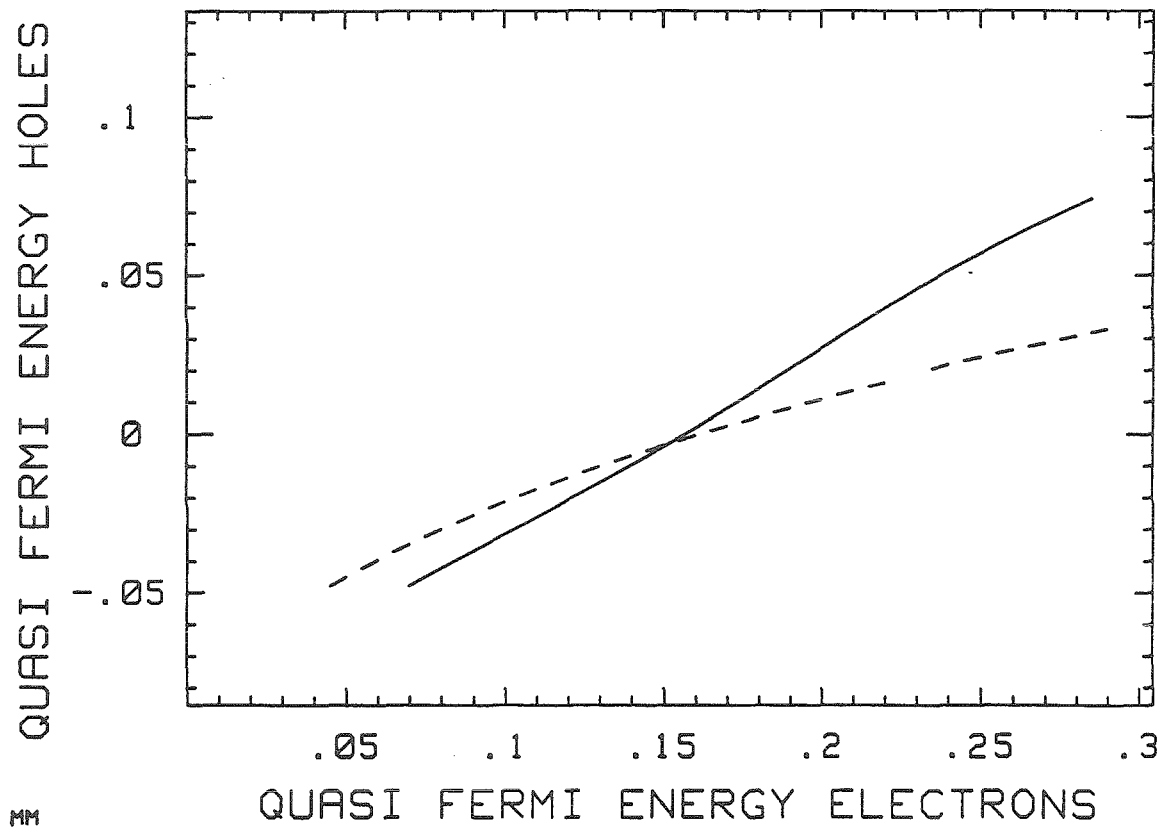
Figure 6.6 Functional relation of the quasi-Fermi energy for the conduction and valence band at room temperature for a quantum-well structure (solid) as well as for a conventional double heterostructure (dotted). For the quantum-well structure the energies are referred to the first quantized eigenenergies in the respective bands.

density-of-state function multiplied by the Fermi occupation factor.

$$\aleph_{occup} = C \cdot \int_{-\infty}^{+\infty} \sum_i^N \frac{1}{1 + e^{\frac{E - E_{Fermi}}{kT}}} \cdot \frac{M(i)}{1 + e^{\frac{E(i) - E}{\Delta E}}} dE \tag{6.8}$$

This formula applies to the conduction band with its quasi-Fermi energy and the electron eigenstates. Also it applies, separately, to the valence band with its quasi-Fermi energy and the hole eigenstates. Practically, the integration starts at an energy where the effective density of states becomes significant and will be terminated where the Fermi occupation factor becomes so small that even the increasing density of effective states cannot make the contributions significant. This is a highly accurate model because the intraband time constants for transitions toward the steady-state condition are substantially shorter (at least at threshold) than the intraband lifetime of the carriers (0.1 to 10 *ps* versus a few *ns*). Therefore, thermalization is achieved and the distribution is governed by the Fermi occupation factor. *Figure 6.5* shows the effective density of states as well as the occupied density of states as a function of energy in the valence and conduction bands of a quantum-well structure.

The necessary condition for having the charge density balanced in steady state gives a structure-dependent, functional relation between the quasi-Fermi level for the conduction and valence band. If the quasi-Fermi level of the valence band is plotted as a function of the quasi-Fermi level of the conduction band, the slope of the function is smaller than one. This asymmetry is due to the different effective masses (and the two different holes versus only one electron. Refer to *Section 7.3*). *Figure 6.6* shows this functional relation of the quasi-Fermi energies for the conduction and valence band for a conventional double heterostructure (dotted line) as well as for a quantum-well structure. An increased slope of the E_{fl} versus the E_{fh} curve of quantum-well lasers shows the influence of the states in the outer structure.

This slope indicates the transition from the effectively two- to the effectively three-dimensional structure. An idealized two- as well as a three-dimensional structure shows a slope of 0.18 to 0.19, but the onset of subbands higher than the first subband increases that value in the quantum-well laser.

To determine the gain spectrum, the selection rules for the optical transitions have to be specified. These transitions involve recombining and thereby annihilating one electron and one hole, giving up their excess energy as a photon. The photon has a small momentum compared to the states of the carriers leading to the approximate selection rule of zero difference in momentum for the electron and hole states involved. This approximation, named the *rigorous k-selection rule*, is carried over from the three-dimensional case to the two-dimensional continuum of the quantum-well structure, but in the one-dimensional associated space, it is replaced by considering all combinations of electron and hole states weighted by the overlap factor of their eigenfunctions. The conduction band states are s-functions, while the valence band states are p-functions; therefore, the transition strength scales with the spatial overlap. Often, the rule that the index of the eigenfunction has to be identical, called $\Delta n = 0$, is used, which turns out to be a good approximation in some cases (an overlap factor close to one), but in other cases it is a very poor approximation (the overlap factor is actually close to zero) because of the asymmetry of the electron and hole states.

Some authors consider the rigorous k-selection rule unreasonable because the dimensions involved are small with respect to dephasing under such a strong rule [24]. Nevertheless, the k-selection rule will be used in the model that follows.

There is one additional consideration to be made, caused by the spreading in energy. An energy difference smaller than the difference of the involved eigenenergies

of the electron and hole state is made possible, corresponding to an imaginary momentum in the two-dimensional space. Rigorous k-selection is still requested for simplicity.

6.6 Theory of the Gain Spectrum of Semiconductor Lasers

To get a quantitative evaluation of the gain, the strength of the transitions has to be determined. The strength of the contribution of a transition satisfying the rigorous k-selection rule is proportional to the overlap factor of the eigenfunctions of the involved charge carriers, the Fermi factor of the electron state, the Fermi factor of the hole state, the density of the transitions, and the square of the matrix element for the transition. The density of transitions is similar to the density of states for the carriers, which via the parabolic band approximation transforms the density of states in k-space into a density in energy. In the case of the transition, the density is lower because of the energy scales for the electron as well as for the hole. One way of expressing this is to consider the *reduced mass* of the two carriers in a formula otherwise identical to the one used to find the density of states. This is commonly referred to as *joint density of states*. If the case of the heavy and the case of the light holes are added, the density of transitions is found. Finally, the matrix element has to be specified. It is the integral over the conjugated electron-wave function multiplied by the electric dipole operator acting on the hole wave function. Its value is the charge of the electron times a distance in the order of a few $\mathring{A}$. Because the conduction band state is s-like and the valence-band state is p-like and the dipole operator is applied, the integration of the envelope functions is the direct overlap as introduced above.

There is one more quantity that enters into the modal gain. It originates from

the spatial size of the electromagnetic mode. The preferred transverse structure in quantum-well lasers is a single-mode, optical wave-guide. This electromagnetic mode has a spatial extent that is large compared to the size of the quantum well. In most cases, it is desirable to have the quantum well in the center of the optical mode. Consequently, considering the intensity of the electromagnetic mode to be constant over the region where the contributing eigenfunctions of the carriers are significantly large is a very good approximation Therefore, the modal gain does *not* depend on the width of the quantum well as long as its width is small compared to the width of the optical mode. A quantized state in a narrow quantum well has a high local gain over a small transverse region. In a wider quantum well, which has a lower local gain over a wider transverse region, the effective modal gain per quantized state is unchanged. Consequently, within this approximation, only the two-dimensional density is significant. The value of the three-dimensional density does not enter and is therefore of no concern.

The derivation of the gain is based on relating the density of subband transitions of quantum-well structures to the photon density. Thus the gain spectrum is derived independent of the line shape function of the transition. This approximation is valid because the effective density of states is slowly varying with respect to the uncertainty energy associated with the interband transition rate (see *Section 6.4*). Furthermore, the carrier density is related to the current density required to maintain it via the spontaneous transitions. When the simplifying assumption of isotropic material is made, both relations can be derived directly for the Einstein relations.

The basic two-level system was treated by Einstein [25]. The dependence on the index of refraction, n, has been added. Using coefficients for the spontaneous

(A) and stimulated (B) transition rates and relating them to the fundamental dipole matrix element of the transition, the following equations are obtained:

$$\frac{A}{B} = \frac{2 \cdot n^3 \cdot E_{trans}^3}{\pi \cdot \hbar^2 \cdot c^3} \tag{6.9}$$

$$A = \frac{1}{T_{spon}} = \frac{n \cdot |\mu|^2 \cdot E_{trans}^3}{\pi \cdot \varepsilon_0 \cdot \hbar^4 \cdot c^3} \tag{6.10}$$

and consequently,

$$B = \frac{|\mu|^2}{2 \cdot \varepsilon_0 \cdot n^2 \cdot \hbar^2} \tag{6.11}$$

where the square of the absolute of the dipole matrix element is

$$|\mu|^2 = |< \psi_1 |e \cdot r| \psi_2 >|^2 \tag{6.12}$$

which is a constant in isotropic material and applies to the spontaneous as well as to the stimulated transitions. An equivalent quantity, the oscillator strength, is occasionally quoted:

$$f = \frac{2 \cdot |\mu|^2}{e^2 \cdot m \cdot E_{trans}} \tag{6.13}$$

In the following, the modal gain of quantum-well lasers is derived directly from the Einstein coefficient by relating the energy *density* of the transitions to the photon density. In this approach, the inverse dependence on the width of the optical mode emerges naturally, and it is evident that introducing a confinement factor is not necessary. The stimulated rate is given by the B coefficient times the photon density in photon frequency and volume.

$$\rho = \frac{d^4 E_{photon\ field}}{d\nu \cdot d^3 V} = \frac{2\pi \cdot \hbar \cdot E_{trans}}{W_{op}} \cdot \frac{d^3 \#_{photon}}{dE \cdot d^2 A} \tag{6.14}$$

On the other hand, the density of states is a density in energy and area. A factor $\frac{2\pi \cdot \hbar \cdot E_{trans}}{W_{op}}$ provides the scaling to the number of photons, $\#_{photon}$, per energy and area, where W_{op} is the characteristic width of the electromagnetic mode.

The definition of the gain coefficient is the *relative* increase in a variable intensity, upon propagation. This definition can be rewritten and a photon density per energy and area introduced in the rightmost factor in *Equation (6.14)*, here called P_n for short, can be substituted.

$$g = \frac{1}{I} \cdot \frac{dI}{dz} = \frac{n}{c \cdot I} \cdot \frac{dI}{dt} = \frac{n}{c \cdot P_n} \cdot \frac{dP_n}{dt} = \frac{n}{c \cdot \tau_{stim}} \cdot \frac{S_n}{P_n} \qquad (6.15)$$

The rate of increase of the photon density can be re-expressed as the product of a density of transitions (a density per energy and area) S_n, and the transition rate $1/\tau_{stim}$, leading to the last expression in *Equation (6.15)*.

By using $1/\tau_{stim} = \rho \cdot B$ and *(6.11)* and substituting S_n via *Equation (6.6)* and P_n via *Equation (6.14)* in *Equation (6.15)*, the following formula emerges:

$$g = \frac{m_e \cdot |\mu|^2 \cdot E_{trans} \cdot M_{eff}}{n \cdot \varepsilon_0 \cdot \hbar^3 \cdot c \cdot W} \qquad (6.16)$$

In *Equation (6.16)*, the gain of the *mode* is given. As outlined, this two-level model is applied to all pairs of electron and hole states. For each considered transition energy all contributions to the gain are gathered. Rather than introduce integrals over the electron and hole energy individually and delta functions to pick the values consistent with the rigorous k-selection rule, constraints on the energies are specified, and no dummy integration is mentioned. Here the broadening, as introduced for the effective density of states, appears as well as the transverse overlap factor and the inversion factor. The set of quasi-Fermi energies for electrons and holes, E_{Fermie} and E_{Fermih}, is considered to obey the charge neutrality condition so that there is only one free parameter for the gain spectrum of a given transverse structure, the strength of the pumping:

$$Gain(E) = \frac{E \cdot C'}{W_{op}(E) \cdot n(E)} \sum_{i=1}^{N_e} \sum_{j=1}^{N_h} \frac{\mu^2 \cdot Overl}{1 + e^{\frac{E(i) - E_e}{\Delta E}}} \cdot \frac{Inv \cdot M_{red}}{1 + e^{\frac{E(j) - E_h}{\Delta E}}} \qquad (6.17)$$

where $W_{op}(E)$ is the effective width of the optical mode at the photon energy E. The overlap factor and the inversion factor are, respectively:

$$Overl = \left| \int_{-\frac{D}{2}}^{+\frac{D}{2}} \psi(i)^* \cdot \psi(j) dx \right|^2 \tag{6.18}$$

$$Inv = \frac{1}{1 + e^{\frac{E_e - E_{Fermi}}{kT}}} + \frac{1}{1 + e^{\frac{E_h - E_{Fermih}}{kT}}} - 1 \tag{6.19}$$

And the relative reduced effective mass is

$$M_{red} = \frac{1}{\frac{1}{M(i)} + \frac{1}{M(j)}} \tag{6.20}$$

There is a very special relation between E_e, E_h, and E implied, which depends on i and j. First, the excess energy over the bandgap energy is the sum of the energy in the conduction band and the energy in the valence band:

$$E_{ex} = E - E_g = E_e + E_h \tag{6.21}$$

Second, the excess energy over the bandgap energy is split in such a way that the rigorous k-selection rule for the electron eigenstate i, and the hole eigenstate j applies:

$$E_e = \frac{E_{ex} - E(i) - E(j)}{M(i) \cdot \left(\frac{1}{M(i)} + \frac{1}{M(j)} \right)} + E(i) \tag{6.22}$$

$$E_h = \frac{E_{ex} - E(i) - E(j)}{M(j) \cdot \left(\frac{1}{M(i)} + \frac{1}{M(j)} \right)} + E(j) \tag{6.23}$$

Finally, C' includes the basic constants, the rest mass of the electron m_e, the vacuum permittivity ε_0, $\hbar$ Planck's constant divided by 2π, the speed of light in vacuum c and in the matrix element μ. The matrix element is based on the value $\mu_0 = 5.2 \cdot 10^{-29} \ msA$ as given in Reference [26], but is scaled according to Reference [27] as follows:

$$\mu^2 = \mu_0^2 \cdot \left(\frac{1.424 \ eV}{E_{Trans}} \right)^2 \cdot \frac{\frac{1}{M(i)} - 1}{\frac{1}{M_0} - 1} \tag{6.24}$$

where 1.424 eV and $M_0 = 0.0667$ are the reference values of the transition energy and effective, relative electron mass. The constant is

$$C' = \frac{m_e}{\varepsilon_0 \cdot \hbar^3 \cdot c} \qquad (6.25)$$

so that $C' \cdot \mu_0^2 = 7.913 \cdot 10^{17} \ J^{-1} = 0.127 \ eV^{-1}$. This model involves a considerable amount of computation, which can be reduced about eightfold by considering symmetrical structures exclusively. In many applications the maximum of the gain is the only important part of the gain spectrum, but this value is wanted as a function of carrier density or quasi-Fermi energy. In these cases the spectral range to be evaluated can be reduced considerably; however, great care must be taken to ensure that the absolute maximum of the gain is found in cases of high excitation (see second quantized-state lasing of a single-quantum-well laser, *Chapter 4*).

While the gain spectrum is the response to probing the system with light, that is, the stimulated emission, the consideration of the spontaneous emission gives the radiating component to the current density required to maintain the gain at steady state. The radiating component seems to be the dominant contribution to the threshold current of high-quality material semiconductor lasers if the leakage current is low.

The calculation is based on the two-level system: A definite electron in the conduction band and a definite hole in the valence band with an equal in-plane k-vector have a spontaneous lifetime of

$$\tau_{spont} = \frac{\pi \cdot \varepsilon_0 \cdot \hbar^4 \cdot c^3}{\mu^2 \cdot n} \cdot \frac{1}{E_{trans}^3} \qquad (6.26)$$

For $E_{trans} = 1.424 \ eV$ and $n = 3.4$, this computes to $\tau_{spont} = 0.85 \ ns$; the actual value is reduced by dividing through the occupation factors. The total rate of

transitions per area multiplied by the charge of the electron is the current density. The current density is calculated by integrating the inverse spontaneous lifetime multiplied by the density of transitions (per area and energy) over the transition energies, E_{trans}. The density of the transitions is determined by the density of possible transitions, as given from the density of states, multiplied by the probability of having the electron and hole state individually occupied and the weighting factor for these states, as introduced for the density of effective states:

$$j = C'' \sum_{i=1}^{N_e} \sum_{j=1}^{N_h} \int_{-\infty}^{+\infty} \frac{\mu^2 \cdot E^3 \cdot n}{1 + e^{\frac{E(i) - E_e}{\Delta E}}} \cdot \frac{Overl \cdot M_{red} \cdot Occu}{1 + e^{\frac{E(j) - E_h}{\Delta E}}} dE \qquad (6.27)$$

where the occupation factor for the transition is

$$Occu = \frac{1}{1 + e^{\frac{E_e - E_{Fermie}}{kT}}} \cdot \frac{1}{1 + e^{\frac{E_h - E_{Fermih}}{kT}}} \qquad (6.28)$$

Again, C'' includes the basic constants and the matrix element and is

$$C'' = \frac{e \cdot m_e}{\pi^2 \cdot \varepsilon_0 \cdot \hbar^6 \cdot c^3} \qquad (6.29)$$

so that $\mu_0^2 \cdot C'' = 1.219 \cdot 10^{83} \frac{A}{m^2 J^4} = 8.03 \cdot 10^3 \frac{A}{cm^2 eV^4}$. The integrand in *Equation 6.27* scales with the photon energy-dependent index of refraction n as well as with the reduced effective mass *(6.20)*. *Equations (6.21)* to *(6.23)* are used to specify E_l and E_h.

6.7 Conclusion

A model to compute gain spectra for quantum-well lasers is presented. In contrast to previous models, the derivation is specifically for quantum-well lasers and is based directly on the Einstein coefficients. The conventionally used Lorentzian-broadening of the transition is analyzed and found not to be theoretically justified. A heuristic smearing of the density of states is introduced to define the effective

density of states, which is then used as the base of the intraband transitions. The used density of states is the density in area, not volume, because the distribution in the transverse direction is found to be irrelevant to the gain spectrum. The model provides a natural transition to wider structures; therefore, it can be used directly to calculate double heterostructures.

6.8 Appendix: Phase-Density Method

The eigenvalue problems *Equations 6.1, 6.2,* and *6.3* can be solved by one generalized method. A single eigenvalue equation for a generalized function $w(z)$ is solved:

$$\frac{-d}{dz}\frac{1}{f_1(z)}\frac{d}{dz}f_2(z)w(z) + P(z) \cdot w(z) = E \cdot w(z) \qquad (6.28)$$

For the Schrödinger equation, P is the potential, E is the eigenenergy, $f_2 = 1$ and $f_1 = \frac{1}{M(z)}$, and $z = \frac{\sqrt{2}}{\hbar} \cdot x$, where x is the transverse spatial coordinate.

For the TE-mode, *Equation (6.2)*, $-P$ is defined to be $\varepsilon(x)$ (permittivity), and the values of $-E$ are the eigenpermittivity determining the propagation constant, $f_1 = 1$, $f_2 = 1$, and $z = k_0 \cdot x$. For the TM-mode, *Equation (6.3)*, $f_1 = \varepsilon(x)$ and $f_2 = \varepsilon(x)$; otherwise, it is similar to the TE-mode. The minus signs are introduced to compensate for the minus sign in *Equation (6.28)*.

In this thesis, the material properties $f_1(x)$, $f_2(x)$, and $P(x)$ will be considered piecewise constant as a result of the steplike Al-concentration in the transverse profile. In practice, the Al-concentration can be made to change gradually as well as abruptly. This approach is chosen so that the solutions to the differential equations are simple; they are either sinusoidal, linear, or exponential. As a result, the eigenfunctions can be described as simple piecewise, analytical functions, and calculation of high precision can be achieved for a small number of subintervals for the region of interest.

The eigensolution of the generalized equation in a region where $E > P(x)$ can be presented as follows:

$$w(z) = w_0(z_0) \cdot Envelope(z) \cdot sin(\int_{z_0}^{z} \kappa(z')dz' + \beta) \qquad (6.29)$$

For the case $w_0(0) \neq 0$, the terms $w_0(z_0) \cdot sin(\beta)$ and β are the amplitude and phase at the reference position z_0, respectively, and $Envelope(z)$ is the envelope function of the solution normalized to $\frac{1}{sin(\beta)}$ at position z_0. The function $\kappa(z)$ is defined as

$$\kappa(z) = \sqrt{\frac{f_1(z)}{f_2(z)}} \cdot \sqrt{E - P(z)} \cdot H(E - P(z)) + \Delta(z) \qquad (6.30)$$

The delta function contributions $\Delta(z)$ originate from stepwise changes and the second spatial derivative in the differential equation. The local behavior given in *Equation 6.30* expresses the *excess of the eigenvalue over the potential*, and $f_1(z)$ and $f_2(z)$ determine the value of the phase density, that is, the rate at which the phase progresses with a change of position as long as $E > P(z)$. At any z_d where $P(z)$ is discontinuous and $P(z) < E$ on both sides of the discontinuity, the $\Delta(z)$ is nonvanishing and is:

$$\Delta(z) = \left[arctan\left(\sqrt{\frac{E - P^-}{E - P^+}} \cdot \frac{f_1^+}{f_1^-} \cdot tan(\alpha^-)\right) - \alpha^- \right] \cdot \delta(z - z_d) \qquad (6.31)$$

where $\alpha^- = \int_{z_d}^{z} \kappa(z')dz' + \beta$, and P^- $\{P^+\}$ is the potential at the left- $\{$ right- $\}$ hand side of z_d, and f_1^- $\{f_1^+\}$ is the value of f_1 at the left- $\{$ right- $\}$ hand side of z_d.

The quantity $k(x)$ associated with $\kappa(z)$ is normally named *wave number*. The wave number is defined as the "spectroscopic wave number" times $2\pi \cdot n(x)$, where $n(x)$ is the index of refraction [27]. The spectroscopic wave number is the number of waves, that is, the full periods, per unit length in vacuum. But this term will not be used because this name is often associated with a global character as well as restricted to electromagnetic phenomena. Instead, the term *phase density* will be used exclusively because it helps to emphasize a local and may be a variable quantity.

The integral in *Equation 6.29* (the argument of the sinus function apart from β) is the accumulated phase called $\phi(z_0, z)$ at z with respect to z_0. It is helpful to consider z_0 and z to be the left and right boundaries of the region where the potential is continually smaller than the eigenenergy. Under the additional assumption that there is only one such region, the phase, that is, the integrated phase density, determines the *index* or *quantum number, n,* uniquely describing the eigenfunction via

$$(n - 1) \cdot \pi < \phi(z_0, z) \le n \cdot \pi \tag{6.32}$$

The assumption that there is only one region with continually lower *potential* than the eigenvalue is restrictive. For instance, a multiple-quantum well, in general, cannot be treated. Therefore, the concept of phase density has to be extended to bridge *barriers*. The application is to determine the phase of a given solution, in particular, the contribution that the region of a barrier makes. For a barrier from z_1 to z_2, the contribution to the phase is computed as follows: If α^- is the phase at the left-hand side of the barrier (z_1^-) as defined above and α^+ is the phase at the right-hand side of the barrier (z_2^+), the phase density may be defined simply as:

$$\Delta(z_2) = (\alpha^+ - \alpha^-) \cdot \delta(z - z_2) \tag{6.33}$$

where α^+ is found by propagating the eigenfunction through the barrier with its local exponential rising and falling solution, and matching at the boundary to the oscillatory solution on the right-hand side of the barrier.

The value of the integrated phase addressed to the barrier according to *Equation 6.33* is in the range $-\pi$ to $+\pi$. A zero crossing, similar to the situation in the oscillatory solutions, is an indication of advancing the phase.

The zero crossing comes about by having absolute equally large (but with opposite sign) contributions of the exponentially increasing and the exponentially decreasing function at one location in the barrier. Therefore, it is the exponentially increasing contribution that is decisive about the zero crossing, making it very sensitive on the particular boundary conditions. This sensitivity is the reason that the dispersion relation can have such radical changes in the case that a barrier is present, a condition that can make conventional root-finding programs to fail.

The phase-density method is general, but only the version for symmetric structures will be used in this thesis. The region of interest starts with the outside of the cladding layer and continues till the center of the structure is reached. Assigning a zero phase to the outside of the cladding layer results in an integrated phase of $n \cdot \pi/2$ at the symmetry plane for the eigensolutions, where n is the *index* or *quantum number*.

Therefore, this phase-density method ensures the finding of each particular eigenfunction and its associated eigenvalue. An additional advantage of the phase-density method is its capability to provide the number of confined states by using the highest trial eigenvalue presenting a possible confined state and finding the integrated phase revealing the number of confined states via *Equation (6.32)* as $n - 1$.

6.9 References

[1]. van der Ziel J.P., R. Dinge, R.C. Miller, W. Wiegmann, and W.A. Nordland, Jr.: *"Laser oscillation from quantum states in very thin $GaAs - Al_{0.2}Ga_{0.8}As$ multilayer structures."* Appl. Phys. Lett. **26**(8):463-465 (1975).

[2]. Dingle R., and C.H. Henry: *"Quantum effects in heterostructure lasers."* U.S.Patent 3,982,207.

[3]. Chang L.L., L. Esaki, and R. Tsu: *"Resonant tunneling in semiconductor double barriers."* Appl. Phys. Lett. **24**(12):593-595 (1974).

[4]. Dingle R., W. Wiegmann, and C.H. Henry: *"Quantum states of confined carriers in very thin $Al_xGa_{1-x}As$-$GaAs$-$Al_xGa_{1-x}As$ Heterostructures."* Phys. Rev. Lett. **33**(14):827-830 (1974).

[5]. Cho A.Y.: *"Film Deposition by Molecular-Beam Techniques."* J. Vac. Sci. Technol. **8**(5):S31-S38 (1971).

[6]. Arthur J.R., Jr.: *"Interaction of Ga and As_2 molecular beams with GaAs surfaces."* J. Appl. Phys. Lett. **39**:4032-4035 (1968).

[7]. Manasevit H.M.: *"The use of metalorganics in the preparation of semiconductor materials II. Epitaxial III-V aluminum compounds using trimethylaluminum."* J. Electrochem. Soc. **116**:250C (1969).

[8]. Dupuis R.D., and P.D. Dapkus: *"Preparation and properties of $Ga_{1-x}Al_xAs - GaAs$ heterostructure lasers grown by metalorganic chemical vapor deposition."* IEEE J. Quantum Elect. QE-15(3):128-135 (1979).

[9]. Asada M., A. Kameyama, and Y. Suematsu: *"Gain and intervalence band absorption in quantum-well lasers."* IEEE J. Quantum Elect., QE-20(7):745-753 (1984).

[10]. Arakawa Y., and A. Yariv: *"Theory of gain, modulation response, and spectral linewidth in AlGaAs quantum-well lasers."* IEEE J. of Quantum Elect., QE-21(10):1666-1674 (1985).

[11]. Asada M., and Y. Suematsu: *"Density-matrix theory of semiconductor lasers with relaxation broadening model-gain and gain-suppression in semiconductor lasers."* IEEE J. of Quantum. Elect., QE-21:434-442 (1985).

[12]. McIlory P.W.A., A. Kurobe, and Y. Uematsu: *"Analysis and application of theoretical gain curves to the designs of multiquantum-well lasers."* IEEE J. Quantum Elect. QE-21(12):1958-1963 (1985).

[13]. Sugimura A. *"Threshold currents for AlGaAs quantum-well lasers."* IEEE J. Quantum Elect. QE-20(4):336-343 (1984).

[14]. Dutta N.K.: *"Calculated threshold current of GaAs quantum-well lasers."* J. Appl. Phys. 53(11):7211-7214 (1982).

[15]. Chinn S.P., P.S. Zory, and A.R. Reisinger: *"A model for GRIN-SCH-SQW diode lasers."* IEEE QE-24:2191-2214 (1988).

[16]. Bastard G., and J. A. Brum: *"Electronic States in Semiconductor Heterostructures."* IEEE J. Quantum Elect. QE-22(9):1625-1644 (1986).

[17]. Colak S., E.R. Eppenga, and M.F.H. Schuurmans: *"Band mixing effects on quantum well gain."* IEEE J. Quantum Elect. QE-23(6):960-968 (1987).

[18]. Marsh A.C., and J.C. Inkson: *"The electronic properties of GaAs/AlGaAs heterojunctions."* IEEE J. Quantum Elect. **QE-22**(1):58-66 (1986).

[19]. Schiff L.I.: *Quantum Mechanics.* McGraw-Hill Book Company: New York, 3rd edition (1968), p. 416.

[20]. Mittelstein M., Y. Arakawa, A. Larsson, and A. Yariv: *"Second Quantized State Lasing of a Current Pumped Single Quantum Well Laser."* XIV Int. Quantum Elect. Conference, Pd-16 (1986), and Appl. Phys. Lett. **49**(25): 1689-1691 (1986).

[21]. Yamanishi M., and Y. Lee: *"Phase dampings of optical dipole moments and gain spectra in semiconductor lasers."* IEEE J. Quantum Elect. **QE-23**(4):367-370 (1987).

[22]. Tarucha S., H. Kobayashi, Y. Horikoshi, and H. Okamoto: *"Carrier-induced energy-gap shrinkage in current-injection GaAs/AlGaAs MQW heterostructures."* Japanese J. of Appl. Phys. **23**(7):874-878 (1984).

[23]. Blood P., E.D. Fletcher, P.J. Hulyer, and P.M. Smowton: *"Emission wavelength of AlGaAs-GaAs multiple quantum-well lasers."* Appl. Phys. Lett. **48**(17):1111-1113 (1986).

[24]. Tomita A., and A. Suzuki: *"Carrier induced lasing wavelength shift for quantum-well laser diodes."* IEEE J. Quantum Elect. **QE-23**:1155-1159 (1987).

[25]. Einstein A.: *"Zur Quantentheorie der Strahlung."* Physik. Zeitschr. XVIII:121 (1917).

[26]. Yariv A.: *Quantum Electronics*. John Wiley and Sons: New York, 3rd. edition (1989), p. 273.

[27]. Yamada M., O. Shouichi, M. Yamagishi and K. Tabata: *"Anisotropy and broadening of optical gain in a GaAs/AlGaAs multiquantum-well laser."* IEEE J. Quantum Elect. **QE-21**(6):640-645 (1985).

[28]. Born M. and E. Wolf: *Principals of Optics*. Pergamon Press: New York, 6th. edition (1988), p. 16.

Chapter Seven

7: Gain Calculations of Semiconductor Lasers

Abstract

In this chapter, a calculation of the performance characteristics of the popular parabolic-graded index single-quantum-well laser is presented as calculated from the model introduced in *Chapter 6*. A comparison of structures that tightly confine the charge carriers in 0, 1, 2, and 3 dimensional is performed. This comparison is based on the calculated performance of specific laser structures for a commonly given gain requirement. A figure of merit for quantum-size effects is introduced and discussed. Conventional, double-heterostructure and multiple-quantum-well structures are contrasted to single-quantum-well lasers. Optimization aspects of the lateral structure are presented and applied to a high-power laser structure. The specific requirement for carrier confinement and optical mode guidance is related by using the previously introduced phase-density method (*Section 6.8*). The high degree of optimization of the single-quantum-well laser structure is derived.

7.1 Introduction

The model of quantum-well structures used in this thesis, including the details of the gain spectra, have been described in *Chapter 6*. In this chapter, on the one hand, applications of the model are presented as specific examples; on the other hand, some general concepts are introduced, which make it possible to obtain performance criteria without detailed calculations.

Some typical details of overall laser structures are described, and the results of applications of this model are presented in *Section 7.2*. Generalized conclusions of confining structures are presented. The base for comparing single-quantum-well laser properties to conventional, double-heterostructure lasers and a comparison to wire and dot structures are given in *Section 7.3*. A figure of merit for the onset of quantum-size effects is introduced and applied to single-quantum-well structures in *Section 7.4*. Following a brief examination of the properties of conventional, double-heterostructure lasers in *Section 7.5*, the multiple-quantum-well structure is introduced in *Section 7.6*. Aspects of optimization of the lateral structure are given together with a proposed transverse structure for high-power lasers in *Section 7.7*. And finally in *Section 7.8*, the concept of separate confinement is addressed via the requirement of the size of the structure to confine the charge carriers and the size of the structure to guide the optical mode. The chapter is summed up in *Section 7.9* with general conclusions about quantum-well lasers.

Modern quantum-well lasers use a graded-index, separate-confinement heterostructure (GRIN SCH). In this structure, the benefits of the double heterostructure for the confinement of the carriers and the electromagnetic mode are implemented separately. The carriers are confined by the quantum well, while the optical confinement is achieved with a graded Al-concentration and therefore an index structure surrounding the quantum well. It should be noted that the structure used to confine the optical mode needs to be up to two orders of magnitude wider than the quantum well as will be described in *Section 7.8*. A popular choice for this structure is a parabolic-graded region perturbed by the narrow, central quantum well and terminated in a continuous transition to the cladding layers as shown in *Figure 6.1a*. The popularity arises from the continuous record-breaking, low-threshold current densities of these structures. The only approximate treatment
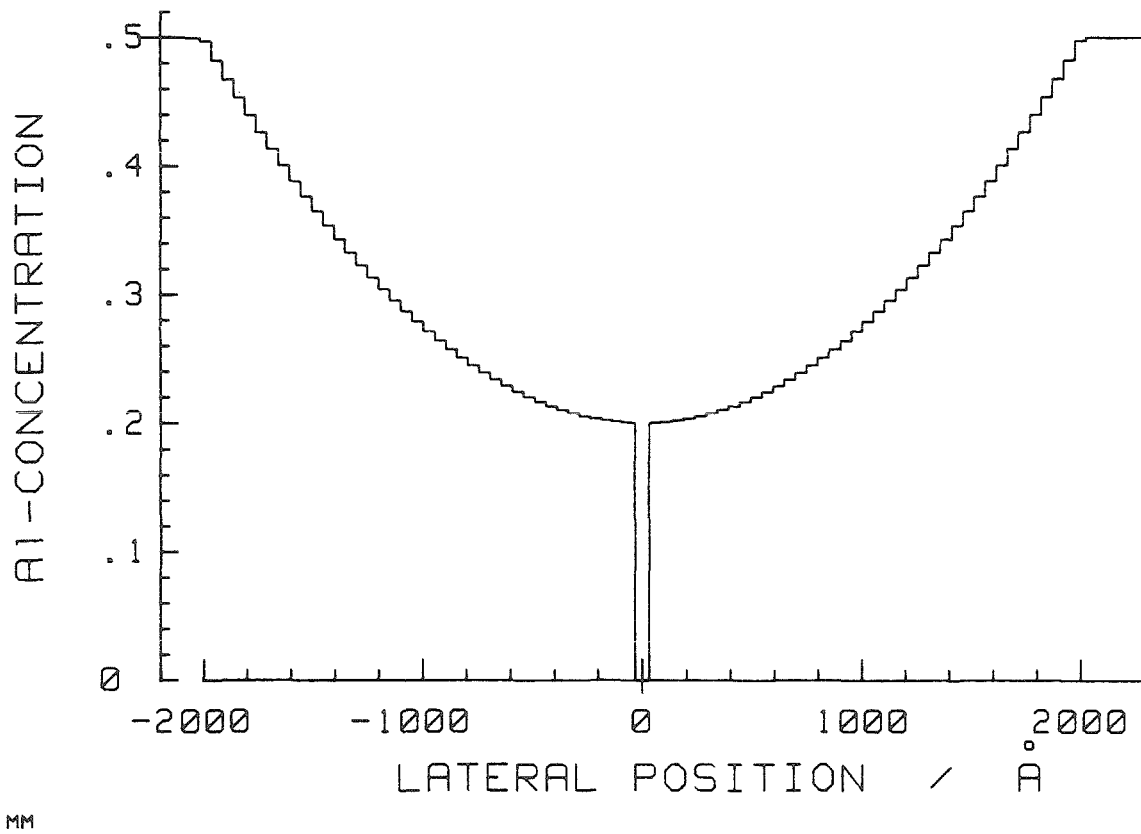
Figure 7.1 The inner structure of the parabolic-graded index, single-quantum-well laser as used for the numerical calculations. The cladding layers are not shown.

(considering the optical mode as a fundamental Gaussian) indicates that a thorough optimization of this structure has not yet been undertaken. An optimization of a single-quantum-well laser structure will be given in *Chapter 7.7*.

7.2 Numerical Results of the Gain Spectrum Model

The specific structure to be used for numerical results of the gain spectrum is the symmetric structure similar to the one introduced in *Chapter 4 (Figure 7.1)*. The transverse Al-concentration profile has a single-quantum well of 100 $\mathring{A}$ width at the center of a parabolic wave-guide of 4000 $\mathring{A}$ total width, which continues without a step in the two 13000 $\mathring{A}$ thick cladding layers of 0.5 Al-concentration. The minimum Al-concentration of the parabola is 0.2, with a discontinuous transition to the GaAs quantum well. One-half of the structure is represented in the numerical model by a total of 47 slices of variable width of piecewise-constant Al-concentration.

In order to find the effective width of the electromagnetic mode as introduced in *Chapter 6.4*, the permittivity profile for the transverse structure is determined, and the Helmholtz equation is solved via the phase-density method of *Sections 6.2* and *6.8*. The eigenvalue of the Helmholtz equation is the effective, relative permittivity, $\varepsilon_{ri}(E_{ph})$, which gives the propagation constant β, via $\beta = \frac{E_{ph}}{c \cdot \hbar} \cdot \sqrt{\varepsilon_{ri}(E_{ph})}$. The eigenfunction of the Helmholtz equation determines the effective width of the optical mode, which is inversely proportional to the modal gain. The prerequisite for solving for the eigenvalue of the permittivity of the transverse structure is to find the permittivity of the individual slices. The permittivity changes not only with the Al-concentration but with the photon energy in a nonlinear fashion.

The method employed to find the permittivity of the material is based on the spectral index of refraction of GaAs and several Al-concentrations of GaAlAs [1] as

Figure 7.2 Spectral index of refraction of GaAs and several Al-concentrations of GaAlAs [1] as well as of AlAs [2].

Figure 7.3 Eigensolutions at 1.4 eV, 1.5 eV, and 1.6 eV photon energy as well as the table of the effective widths of the fundamental modes for the structures of these photon energies. The eigenvalues of the relative permittivity and their equivalent bulk Al-concentrations, X, are presented.

well as of AlAs [2]. The doping dependence is not taken into account. The values at 1.4, 1.5, and 1.6 eV are taken from the published curves [1, 2], and a quadratic spectral behavior is fitted. Then a linear fit is performed for intermediate Al-concentrations. *Figure 7.2* shows the used values in the spectral region of interest. For the three determined permittivity profiles associated with the three photon energies, the Helmholtz equation is solved and the eigenvalues and eigenfunctions are found (in the sense that at the outer side of the cladding layer, the function is not matched but rather minimized, as in the previous sections).

For the eigenfunctions of the Helmholtz equation, the effective width of the electromagnetic mode is calculated according to the definition:

$$W_{em} = \frac{\int_{-d/2}^{+d/2} I(x)dx}{I_{QW}} \tag{7.1}$$

where $I(x)$ is the transverse intensity profile of the eigensolution, I_{QW} is the intensity at the location of the quantum well, and d is the total width of the transverse structure including the cladding layers. Using the effective width values at three different photon energies provides a quadratic expression for the frequency dependence of the effective width of the lasing mode. *Figure 7.3* shows the eigensolution at 1.4 eV, 1.5 eV, and 1.6 eV photon energy as well as the table of the effective width of the fundamental mode for the structure at these photon energies. The change in the eigenvalue of the index with photon energy is the reason that the longitudinal mode spacing is actually about one-quarter larger than the prediction based on a fixed index of refraction, commonly referred to as dispersion. The change in the effective width of the eigenfunctions with photon energy has not been addressed previously.

For single transverse-mode operation, it is advantageous if the wave-guide structures meet the following criteria: A second eigensolution does not exist, or the

WAVELENGTH / nm
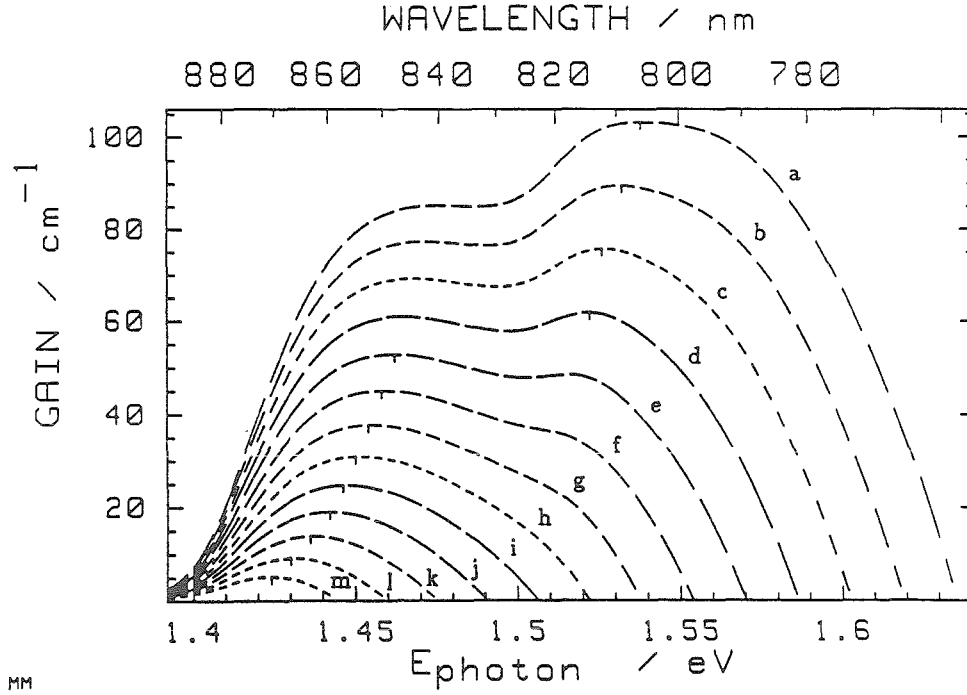
Curve	E_{Fe} eV	E_{Fh} eV	G_{max} $\frac{1}{cm}$	λ nm	N_{occ} $\frac{10^{12}}{cm^2}$	j $\frac{A}{cm^2}$	η ns
a	0.22	0.0395	103.2	806.1	32.3	1333	3.88
b	0.21	0.0333	89.5	809.3	26.8	1126	3.81
c	0.20	0.0270	75.7	812.5	22.0	936	3.76
d	0.19	0.0207	61.8	814.6	18.0	767	3.76
e	0.18	0.0143	52.8	848.0	14.7	619	3.79
f	0.17	0.0081	45.1	850.3	11.9	494	3.87
g	0.16	0.0019	37.8	852.7	9.7	389	4.00
h	0.15	-0.0004	31.0	855.0	7.9	304	4.18
i	0.14	-0.0097	24.7	857.4	6.5	236	4.42
j	0.13	-0.0153	19.0	859.8	5.4	181	4.73
k	0.12	-0.0207	13.8	863.4	4.4	138	5.12
l	0.11	-0.0261	9.1	867.0	3.7	104	5.62
m	0.10	-0.0313	5.2	870.6	3.0	77	6.24

Figure 7.4 Gain spectra of a single-quantum-well laser for different pumping strengths. The table gives parameters for the shown traces. Note the transition of the gain maximum from lower to higher photon energies with increasing pumping. The second quantized-state lasing occurs when the spectrally independent gain exceeds 60 $\frac{1}{cm}$.

existing second eigensolution exhibits an intensity at the outside of the cladding layer nearly as large as the peak intensity. This criterion ensures that the second eigensolution is either not guided or is very leaky guided and cannot be populated with photons by stimulated emission; therefore, it does not compete with the fundamental eigenmode for the inversion of the laser.

The Schrödinger equation is solved (using the phase-density method of *Sections 6.2* and *6.3*) to find the electron and hole eigenstates and eigenenergies of the transverse structure. The increase of the bandgap is taken as linear in the Al-concentration, a fixed fraction, 0.67, which is considered for the conduction band and therefore effective for the electrons. The remaining fraction taken up by the valence band, 0.33, is effective for the holes. In this thesis, the conduction-band profile is $E = 0.67 \cdot 1.247eV \cdot X$, and the valence-band profile is $E = 0.33 \cdot 1.247eV \cdot X$, where X is the Al-concentration. Similarly, the relative effective masses are approximated to scale linearly with the Al-concentration: $M_e = 0.0667 + 0.0833 \cdot X$, $M_{lh} = 0.087 + 0.1209 \cdot X$, and $M_{hh} = 0.380 + 0.0985 \cdot X$ are used.

By occupying the effective density of states for the electrons and holes such that their sheet charge density is compensated, the relation of the quasi-Fermi energies for the valence and conduction band is found as shown in *Figure 6.6*. For the gain calculation of the parabolic GRIN SCH structure, a carrier-density-independent bandgap renormalization of -48 *meV* is applied. When the gain is computed using the scaled matrix element of (6.29) [3, 4], the gain spectrum at various carrier densities results, as shown in *Figure 7.4*. It is evident that the gain maximum appears at significantly higher photon energies, once the carrier density gets high enough to have the second quantized state sufficiently occupied. Some of the parameters for the gain spectra (a) to (m) of *Figure 7.4* are presented in

the associated table. This structure can provide enough gain for a 430 μm long cavity with simple cleaved facets to lase with threshold-current density just below 300 $\frac{A}{cm^2}$ at a carrier lifetime of 4.2 ns, according to the model presented in this thesis. The predicted jump in the lasing wavelength of 33 μm (assuming that the model is precise) indicates that the single-quantum-well structure used for the experiments as described in *Chapters 4* and *5* probably had a thinner quantum well, thus explaining its lower threshold-current density in comparison to the one in this prediction.

7.3 Comparison of Quantum-Confined Structures

In this section, bulk material is compared to structures that exhibit reduced dimensionality introduced by quantum confinement. The objective is to consider the fundamental effects of tight confinement on the density of states first. In particular, the density of occupied states needed for transparency is calculated. Secondly, 0-, 1-, 2-, and 3-dimensional confinement structures are considered as gain medium in a GaAs semiconductor laser. A fixed transverse mode width and resonator loss are assumed, providing a comparison of internal quantities independent of the overall side of the laser. The results are summarized in *Tables 7.1* and 7.2. Considering first-order effects, only tight confinement in a different number of dimensions leads to a different ratio of the density of states in the valence band as compared to that of the conduction band. In all dimensions, n, the density of states scales with the $\frac{n}{2}$-power of the effective mass of the charge carriers. In the case of bulk, the 3-dimensional case, the valence band is made up of contributions of light and heavy holes, resulting in a ratio of the density of states in the valence band to the density

of states in the conduction band of

$$Ratio_3 = \left(\frac{M_{hh}}{M_{el}}\right)^{3/2} + \left(\frac{M_{lh}}{M_{el}}\right)^{3/2} = 15.1 \qquad (7.2)$$

where $M_{hh} = 0.38$, $M_{lh} = 0.087$, and $M_{el} = 0.0667$ are assumed for the effective masses of the electron, light hole and heavy hole in terms of the rest mass of the electron, respectively. In the case of a well (two-dimensional case), the onset energy of the heavy hole is lower than the onset energy of the light hole; therefore, the light hole constitutes only a second-order effect for a strong enough confinement, and, consequently, the ratio becomes:

$$Ratio_2 = \frac{M_{hh}}{M_{el}} = 5.7 \qquad (7.3)$$

Similarly, the ratio for quantum wires becomes

$$Ratio_1 = \sqrt{\frac{M_{hh}}{Mel}} = 2.4 \qquad (7.4)$$

For quantum boxes, because of their atomiclike properties and again an increasing difference in confinement energy between the light and heavy hole, the ratio simply becomes:

$$Ratio_0 = 1 \qquad (7.5)$$

The shape of the different density-of-state functions of the bulk and subbands of the confined states in lower dimensions is commonly considered, but the properties implied by this ratio are not emphasized. For the case of transparency at the transition at the onset of the bands, an electron population considerably exceeding 0.50 has to be established in all cases but the quantum box.

The density of carriers for transparency at the onset energy of the subbands is one of the key parameters of the laser medium. The number is found by integration

Dimension	3	2	1	0
Name of laser	Bulk	Well	Wire	Box
Ratio	15.1	5.7	2.4	1
Subband density	$\frac{\sqrt{2}}{\pi} \frac{m^{\frac{3}{2}}}{\hbar^3} \sqrt{E}$	$\frac{1}{\pi} \frac{m}{\hbar^2}$	$\frac{\sqrt{2}}{\pi} \frac{\sqrt{m}}{\hbar} \frac{1}{\sqrt{E}}$	$2 \cdot \delta(E)$
Quasi-Fermi energy	$1.75 \cdot k_B T$	$1.22 \cdot k_B T$	$0.69 \cdot k_B T$	$0 \cdot k_B T$
Transparency density	$1.078 \cdot 10^{18}$ cm^{-3}	$1.070 \cdot 10^{12}$ cm^{-2}	$1.060 \cdot 10^{6}$ cm^{-1}	1
Asymmetry factor	3.23	2.13	1.47	1

Table 7.1 Comparison of GaAs/GaAlAs lasers with different confinement structures leading to dimensionalities from three to zero. The ratio gives the effective asymmetry of the valence band with respect to the conduction band. The subband density includes the twofold increase that is due to spin; its energy parameter, E, is with respect to their onset energy, below which the density is zero. The quasi-Fermi energy is given for the conduction band with respect to the onset energy, and the computed carrier density at room temperature $(k_B T = 0.026 \ eV)$ is given for transparency at the transition energy corresponding to the onset of the subbands. For 0.5 population of the electrons at the onset of the conduction band, the density is lower by the asymmetry factor given in the last row.

114
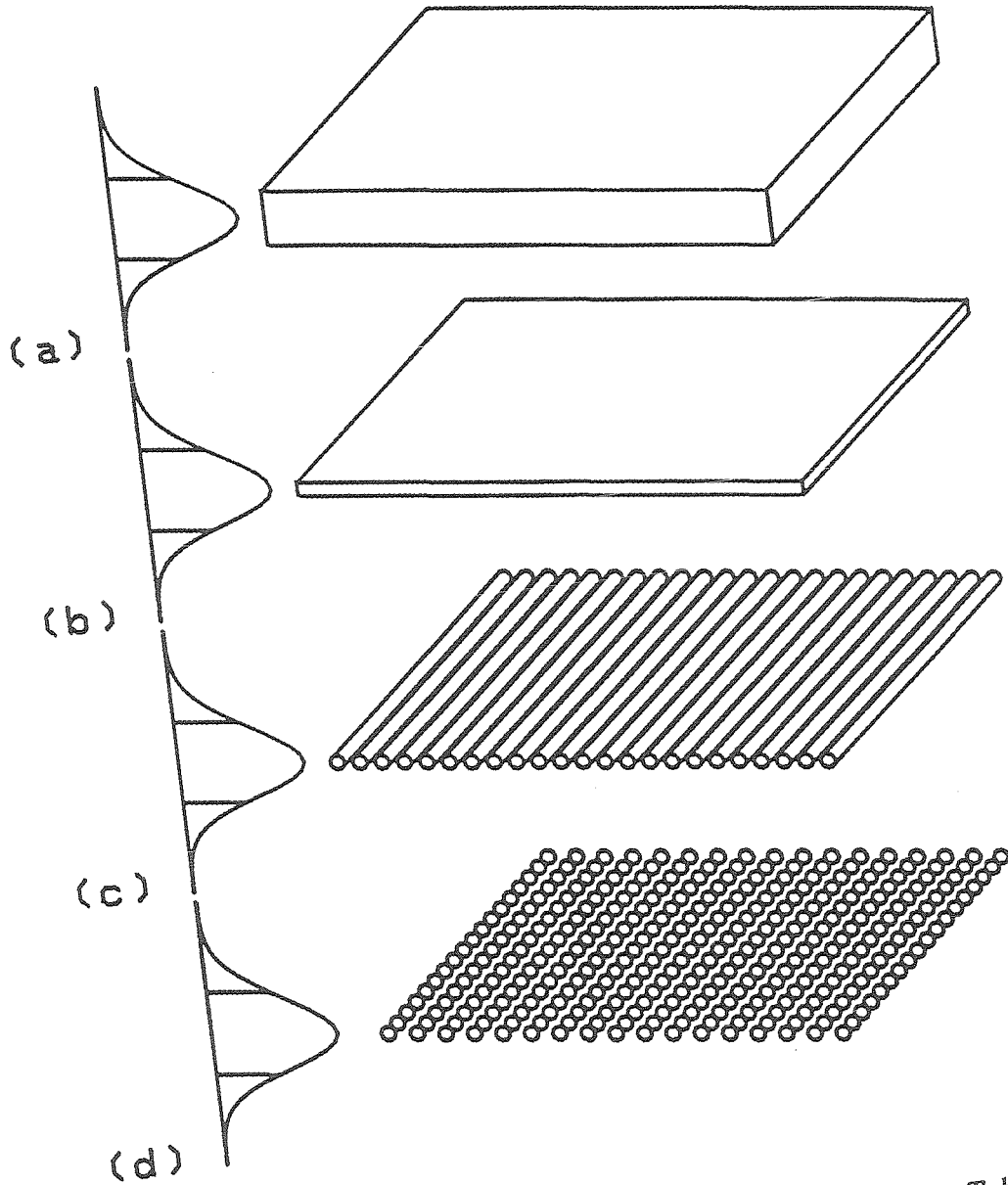
Figure 7.5 Active regions of laser structures used in the comparison in *Table 7.2.* The width of the optical mode is indicated on the left side. (a) 2000 Å thick active region of the conventional double heterostructure. (b) 100 Å thick single-quantum well. (c) one-dimensional planar array of 100 Å diameter quantum wires on 157Å centers. (d) two-dimensional planar array of 100 Å diameter quantum boxes on 200 Å square centers. The structures (b), (c), and (d) are five times larger than scale with respect to the width of the optical mode.

over energy of the density-of-states function weighted by the Fermi occupation factor and by requiring overall charge neutrality and zero inversion at the onset-energy transition. The quasi-Fermi energy for electrons with respect to the onset of the conduction band is conveniently expressed in units of the thermal energy, $k_B T$. The numbers for this energy ratio are given in *Table 7.1*. For the effective masses given above, this approximation leads to a density of carriers at room temperature $(k_B T = 0.026 \ eV)$ as given in *Table 7.1*.

Furthermore, smearing in energy with a characteristic width of ΔE has to be considered. The shape of smearing does not necessarily include the Lorentzian line shape because of its long tails. With smearing, the results are further modified and become more involved, since the photon energy at which the material becomes transparent is no longer obvious.

In the following, a comparison of laser structures using 0-, 1-, 2-, and 3-dimensional confinement based on equal modal gain is performed. The effect of different quantum confinements on parameters such as threshold-current density becomes directly comparable, by using equal transverse-optical-mode width. *Figure 7.5* gives a sketch of the four active regions of the comparison.

A very recent paper on calculations for quantum-wire lasers by Zarem et al. [5] allows scaling performance characteristics for a direct comparison with a quantum-well laser. For the active region, a one-dimensional array of parallel 100 $\mathring{A}$ diameter wires on 157 $\mathring{A}$ centers is considered. Considering 100 $\mathring{A}$ diameter wires a fabrication tolerance [5] of about 4.3 $\mathring{A}$ leads to an energy spreading of $\Delta E = 6.6 \ meV$. In this case a "bulk" gain of about 1800 $\frac{1}{cm}$ is achieved at a bulk density of $5 \cdot 10^{18}$ $\frac{1}{cm^3}$ [5]. For 30 $\frac{1}{cm}$ of gain for an optical mode of 3000 $\mathring{A}$ width, a packing density of 157 $\mathring{A}$ lateral spacing is required. Using 3 ns for the average carrier lifetime, a

current density of 133 $A\ cm^{-2}$ is estimated for this lasing condition. This calculation is realistic under the assumption that wires with high uniformity can be produced because all bandfilling effects have been taken into account. The rather close spacing of individual wires could be avoided by using n transverse layers of wires with lateral wire spacing increased n-fold. Quantum wire lasers have not as yet been demonstrated experimentally.

For the quantum-box laser, an active region in the form of a single sheet of 100 $\overset{\circ}{A}$ diameter dotes on 200 $\overset{\circ}{A}$ square centers is considered; this is a two-dimensional array of quantum boxes. The energy of the fundamental eigenstate, as it is effective for the transition, is considered distributed with a breadth of 6.6 eV. These conditions imply a density of transitions of 3.8 10^{13} $\frac{1}{cm^2\ eV}$. The tight confinement implies a photon energy of about 1.7 eV. Using the scaled matrix element, *Equation 6.29*, a maximum gain of 46 $\frac{1}{cm}$ for the first state transition is computed for this particular quantum-dot laser structure and an optical mode width of 3000 $\overset{\circ}{A}$. According to a recent publication on the concept of quantum-box lasers, by Vahala [6] *Figure 10*, a maximum gain of about 70 $\frac{1}{cm}$ is obtained after appropriate scaling. Using the 46 $\frac{1}{cm}$ of maximum obtainable gain and concepts from *Chapter 6.6*, a transparency current density of 7 $\frac{A}{cm^2}$ is computed. A pump-current density of about 32 $\frac{A}{cm^2}$ will provide 30 $\frac{1}{cm}$ of modal gain for a mode of 3000 $\overset{\circ}{A}$ width. This calculation is on the optimistic side because it excludes the effects of higher-order states. The quantum-dot laser is at the theoretical state only, because a way to fabricate these structures with the required fabrication tolerance has not yet been demonstrated.

The estimates for these presented quantum-wire and quantum-box structures and results from *Chapter 7.2* and *Chapter 7.5* allow a direct comparison of the relative performance of lasers with different dimensions, i.e., bulk, quantum-well,

Dimension	3	2	1	0
Name of laser	Bulk	Well	Wire	Box
$<\omega>$ / $\mathring{A}$	2000	100	50	13
j_0 / $A\ cm^{-2}$	712	81	~ 27	7
τ_0 / ns	5.6	6.0	~ 6	2.8
$\aleph_0$ / $10^{12}\ cm^{-2}$	24.8	3.1	~ 1	0.125
j_{th} / $A\ cm^{-2}$	1004	293	~ 133	32
τ_{th} / ns	4.8	4.2	~ 3	1
$\aleph_{th}$ / $10^{12}\ cm^{-2}$	29.8	7.7	2.5	0.207
E_{ph} / eV	1.40	1.45	1.60	1.70
E_{ex} / $k_B T$	0.58	2.65	~ 3	3.14
$\frac{dg}{dj}$ / $A^{-1}cm$	0.104	0.09	~ 0.15	0.79
$\frac{dg}{d\aleph}$ / $10^{-12}cm$	6.4	4.3	~ 12.0	365

Table 7.2 The results of estimations and calculated values of GaAs/GaAlAs lasers with different dimensionalities. $<\omega>$ is the average thickness of the active region and therefore a direct measure of the relative volume. Refer to the text for details.

quantum-wire, and quantum-box lasers as summarized in *Table 7.2*. The size of the
lasers is not implied except for having a transverse optical mode width of 3000 $\mathring{A}$
and a modal gain requirement of 30 $\frac{1}{cm}$ (the increased excited state absorption of
conventional lasers is accounted for by requesting 36 $\frac{1}{cm}$ of modal gain). A sub-μm
lateral wave-guide is probably equally as difficult to fabricate in a laser with a bulk
active region as in a laser with a quantum confined, active region. In all cases,
an energy smearing of 6.6 *meV* is used. This smearing enters in the case of bulk
and quantum-well lasers as was discussed in *Chapter 6*. In the case of wire and
box lasers, the smearing is similar. The manufacturing tolerances of the size of the
structure can be considered as the origin of the smearing [5, 6]. The quantum-box
structure would exhibit serious spectral hole-burning if the energy smearing would
be due only to the distribution of the size of the manufactured structure. The
transition-broadening as it is conventionally used applying a Lorentzian line-shape
function is not applied in any of the calculations.

The transparency condition considered is the case of transparency at the thresh-
old lasing wavelength. For the quantum-wire laser, the values presented in the *Table
7.2* are estimates only. Also, the gain slopes for the wire lasers are estimated by
assuming a proportionality of the density of state to the gain, g, and the average car-
rier lifetime in the vicinity of the threshold is assumed to be proportional to $\frac{1}{\sqrt{g}}$. The
results are summarized in *Table 7.2*. The specific three-dimensional structure is a
2000 $\mathring{A}$-wide, double heterostructure with the bulk properties as described in *Section
7.5*. The single-quantum-well laser is a 100 $\mathring{A}$ well structure as introduced in *Chap-
ter 7.2*. The size implies nothing specific with respect to the confinement structure
for the charge carriers if the required gain is not altered; therefore, it is excluded
from the comparison presented here. More general considerations, in particular,
scaling laws, have been published by Yariv [7] for three-, two-, and one-dimensional

semiconductor lasers. In conclusion, the experimental findings of improved performance of quantum-well lasers over double-heterostructure lasers is theoretically explained. The same order improvements for the transitions of quantum-wire and the quantum-box lasers under the assumption that very stringent manufacturing tolerances can be met, are predicted.

7.4 Figure of Merit of Quantum-Well Size

In this section the dependence of the quantum-well effects on the size of the well is considered. The detailed model of *Chapter 6* accounts for sizes of the well up to the large-size limit where quantum effects are totally negligible, the conventional double heterostructure of lasers. This separate treatment of the fundamental consequences of quantum-confinement is to highlight the quantitative effects as they become qualitatively important. The main point is to extract general information in contrast to the specific information provided by the application of the model in *Chapter 6*.

The condition for the quantum-size effect to be significant, is that the next higher confined state (that is, the onset of the second lowest subband) is spaced in energy more than the thermal energy $k_B T$. This is a necessary condition to make the subbands distinguishable on account of occupation.

The bulk case does not have any direction with tight confinement; therefore, there are no subbands (one could say that there is only one subband in three dimensions or that the number of the subbands is very large, depending on the point of perspective). In the bulk case, there are no quantum-confinement effects. In quantum-well lasers the smallest energy difference of subband onset energies is between the $n = 1$ heavy hole and the $n = 1$ light hole or the $n = 2$ heavy hole.

In order to get an estimate, twice the confinement energy of the heavy hole in an infinitely deep well will be used as the energy difference considered (the infinite wall well would place the first light hole higher than the second heavy hole, a situation that is often reversed in realistic conditions).

$$E_{spacing} = 2 \cdot E_1(hh) \tag{7.6}$$

$$E_1 = \frac{\pi^2 \cdot \hbar^2}{2 \cdot m \cdot W^2} \tag{7.7}$$

where m is the effective mass of the confined particle, and W is the full width of the confining structure. If the figure of merit is defined as the ratio of the thermal energy to this energy spacing, the figure of merit scales linearly with temperature and mass and quadratically with quantum-well width; it is

$$Figure\ of\ Merit\ = \frac{T \cdot W^2 \cdot M}{C} \tag{7.8}$$

$$C = \frac{\pi^2 \cdot \hbar^2}{k_B \cdot m_e} = 8.73 \cdot 10^{-15} m^2 K = 8.73 \cdot 10^5 \mathring{A}^2 K$$

where M is the effective mass in the units of the electron rest mass m_e. For the given effective mass of the heavy hole, room temperature, and the *Figure of Merit* of 1, the width of the well is 87.5 $\mathring{A}$ (approximately 90 $\mathring{A}$). The interpretation is that wells of 90 $\mathring{A}$ width exhibit partial quantum-well properties with respect to heavy holes, while only the wells small compared to 90 $\mathring{A}$ exhibit full quantum-well behavior. Substituting the effective mass of the *electron* for the heavy hole in *Equation 7.6* leads to a width of 209 $\mathring{A}$. The significance of this value (209 $\mathring{A}$) is that it approximates the well size up to which the quantization is explicit in the laser properties. This approximation does not consider that the transitions involve specific electrons and holes; the goal is to provide a general guideline, not a specific result.

For example, a single-quantum-well laser with a well width W_{qw} within these two limits ($90\overset{\circ}{A} < W_{qw} < 209\ \overset{\circ}{A}$) exhibits a gain spectrum with local maxima for the first and second quantized-state transition or at least a reminiscence of the two maxima in the curvature of the gain spectra between these transition energies. On the other hand, the gain of the first quantized-state transition will still show substantial increase (with increasing pumping strength) after the second quantized-state transition produces superior gain. Actually, the full quantum-well behavior is not easy to realize at room temperature because a well of sufficiently small width cannot be easily made deep enough to confine the second quantized state for the electrons in the GaAs/GaAlAs system. In other words, real GaAs/GaAlAs lasers will always be close to the limit where three-dimensional properties start to spoil the theoretically predicted improvements of the ideal two-dimensional system at room temperature.

7.5 Conventional Double-Heterostructure Laser

For quantum-well lasers, as explained in *Chapters 5* and *6*, the gain available at sufficient pumping densities (high enough quasi-Fermi levels) is limited by the number of contributing quantized states. Radical changes in lasing wavelength as a function of gain requirement can result. However, the conventional double-heterostructure laser exhibits only gradual changes in the lasing wavelength. The model of quantum-well structures presented in this thesis can be used even if the width is too large to let the structure exhibit quantum effects.

Applying the quantum-well model to a double heterostructure of width W allows us to compute the number of subbands N that contribute transitions for a given excess energy over the bandgap E_{ex}. The square-root of energy dependents
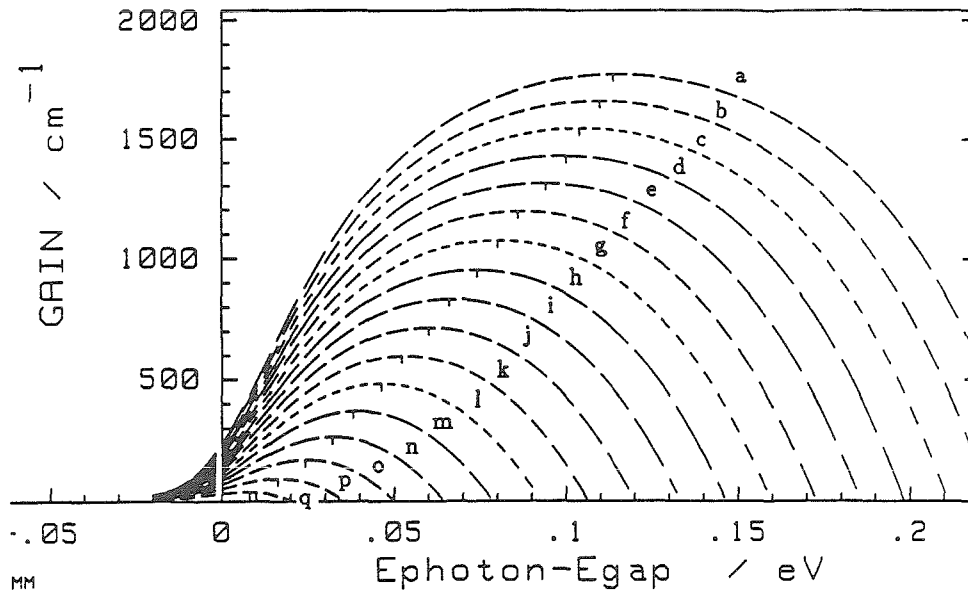
Curve	E_{Fe} eV	E_{Fh} eV	G_{max} $\frac{1}{cm}$	λ nm	N_{occ} $\frac{10^{12}}{cm^2}$	j $\frac{A}{cm^2}$	η ns
a	0.22	0.0161	1772.6	824.3	161.5	13650	1.89
b	0.21	0.0136	1659.5	826.5	150.7	12744	1.89
c	0.20	0.0109	1545.1	829.9	140.3	11807	1.90
d	0.19	0.0082	1429.0	832.1	130.2	10839	1.92
e	0.18	0.0054	1311.6	835.4	120.3	9847	1.96
f	0.17	0.0026	1193.1	840.0	110.8	8843	2.01
g	0.16	-0.0004	1074.1	843.4	101.5	7839	2.07
h	0.15	-0.0035	954.6	846.9	92.6	6855	2.16
i	0.14	-0.0067	835.2	851.5	83.9	5908	2.27
j	0.13	-0.0101	716.0	855.0	75.6	5013	2.41
k	0.12	-0.0136	597.9	859.8	67.7	4184	2.59
l	0.11	-0.0173	482.6	863.4	59.9	3430	2.80
m	0.10	-0.0212	371.2	868.2	52.7	2758	3.07
n	0.09	-0.0254	267.1	871.9	45.9	2170	3.39
o	0.08	-0.0298	173.4	876.8	39.5	1666	3.81
p	0.07	-0.0345	95.5	881.8	33.6	1246	4.33
q	0.06	-0.0395	39.4	886.8	28.2	903	5.01

Figure 7.6 Gain spectra of bulk GaAs as it is effective in conventional, double-heterostructure lasers. The table gives parameters for the traces shown. Note that the gain is very high for the upper traces. Only the traces (p) and (q) correspond to usual operational conditions.
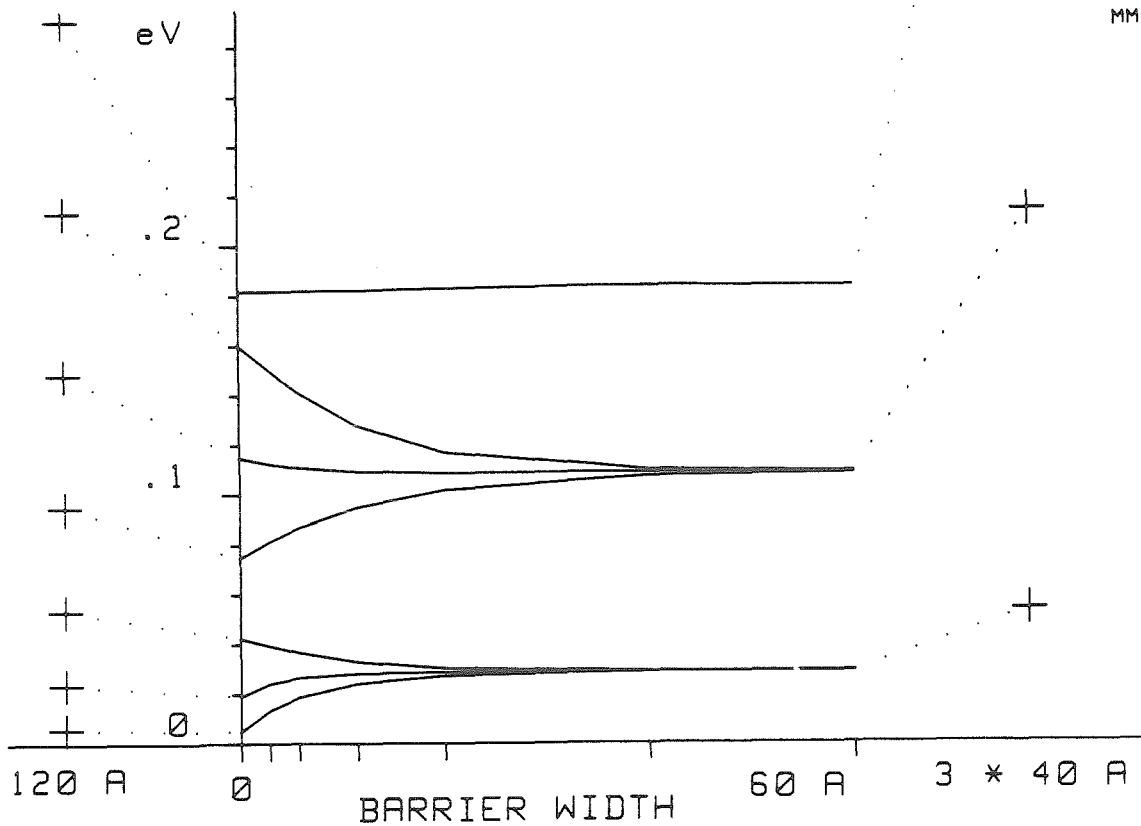
Figure 7.7 Eigenenergies for heavy holes of a multiple-quantum-well structure. On the left and right extremes, the eigenenergy for the case of an infinite wall well of 120 Å and 40 Å, respectively, are indicated as reference and first approximation. The traces give the eigenenergy of the six lowest eigenstates as a function of the barrier width from 0 to 60 Å in a realistic structure. The height of the barriers is below the seventh eigenvalue, which is hardly influenced in the transition from one large quantum well to a triple-quantum well. Note that the eigenenergies are, in general, lower than the infinite-wall-well approximation, with the exception of the fourth state, which actually has a higher eigenenergy in the triple quantum-well structure than in the single, infinite wall well.

of the density of states in three dimensions is achieved by the density of subbands in this description. Using the reduced masses of the heavy-hole and light-hole transitions, respectively, $M_{th} = 0.0567$ and $M_{tl} = 0.0378$, for a 2000 $\mathring{A}$ structure, the number of subbands is found via *Equation 7.9*. The number of subband transitions, N, is:

$$N = 141 \cdot \sqrt{\frac{E_{ex}}{eV}} \tag{7.9}$$

of which 45% are light-hole transitions. Estimating the possible gain per transition to be 100 $\frac{1}{cm}$ indicates that the conventional double heterostructure has the potential of providing hundreds, even thousands, of $\frac{1}{cm}$ gain coefficient. This is a well-known property of bulk GaAs material.

Consequently, moderate excess energy (the difference between the quasi-Fermi levels minus the bandgap energy) is needed to make large gains possible. A typical resonator does not require that kind of gain; therefore, the large potential gain is not exploited. Actually, very large current densities will not make this kind of operational condition attractive. In *Figure 7.6*, approximate gain spectra are shown for the bulk of a double heterostructure; typical gain requirements correspond to a range between curves (p) and (q). As discussed, the quantum effects are not evident in this case, because adjacent transverse eigenstates are energetically much closer to each other than $k_B T$, making their population nearly equal.

7.6 Single- versus Multiple-Quantum-Well Laser Structures

After the single-quantum well and the conventional double-heterostructure laser have been treated, another variant of laser structures is described here. If the gain requirement is higher than the gain that a single-quantum well can provide and if a low-threshold current density is desired, a multiple-quantum-well structure
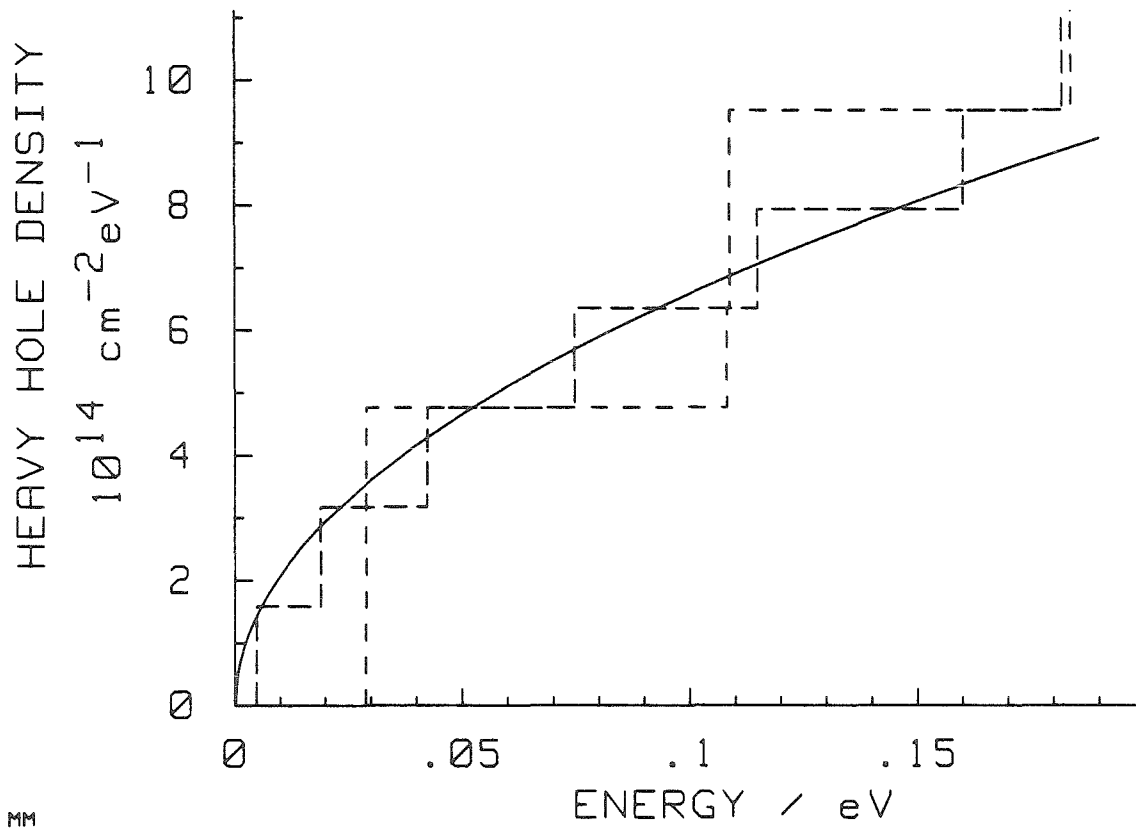
Figure 7.8 Scheme of the density of the hole states without smearing for a thick, single-quantum well, three equally thin quantum wells of the same total widths and the continuum limit for the same total width. In quantum-well lasers, eigenenergies of the confined states are lower than the infinite wall-well approximation suggests. Therefore, the steps in the density-of-states function cross the $\sqrt{E}$ curve of the continuum limit rather than are confined under it.

can be employed. The main effect of multiple-quantum-well structures on the eigenvalues is shown in *Figure 7.7*. The particular case of the heavy-hole eigenvalues of a quantum well is shown where the quantum well is converted into a triple-quantum well by introducing two barriers to split the single-quantum well into three equally thick fractions. The total width of the active region is not altered and as can be seen, the number of quantized states does not change.

The eigenenergies are shifted and reorganized to form groups with the same number of members as the number of quantum wells as long as the eigenenergies are substantially below the height of the barriers and the barriers have significant thickness. This is shown in *Figure 7.8*, where a schematic of the density of heavy-hole states is given for the thick, single-quantum well, the three equally thin quantum wells and the continuum limit. Smearing of the onset energies is not included.

The effect is caused by the influence of the barrier on the dispersion relation. Thick enough barriers have such a strong effect that each group of eigenvalues is found conveniently by applying the perturbation theory [8] similar to the treatment of array lasers in the supermode theory [9]. The result is an arrangement of quantized states similar to that of a single-quantum well of a given form but multiplied by the number of quantum wells of that form in the structure. The very small spacing in eigenenergy in a group occurs only if the individual quantum wells are identical.

The benefit of this rearranged density of quantized states is that the spacing between the groups is large so that the occupation of one group may be high, but the other group exhibits only low occupation. Under the given conditions, the considerations outlined in *Section 7.4* apply for the overall structure. Even so, the accumulated thickness of the wells may be large; the quantum-well effects show

according to the width of the individual well. Overall, the multiple-quantum-well structure has the strength to provide high gain, retaining the relative benefits of the quantum-well structure over the conventional structure as discussed in *Section 7.3*. The multiple-quantum-well structure has been very popular over the last several years, mainly because single-quantum-well material with very high quality is more difficult to produce. The growth procedure implies an increase in the quality of the wells with the number of preceding wells, a feature that single-quantum-well structures cannot benefit from. The moderate gain requirement of very high quality material and a long resonator with uncoated facets is *optimally* met with a *single-*quantum-well structure, a fact that may not have been appreciated enough so far.

7.7 Optimized Transverse Structure Single-Quantum-Well Laser

In the GaAs/GaAlAs system the transverse structure is given by the transverse Al-concentration profile. The Al-concentration governs the potential for the charge carriers and the permittivity for the optical wave-guide. The parabolic optical wave-guide considered in *Chapter 7.2* is but one possible transverse structure. Two parameters for the transverse electromagnetic guiding structure have been introduced: first defining the effective width of the optical mode W_{em}, which enters inversely into the modal gain of quantum-well lasers. Secondly, the structure is limited to guide only the fundamental mode in order to avoid transverse mode competition. Optimization can aim at the lowest possible threshold-current density, asking for a small W_{em}. On the other hand, exactly the opposite requirement results from the facet-damage intensity limit at high-power operation. A large W_{em} also eases the demand on the optical system outside the crystal wave-guide by reducing the full-angle-at-half-intensity transverse spreading of the beam by diffraction, which may become a major practical concern for optimizing the efficiency of the

laser with respect to usable output power. The example given in this section is of the type with a rather large optical mode, trading the lowest threshold in favor of high-power capability and lower transverse diffraction.

Large transverse optical-mode width is obtained by confining structures that can be made either very narrow or wide and shallow. In the first case, weak guiding leads to long exponential tails requiring thick cladding layers to prevent excess leaking. This structure is very sensitive to asymmetry in the permittivity of the upper and lower cladding layer. The alternative is a structure about as wide as the effective width of the optical mode, but shallow enough to stay within the limit of not guiding the second-order optical mode. A steep transition is favorable to terminate the guiding structure at the side with respect to mode discrimination.

Further considerations involve the effects concerned with transporting the charge carriers into the quantum well. An improved funnel effect and therefore an improved capture ratio for the carriers can be expected if the potential decreases toward the quantum well. This argument applies for both sides because the electrons and holes are injected in opposite directions. Recent findings indicate contradictorily that quantum-well lasers with just as good properties have been obtained with or without graded outer regions [10]. Our experiments, in which quantum-well lasers have been driven to more than 65 times threshold current [11, 12], suggest that efficient funneling of the charge carriers is at a premium at high-power operation because the effective lifetime of these carriers is reduced to well below 100 ps.

Furthermore, there is experimental evidence that injecting the charge carriers into a quantum well can be slow; more than 10 ps have been measured. From experience of the shape of the eigenfunctions of charge carriers in a symmetric
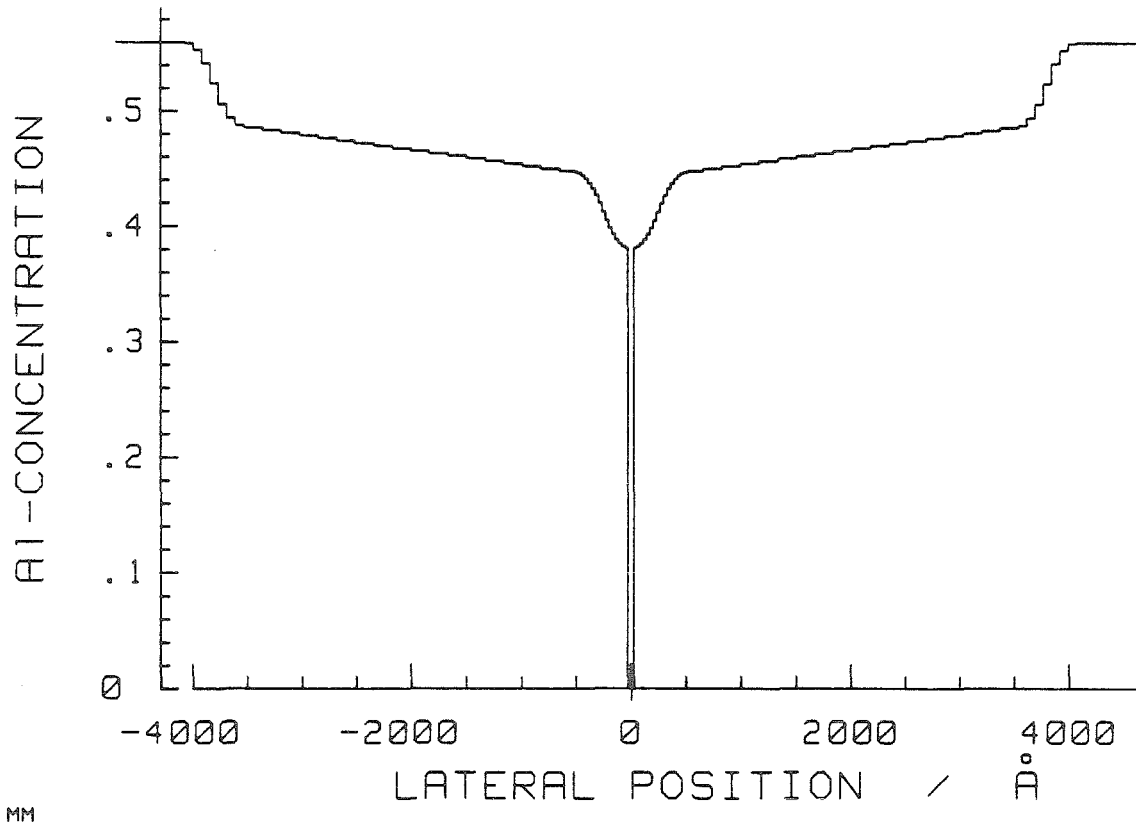
Wavelength nm	Permittivity Eigenvalue	Equivalent Al-Concentration	Leak	Effective Width/Å
886	10.771	0.483	$20 \cdot 10^{-6}$	5266
827	11.031	0.484	$5 \cdot 10^{-6}$	4881
775	11.295	0.467	$1 \cdot 10^{-6}$	4553

Figure 7.9 Proposed transverse structure of a high-power laser. The transverse Al-concentration profile is given; refer to text, *Section 7.7*, for details. The table provides information on the wave-guiding properties of this structure. This table is comparable to the table presented in *Figure 7.3*.

WAVELENGTH / nm

840 820 800 780 760 740 720 700
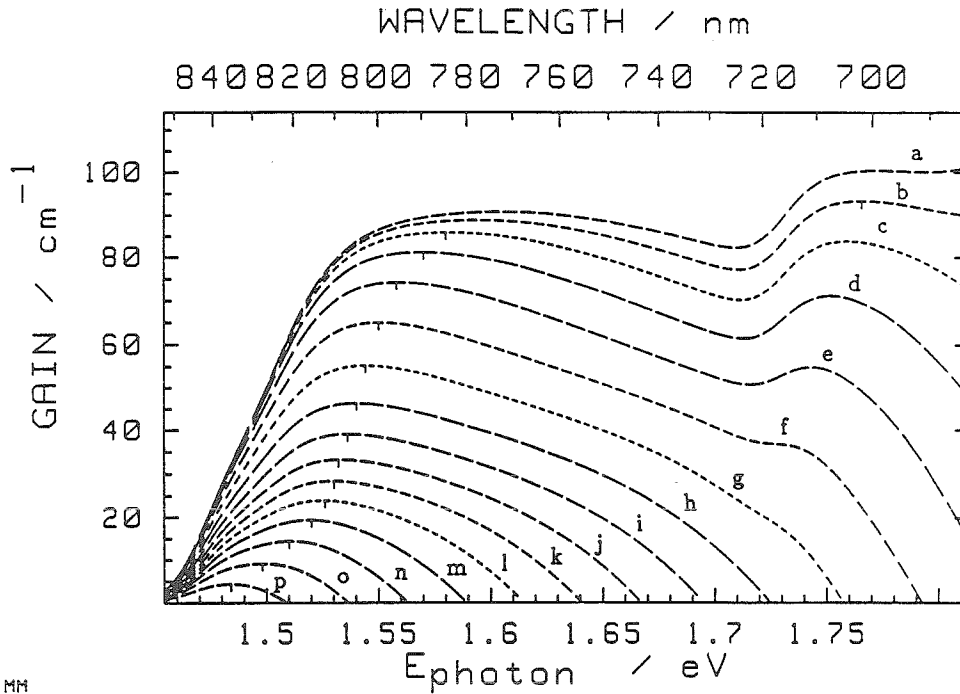
Curve	E_{Fe}	E_{Fh}	G_{max}	λ	N_{occ}	j	τ
	eV	eV	$\frac{1}{cm}$	nm	$\frac{10^{12}}{cm^3}$	$\frac{A}{cm^2}$	ns
a	0.44	0.1541	101.0	683.5	108.3	3910	4.44
b	0.42	0.1426	93.3	702.0	82.2	3600	3.66
c	0.40	0.1289	85.8	784.7	59.4	3210	2.97
d	0.38	0.1130	81.2	789.7	41.3	2740	2.41
e	0.36	0.0957	74.1	795.8	28.0	2230	2.01
f	0.34	0.0785	65.0	799.9	19.1	1731	1.77
g	0.32	0.0634	55.2	803.0	13.5	1310	1.65
h	0.30	0.0510	46.3	805.1	10.0	988	1.61
i	0.28	0.0411	39.1	807.2	7.7	758	1.64
j	0.26	0.0333	33.3	809.3	6.3	590	1.70
k	0.24	0.0268	28.5	810.3	5.2	464	1.81
l	0.22	0.0209	24.0	812.5	4.4	362	1.95
m	0.20	0.0152	19.4	815.7	3.7	277	2.16
n	0.18	0.0092	14.4	821.1	3.1	203	2.45
o	0.16	0.0026	9.2	827.6	2.5	140	2.88
p	0.14	-0.0051	4.4	835.4	1.9	88	3.56

Figure 7.10 Gain calculations of the proposed high-power structure. Gain spectra at different pumping strengths are shown. The table gives parameters for the curves shown. The optimum gain requirement for this structure is a rather low 20 $\frac{1}{cm}$. This is caused by the wide optical mode, which increases the maximum output power before facet damage is limiting.

confining structure at flat-band-condition, it seems advisable to introduce a small transition structure to improve injection from the larger outer structure into the comparably narrow quantum well.

After introducing the qualitative features of the transverse profile, some additional considerations about the Al-concentration are made. The laser action is based on the direct bandgap of GaAs and GaAlAs for Al-concentrations below about 0.42. The indirect bandgap material has been used for the outer structure with success; however, the structure next to the quantum well may be preferably direct bandgap material. Direct bandgap material requires the Al-concentration to be below 0.42 and therefore limits the depth of the quantum well. Also, the region of the inner transition structure next to the quantum well should also be of direct bandgap material.

In *Figure 7.9*, the proposed transverse structure is shown; the transverse Al-concentration profile is given. The quantum well is rather thin to provide a strong quantum-well effect. The thickness is chosen so that the second electron state is still well confined in the quantum well, giving a lower limit for the width. In *Figure 7.10*, gain spectra for different pumping strengths are shown. The calculations reveal that the optimum gain requirement is rather low, being 20 $\frac{1}{cm}$. The gain reduction is due to the larger optical-mode width, which is about 1.5 times as large as the width of the example described in *Section 7.2*. The transition to the second quantized-state lasing at high gain (90 $\frac{1}{cm}$) is due to the narrow quantum well. The narrow quantum well leads to a high band filling at the first quantized state before the second quantized state transition shows superior gain.

7.8 Scaling Law for Optical and Carrier Confinement in Heterostructures

The transverse structure of the semiconductor laser diode has to perform two functions: The optical mode has to be guided, and the charge carrier has to be confined. These requirements have been addressed in *Chapter 6*; it was found that the mathematical treatment can be performed with one generalized formula for both cases. The inherent fundamental scaling law is extracted from the physical properties of the GaAs/GaAlAs system. Neglecting nonlinearities and spectral dependence, the permittivity can be approximated by

$$\varepsilon(x) = \varepsilon_{or} - X \cdot \varepsilon_s \qquad (7.10)$$

with $\varepsilon_{or} = 13.25$ and $\varepsilon_s = 5.5$ for a wavelength of 845 nm, corresponding to $k_0 = 7.44 \cdot 10^4 \frac{1}{cm}$. Similarly, the direct bandgap can be approximated, at least for Al-concentrations that are not high.

$$E_g(X) = E_{g0} + X \cdot E_s \qquad (7.11)$$

where $E_{g0} = 1.424\ eV$ and $E_s = 0.67 \cdot 1.247\ eV$ for electrons, and $E_s = 0.33 \cdot 1.247$ eV for holes at room temperature. Considering an eigenvalue equivalent to the Al-concentration-dependent material parameter as given in *Equations 7.10* and *7.11* leads to differential equations in GaAs as follows:

$$\frac{-d^2}{d\left(\frac{\sqrt{2 \cdot E_s \cdot X}}{\hbar} \cdot x\right)^2}\ \psi = \psi \qquad (7.12)$$

$$\frac{-d^2}{d\left(k_0 \cdot \sqrt{\varepsilon_s \cdot X} \cdot x\right)^2}\ \psi = \psi \qquad (7.13)$$

The equations are rewritten in implicit units. Using these units, the phase density is derived to be for the optical mode

$$\kappa_{optical} = k_0 \cdot \sqrt{\varepsilon_s \cdot X} = 1.74 \cdot 10^7\ m^{-1} \cdot \sqrt{X} = \frac{\sqrt{X}}{573\mathring{A}} \qquad (7.14)$$

and for the charge carrier, in particular, the electrons

$$\kappa_{carrier} = \frac{\sqrt{2 \cdot m \cdot E_s \cdot X}}{\hbar} = 1.21 \cdot 10^9 \; m^{-1} \cdot \sqrt{X} = \frac{\sqrt{X}}{8.3\mathring{A}} \qquad (7.15)$$

the length scale changes from 8.74 $\mathring{A}$ for the electrons to 10.3 $\mathring{A}$ for light holes and 4.98 $\mathring{A}$ for heavy holes.

The significance of *Equations 7.14* and *7.15* is that the structure confining the optical mode has to be two orders of magnitude larger than the structure confining the charge carriers, if both structures have about equal depth and provide equally tight confinement. A single structure for optical guiding and confinement of electrons as used in traditional double-heterostructure lasers is significantly mismatched. A single-mode optical confinement is well matched to a single confined state for the electrons as is implemented in modern, thin, single-quantum-well lasers. As pointed out, this structure provides all the gain needed for long, uncoated facet lasers.

7.9 Conclusion

It has been shown that the single-quantum-well transverse structure meets the gain requirement of typical length GaAs/GaAlAs semiconductor lasers. In comparison to conventional, double-heterostructure lasers and multiple-quantum-well lasers, the threshold current density is minimum, and the distributed losses of high-quality material are also minimum. The material-dependent parameters imply that the guiding structure around the quantum well for the optical mode is to be up to two orders of magnitude wider than the well. Several varying structures for this guide are used, but a thorough optimization has not yet been published. A particularly advanced structure is introduced.

The increased performance of the single-quantum-well lasers with respect to the conventional, double-heterostructure lasers and in many cases the multiple-quantum-well lasers has not yet led to a dominance of this structure in the commercial laser market. Proposed structures of quantum-wire and quantum-dot lasers promise two- to five-fold improvements in threshold current densities for the future (may be more for optimized structures). The improvements depend critically on the manufacturing capability of very high uniformity of these quantum structures.

7.10 References

[1]. Casey H.C. Jr., D.D. Sell, and M.B. Panish: *"Refractive index of $Al_xGa_{1-x}As$ between 1.2 eV and 1.8 eV."* Appl. Phys. Lett. **24**(2):63-65 (1974).

[2]. Fern R.E., and A. Onton: *"Refractive index of AlAs."* J. of Appl. Phys. **42**(9):3499-3500 (1971).

[3]. Yariv A.: *Quantum Electronics.* John Wiley and Sons: New York, 3rd. edition (1989), p.273.

[4]. Yamada M.: *"Anisotropy and broadening of optical gain in a GaAs/AlGaAs multiquantum-well laser."* IEEE J. Quantum Elect. **QE-21**(6):640-645 (1985).

[5]. Zarem H., K.J. Vahala, and A. Yariv: *"Gain spectra of quantum wires with inhomogeneous broadening."* To appear in IEEE J. Quantum Elect. **QE-25**(4), (1989).

[6]. Vahala K.J.: *"Quantum box fabrication tolerance and size limits in semiconductors and their effect on optical gain."* IEEE J. Quantum Elect. **QE-24**(3):523-530 (1988).

[7]. Yariv A.: *"Scaling laws and minimum threshold currents for quantum-confined semiconductor lasers."* Appl. Phys. Lett. **53**(12):1033-1035 (1988).

[8]. Schiff L.I.: *Quantum Mechanics.* McGraw-Hill Book Company: New York, 3rd. edition (1968).

[9]. Kapon E., J. Katz, and A. Yariv: *"Supermode analysis of phase-locked arrays of semiconductor lasers."* Optics Letts. **10**(4):125-127 (1984).

[10]. Streifer W., personal communication, November 1988.

[11]. Larsson A., M. Mittelstein, and A. Yariv; unpublished.

[12]. Chen H.Z., M. Mittelstein, and A. Yariv; unpublished.

<div align="right">Chapter Eight</div>

8: Semiconductor Lasers
with an External Tuning Resonator

Abstract

Quantum-well lasers are shown to exhibit flattened, broadband gain spectra at a particular pumping condition. The gain requirement for a grating-tuned external cavity configuration is examined and is applied to a semiconductor quantum-well laser with an optimized length of gain region. The coupled-cavity formalism is employed to examine the conditions for continuous tuning. The possible tuning range of double-heterostructure lasers is compared to that of quantum-well lasers. The predicted broadband tunability of quantum-well lasers is confirmed experimentally by grating-tuning of uncoated lasers over 85 nm, with single, longitudinal mode output power exceeding 200 mW.

8.1 Introduction

In this chapter, a theoretical investigation and an experimental verification of the gain characteristics of quantum-well semiconductor lasers are presented, which demonstrate that nearly constant gain can be achieved over an extended spectral range. Such a wide, flat gain spectrum is a prerequisite for practical broadband tunability, whose utility has been proven by the popularity of dye lasers. Following the examination of the resonator used in the experimental investigation, the parameterization of the external tuning cavities is generalized and applied to the case of continuous tuning. In a theoretical comparison, the conventional double
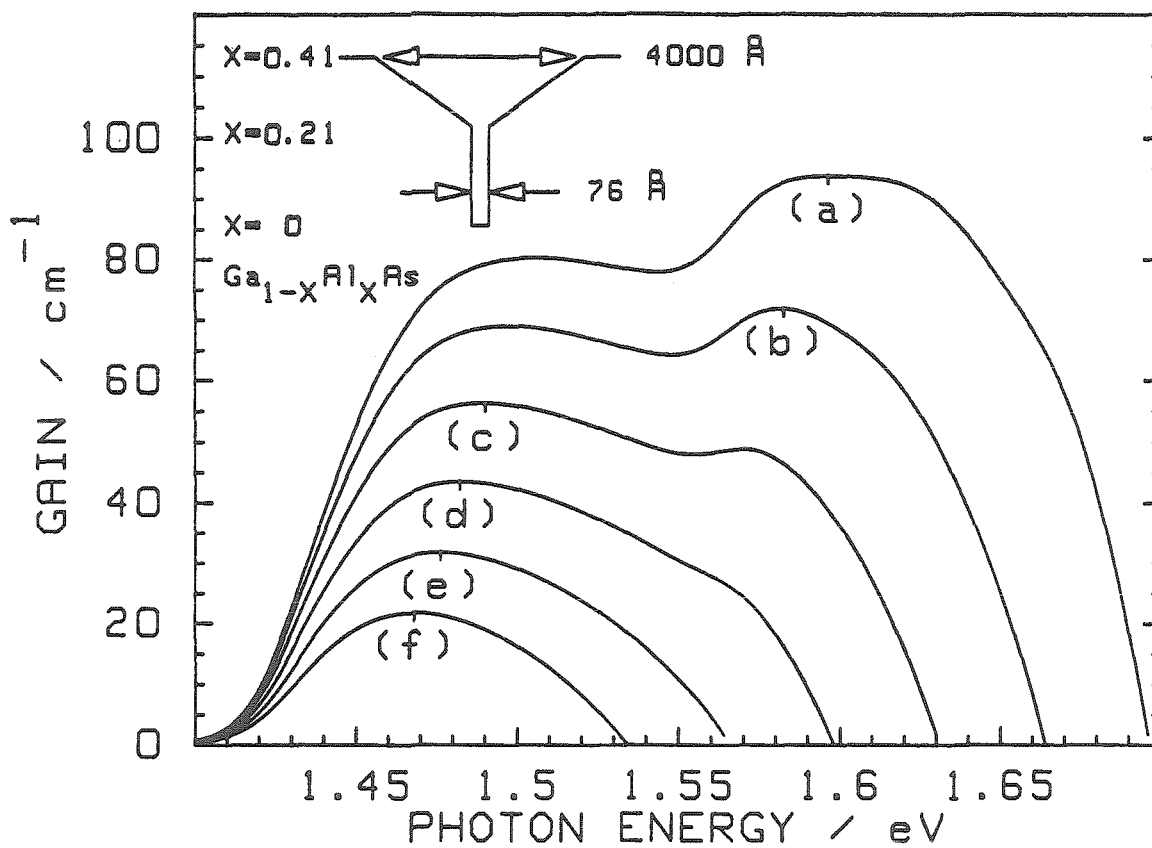
Figure 8.1 Computed gain spectra of a single-quantum-well laser under various pumping strengths. The pump current density is (a): 1830, (b): 1350, (c): 950, (d): 630, (e): 405, and (f): 255 $\frac{A}{cm^2}$, respectively. The particular linear GRINSCH-SQW structure considered is indicated in the inset.

heterostructure is shown to exhibit gain spectra of approximately equal width at comparable band filling but with an order-of-magnitude increase of required pump current density. Experimentally, the flattened gain spectrum of quantum-well lasers is demonstrated by broadband tuning in a grating-tuned external cavity.

Tuning of semiconductor lasers with an external grating has been demonstrated previously, and a tuning range in excess of 3.5% at 1.5 μm has been realized [1]. A refined version of a long-wavelength semiconductor laser has been reported to be tunable over 9% of a spectral width of 74 meV [2]. In the GaAs/GaAlAs system, superluminescent light-emitting diodes (SLEDs), fabricated from multiple-quantum-well material, have been made to lase in an external cavity over a tuning range of 6.0% (CW) and 8.0% (pulsed) in the vicinity of 780 nm [3]. In this chapter, the existence of a flattened gain spectrum in quantum-well media under proper pumping is demonstrated. By taking advantage of the flattened gain spectra, the tuning of an *uncoated* single-quantum-well, broad-area semiconductor laser over a range exceeding 10% near 800 nm is demonstrated [4-6].

8.2 Gain-Flattened Condition of Quantum-Well Lasers

The model for the gain of quantum-well semiconductor lasers developed in *Chapters 6* and *7* is used for calculation of the gain spectra at high pumping currents. *Figure 8.1* shows the theoretical gain spectra at various pumping strengths for the single-quantum-well structure defined in the inset. Curve (b) in *Figure 8.1* shows the *gain-flattened* spectrum.

The distinct onset of the subbands in the quantum-well laser allows for more than one local maximum in the gain spectrum. Specifically, in a single-quantum-well structure, *the pumping strength can be adjusted* so that equally high gain peaks

arise from the first and second quantized-state transitions, resulting in a wide spectral region of near equal gain (*Figure 8.1 (a), (c)*). The shape of the gain spectrum under this pumping condition is specific to quantum-well lasers. Conventional, double-heterostructure lasers do not exhibit concave regions in the center of the gain spectra but rather show single, bell-shape gain spectra (refer to *Figure 7.5*). The width of the flattened gain region is directly related to the separation of the first and second quantized-state transition, which is a function of the transverse structure, in particular, the width of the quantum well. With increased separation, the dip between the maxima increases and may become the practical limiting factor for increasing the width of the gain-flattened region in single-quantum-well lasers. The depth of the dip in the gain spectrum can be reduced by using a multiple-quantum-well structure with slightly different well width. The different well width separates the quantization energies, particularly of the second set of quantized states, effectively smearing out the onset of the higher photon-energy gain peak and filling in the dip in the gain spectrum.

Another method of stretching the width of the gain spectrum at a particular pumping strength is to take advantage of the high density of quantized-state transitions provided by the much increased width of the structure guiding the optical mode. If the quantum well is properly designed, the gain spectrum can exhibit three nearly equal gain maxima. The first two correspond to the first two quantized states in the quantum well, and the third maximum corresponds to the onset of the transitions of the wider outer structure of the wave-guide.
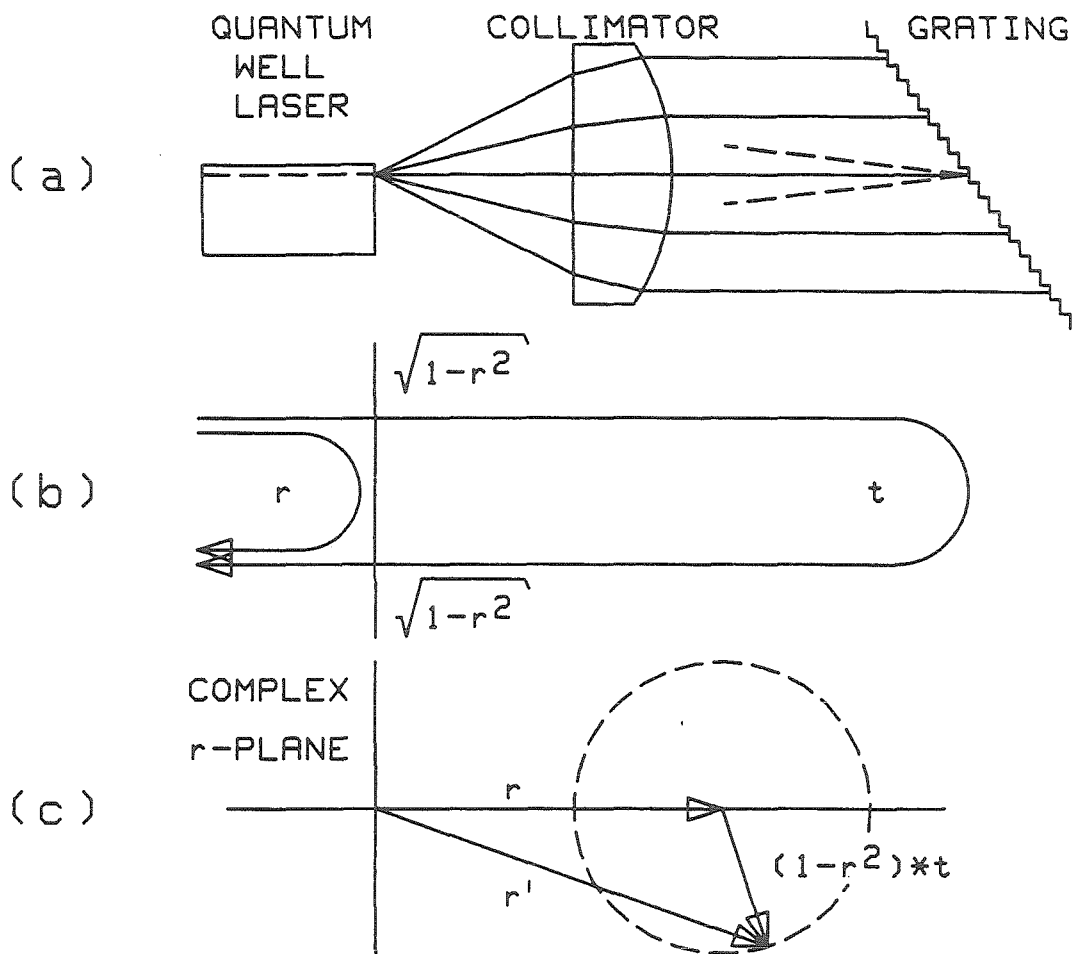
Figure 8.2 Schematic of (a) the external resonator configuration, and (b) the two main contributing beams for the rear side reflectivity. (c) Scheme of the coherent addition of the amplitudes of the two main contributing beams to form the complex reflection coefficient r'.

8.3 Tuning of Uncoated Crystal Cavities

A grating-tuned external resonator is investigated to find the gain requirement and in particular the required flatness to insure operation on the grating-selected wavelength.

A scheme of an external-lasing, wavelength-selective resonator is given in *Figure 8.2a*. The effect of the external resonator on the laser formed by a double-cleaved crystal resonator of a semiconductor laser can be modeled simply as a change in the effective complex reflection coefficient at the rear crystal facet from the value without external feedback r, to a value r':

$$r'(\omega) = r + (1 - r^2) \cdot t(\omega) \cdot e^{i\frac{2 \cdot \omega \cdot L_{ex}}{c}} \tag{8.1}$$

where ω is the radian frequency, $\omega = \frac{E_{ph}}{\hbar}$, L_{ex} is the length of the external resonator, and $t(\omega)$ is the amplitude transmission coefficient of the single-sided external cavity back *into the lasing mode* just outside the crystal. t therefore includes mode-mismatch losses in the coupling arrangement. *Equation 8.1* neglects multiple reflections in the external resonator, which is permissible as long as $|r \cdot t| \ll 1$. For grating-tuned feedback, the transmission amplitude of the external cavity $t(\omega)$ peaks at the Littrow frequency ω_0, i.e., the frequency that is retroreflected by the grating. As ω departs from ω_0, the coupling back from the grating into the laser mode just outside the facet becomes progressively smaller. Consequently, the spectral reflectivity $r'(\omega)$ is changed from the value r of the crystal facet alone *only* near the Littrow frequency. The requirement that the electric field reproduce itself after one round trip in the crystal resonator is expressed as

$$e^{(g(\omega) - \alpha_i)L} \cdot e^{i\frac{2 \cdot L \cdot n(\omega) \cdot \omega}{c}} \cdot r \cdot r'(\omega) = 1 \tag{8.2}$$
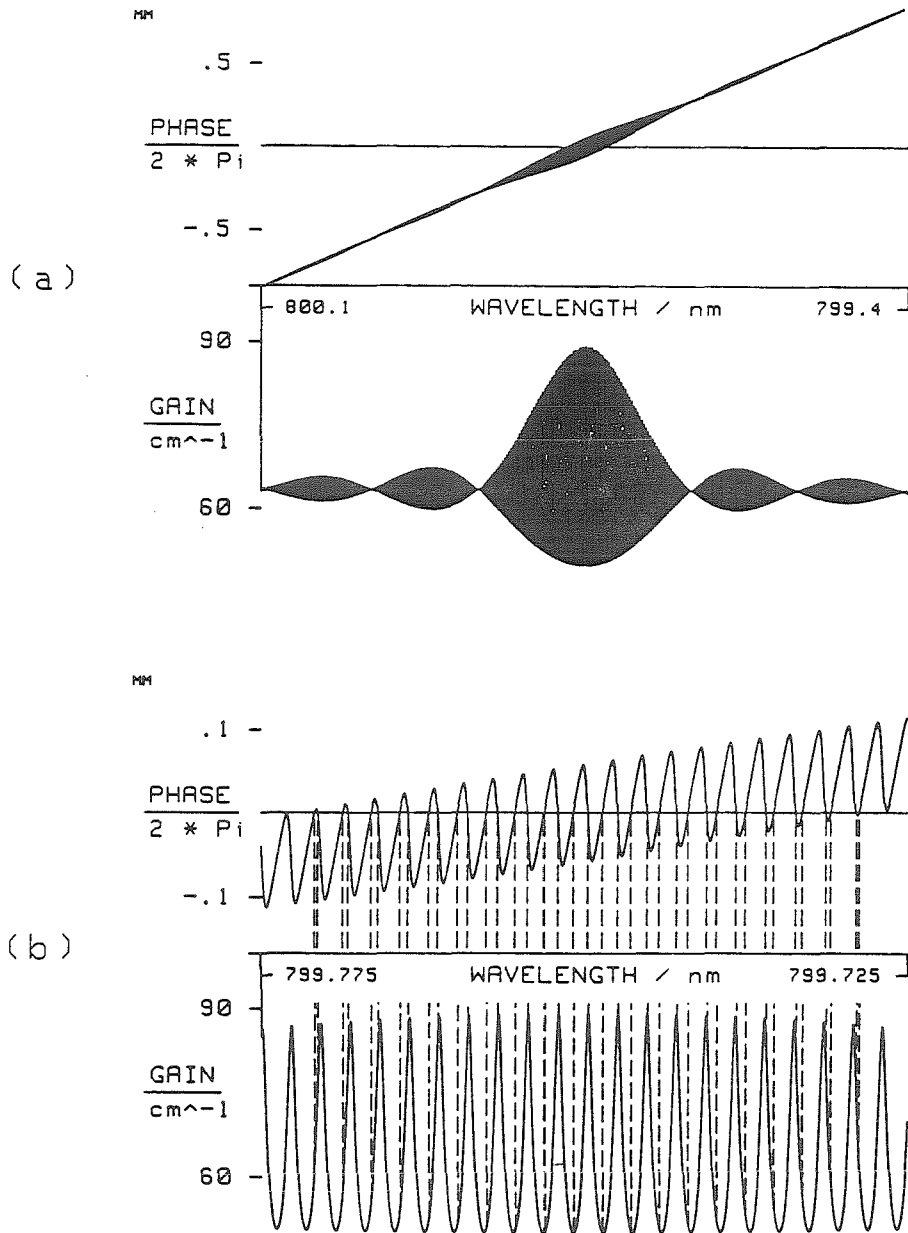
Figure 8.3 Computed phase modulo 2π and gain requirement of the composite cavity laser tuned to a crystal cavity resonance. The parameters correspond to the experimental condition of an uncoated laser. In (a) the wavelength selectivity of the external cavity is evident. In (b) an expanded section of the spectrum is shown and the 39 wavelengths where the phase condition *Equation 8.4* is fulfilled are indicated by vertical dashed lines. Near the center, the phase condition is met with the minimal gain requirement, the wavelength were lasing is expected.

where $g(\omega)$ is the modal power gain of the semiconductor medium, α_i are its distributed modal power losses, and L is its length. Considering separately the amplitude and the phase of *Equation 8.2* gives the following requirements for the frequencies of oscillation and their modal power gain at threshold of the composite cavity frequencies:

$$g(\omega) = \alpha_i + \frac{1}{L} \ln \left\{ \frac{1}{|r \cdot r'(\omega)|} \right\} \tag{8.3}$$

$$2\pi \cdot m = \frac{2L\, n(\omega)\, \omega}{c} + arctan \left\{ \frac{(1 - r^2) \cdot t(\omega) \cdot \sin\left(\frac{2\omega L_{ez}}{c}\right)}{r + (1 - r^2) \cdot t(\omega) \cdot \cos\left(\frac{2\omega L_{ez}}{c}\right)} \right\} \tag{8.4}$$

where m is an integer. The phase condition, *Equation 8.4*, is satisfied for a group of frequencies [7] clustered near the grating-selected longitudinal mode of the crystal resonator; the spacing within the group is approximately $\frac{\pi c}{L_{ez}}$. The corresponding threshold gains of these modes vary, however, because of the fast "oscillation" of $|r'|$ with ω (see *Equation 8.1*). In general, there will be one mode that corresponds closely to constructive interference from the external cavity if the number of solutions of *Equation 8.4* is sufficiently large. In this section, only the conditions of operating near resonance of the crystal cavity are considered. The continuous tuning will be addressed in *Section 8.4*. To be specific, the values for the variables closely resembling the experimental conditions described in *Section 8.6* are used, and the phase and gain corresponding to *Equation 8.3* and the right-hand side of *Equation 8.4* are shown in *Figure 8.3*. The phase is shown in the vicinity of $m = 1617$. The aperture of the lens assembly is considered to limit the spectral resolution to 0.23 *nm*. A hard aperture causes a $sinc^2$-response in the vicinity of the Littrow wavelength as illustrated in *Figure 8.3a*. In *Figure 8.3b* the spectral range shown is limited to the region where the phase condition is fulfilled and $t(\omega)$ is

$$\sqrt{1-r^2}$$

$$\sqrt{1-r^2}$$

(a)

(b)
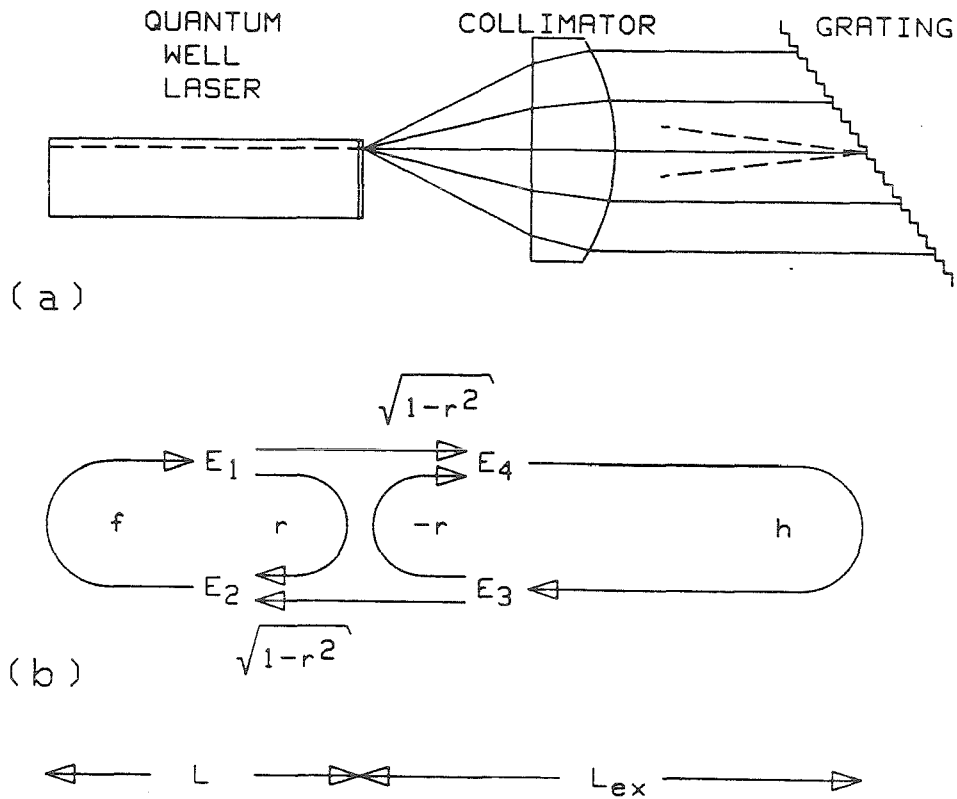
Figure 8.4 Schematic of (a) the external tuning cavity configuration. In (b) the coupling of the cavities is presented. The left-hand side presents the crystal cavity of length L with gain and output toward the left. The round-trip propagation is lumped in the coefficient f. The right-hand side presents the single-sided external cavity of length L_{ex} with the wavelength-dependent transmission coefficient, its round-trip propagation is lumped into the coefficient h.

significant. In the case of constructive interference at $\omega = \omega_0$, the gain requirement is minimized, and *Equation 8.2* with $2\pi \cdot m = \frac{2 \cdot L \cdot n(\omega) \cdot \omega}{c}$ and *Equation 8.4* give:

$$g(\omega_0) = \alpha_i + \frac{1}{L} \ln \left\{ \frac{1}{r \cdot (r + (1 - r^2)|t(\omega_0)|)} \right\} \tag{8.5}$$

If the round-trip gain first reaches unity at the tuned frequency ω_0, the composite resonator will lase at the corresponding photon energy. The tuning range is then determined by the flatness of the gain spectrum relative to the amount of grating feedback. The gain requirement of the single-sided, external-resonator composite-cavity laser is illustrated by two numerical examples: The value corresponding to *uncoated* facets of GaAs/GaAlAs lasers is about $r^2 = 0.3$. If $\alpha_i = 4.4 \frac{1}{cm}$, and $L = 0.019$ *cm*, then $t = 0.26$ leads to a 22.3% reduction in gain requirement. If the power transmission of the external cavity is reduced from 0.0676 (the estimated experimental condition and value used for *Figure 8.3*) to 0.01, then the feedback from the external cavity is effective in reducing the gain requirement by 9.3%. This 9.3% gain reduction is just about what is required to tune through the dip in the gain spectrum, (b) in *Figure 8.1*.

8.4 Continuous Tuning

The condition of continuous tuning of an external-tuning-resonator semiconductor laser is derived. The restriction $|r \cdot t| \ll 1$ used in *Section 8.3* allowed the multiple round trips in the external cavity to be neglected. In this section the coupled cavity formalism [8] is employed, which presents an *exact* method of treating the crystal and the external cavity in their interaction.

A minimum set of parameters to describe the composite cavity in the coupled-cavity formalism is introduced here and is indicated in *Figure 8.4*. The interface of

the crystal cavity and the external cavity exhibit a reflection coefficient of r inside the crystal, leading to a reflection coefficient of $-r$ inside the external cavity and transmission coefficient of $\sqrt{1 - r^2}$ in both directions. The round trip in the external cavity h is defined by its transmission coefficient t and an advanced phase $\frac{2 \cdot L_{ex} \cdot \omega}{c}$. Similarly, the round trip in the crystal resonator f is defined by its transmission coefficient $e^{L \cdot g} \cdot r_o$ and an advanced phase $\frac{2 \cdot L_{ex} \cdot n(\omega)}{c}$. L is the length of the crystal cavity, L_{ex} is the length of the external resonator, g is the power gain coefficient, and r_o is the reflection coefficient of the output side of the crystal resonator, the side opposite to the external cavity.

The complex ratio of the field amplitudes of the counterpropagating beams inside the crystal resonator at the interface can be considered in two ways [8] (refer to *Figure 8.4*): First, upon considering the round trip in the crystal cavity, the ratio of the field amplitude for the propagation toward the interface (E_1) with respect to the field amplitude for propagation leaving the interface (E_2) is f. Second, the round trip through the external cavity is considered. These two considerations for the same ratio imply:

$$f = \frac{1}{r + \frac{(1 - r^2) \cdot h}{1 + r \cdot h}} \tag{8.6}$$

If the amplitude and phase parts of h are t and s, respectively, then *Equation 8.6* can be rewritten as

$$f = \frac{1}{r + \frac{1 - r^2}{r + \frac{1}{t \cdot s}}} \tag{8.7}$$

The term $r + \frac{1}{t \cdot s}$ can never vanish because $0 < r < 1$ and $0 < t \leq 1$. The term $r + \frac{1 - r^2}{r + \frac{1}{t \cdot s}}$, on the other hand, can vanish for $s = -1$ and for particular pairs (r, t) defining critical values. The functional relation for the critical values is simply:

$$t_c(r_c) = r_c \tag{8.8}$$

The significance of the curve (r_c, t_c) is that it specifies the part of the two-dimensional parameter space $0 < r < 1$, $0 < t \leq 1$ of the composite cavity, where continuous tuning is impossible $(t < r)$.

The fundamental problem for continuous tuning with an external-tuning-resonator arrangement is to achieve a valid round-trip condition of the composed cavity at *every* wavelength in the tuning range. The worst case is destructive interference upon one round trip in the crystal cavity. This case corresponds to a real but negative f. Accordingly, the phase condition for the external resonator *Equation 8.7* implies $s = -1$. If $r = t$ (a pair of critical values), then the gain requirement is infinite ($\frac{1}{g} = 0$). In case that $t < r$, there is no solution with positive gain; therefore, lasing at the desired wavelength in the composite cavity is not possible, and continuous tuning cannot be achieved. On the other hand, if $t > r$, the pair (r, t) implies a finite positive gain. Using $s = -1$ in the case of $t > r$ results in constructive interference upon one round trip in the external cavity because of the $-r$ reflection coefficient. It also provides the needed out-of-phase component injected into the crystal cavity to annihilate the direct reflection and results in the following gain requirement.

$$g = \alpha_i + \frac{1}{L} \cdot \left(ln\frac{1}{r_o} + ln\frac{1}{\frac{1-r^2}{\frac{1}{t}-r} - r} \right) \tag{8.10}$$

The significance of *Equation 8.10* is that it gives the upper limit of the gain requirement under conditions of continuous tuning. In contrast, the minimum gain requirement is achieved when the crystal resonator is in resonance, and the external cavity shows a π phase change upon one round trip in the external cavity (note the reflection coefficient, $-r$, introducing the π phase change, $s = +1$). In this case, the external cavity feeds back into the crystal cavity in phase with the direct reflection,
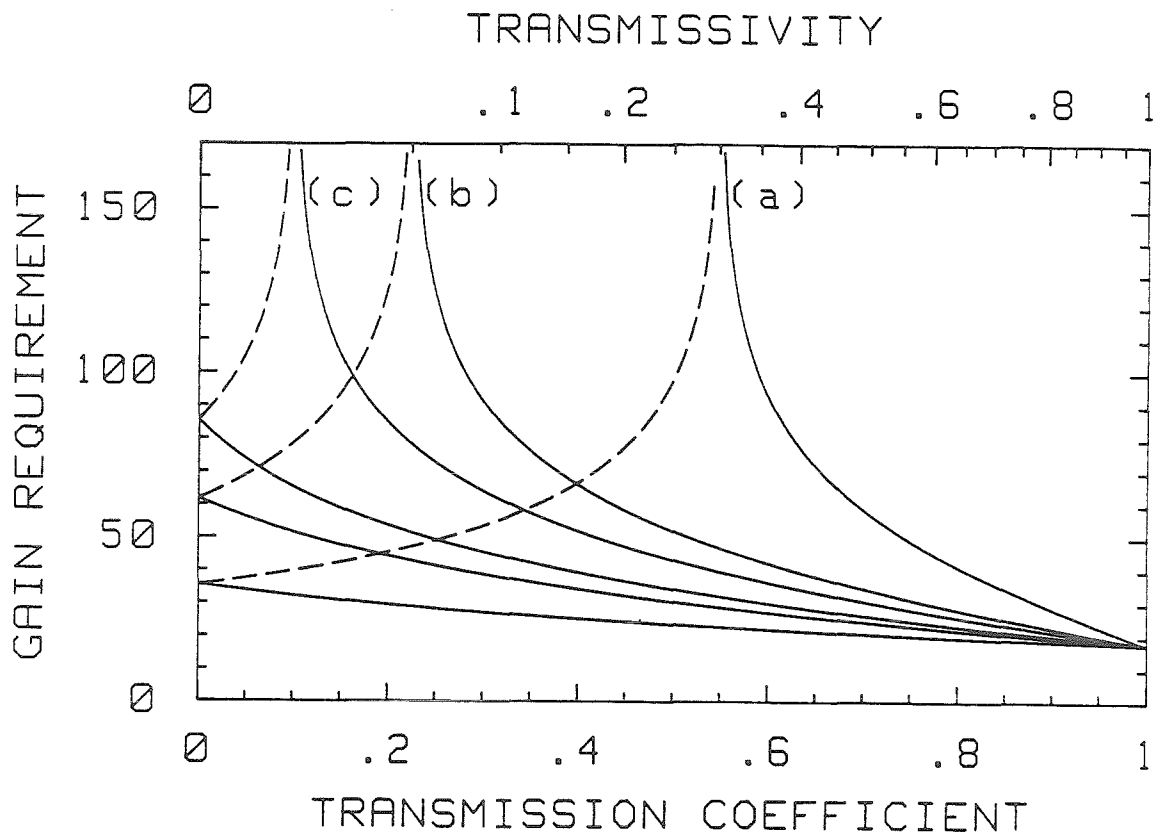
Figure 8.5 Computed gain requirement of the composite cavity laser as a function of external-resonator transmission coefficient for three values of facet reflectivity: (a) 0.30, (b) 0.05, and (c) 0.01. The output-facet reflectivity is a constant, 0.3, and the length of the cavity is 0.034 *cm*. The transitivity is shown on the top. Each lower curve corresponds to the case of resonance wavelength in the crystal cavity. The upper curve on the right side of the pole corresponds to the case of destructive interference for one round trip in the crystal cavity alone; the worst-case approximation for continuous tuning. The upper curve on the left side of the pole corresponds to the case of constructive interference for one round trip in the external resonator alone; continuous tuning is not possible in the region $t < r$.

and therefore the gain requirement is reduced to:

$$g = \alpha_i + \frac{1}{L} \cdot \left(ln\frac{1}{r_o} + ln\frac{1}{\frac{1-r^2}{\frac{1}{t}+r} + r} \right) \tag{8.11}$$

Equations 8.10 and *8.11* give the upper and lower limits of the gain requirement under conditions of continuous tuning. For a given crystal cavity, the wavelength determines the round-trip condition for the crystal cavity and therefore the actual gain requirement. Consequently, *Equations 8.10* and *8.11* give the bounds for the wavelength-dependent oscillation for the gain requirement. It should be noted that in practice, the dependence of the index of refraction n on the carrier density and therefore gain are influencing the modulation of the gain as a function of wavelength.

In *Figure 8.5*, the results of the two limiting gain requirements are plotted (solid lines) as functions of the transmission coefficient, t, for three values of the parameter reflection, r^2, i.e., 0.01, 0.0676, and 0.3. In *Figure 8.5* the region left of the pole corresponds to the case of dominant crystal-facet reflectivity $(t < r)$ and therefore noncontinuous tuning. The pole for the upper curves indicates the transition to the case of dominance of the external cavity, opening the possibility of continuous tuning for values of t larger than the critical value $(t > r)$. Furthermore, *Figure 8.5* indicates how large a gain modulation can be expected under continuous tuning. Basically, the gain requirement will change with tuning wavelength because the crystal resonator by itself provides constructive interference, changing to a π-phase shift and back to constructive interference, which has to be compensated for by the external cavity . The gain requirement will oscillate upon continuous tuning. The limits of the excursion of this gain requirement are shown in *Figure 8.5*. A very small reflection coefficient at the crystal facet and a high transmission through the external cavity are required in order to make wavelength-dependence of the gain
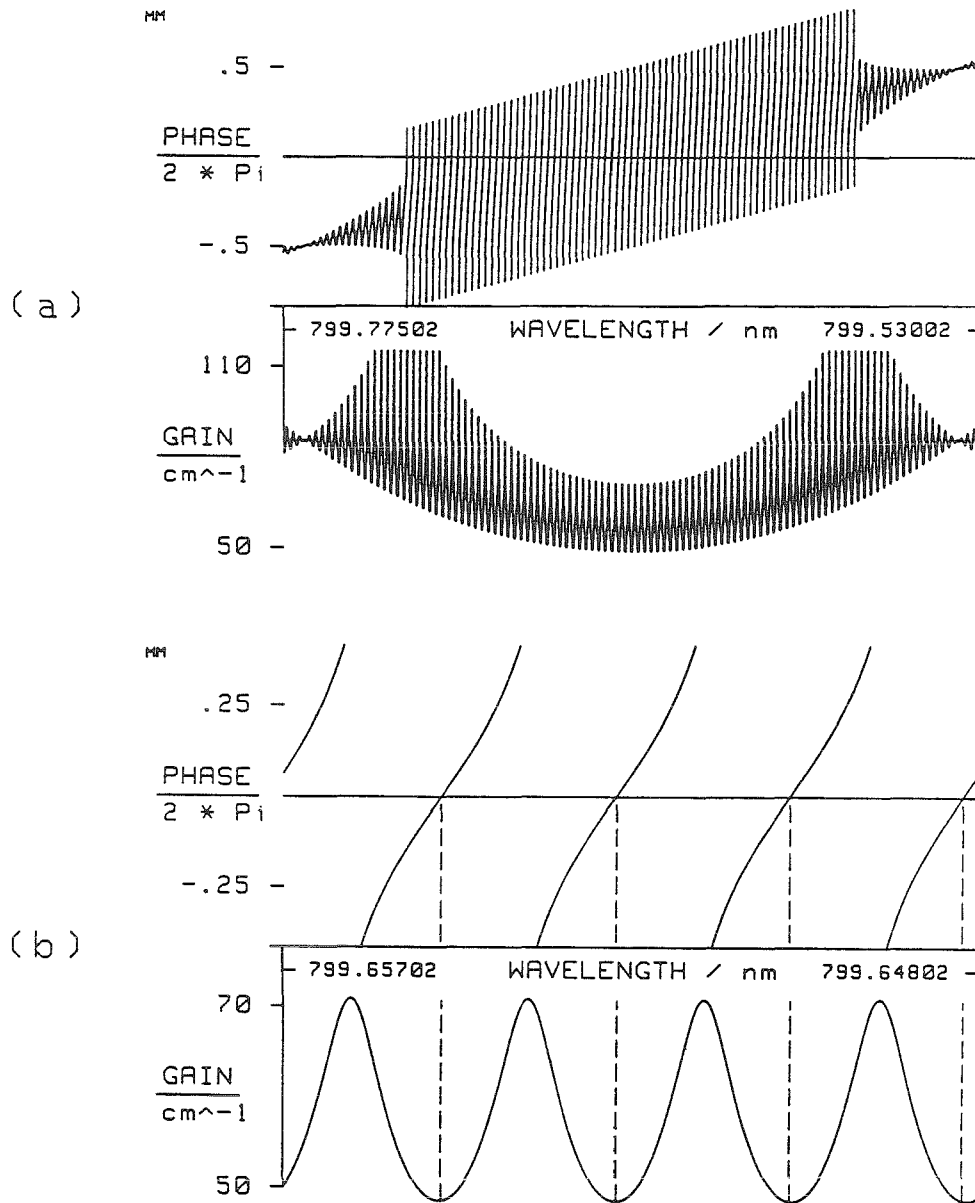
Figure 8.6 Computed phase and gain requirement of the composite-cavity laser tuned to a crystal cavity resonance similar to *Figure 8.3*. The parameters correspond to the condition of a coated laser facet ($r = 0.1$, $t = 0.26$, $L = 0.034$ cm, and $L_{ex} = 14$ cm). In (a) the wavelength selectivity of the external cavity is evident. In the range where the external cavity dominates, the direct reflection exhibits rapid continuous advance of the phase according to the external cavity leading to the $2 \cdot \pi$ discontinuities in the presentation of the phase associated with the crystal cavity. In (b) an expanded section of the spectrum is shown. The phase varies according to the external cavity.
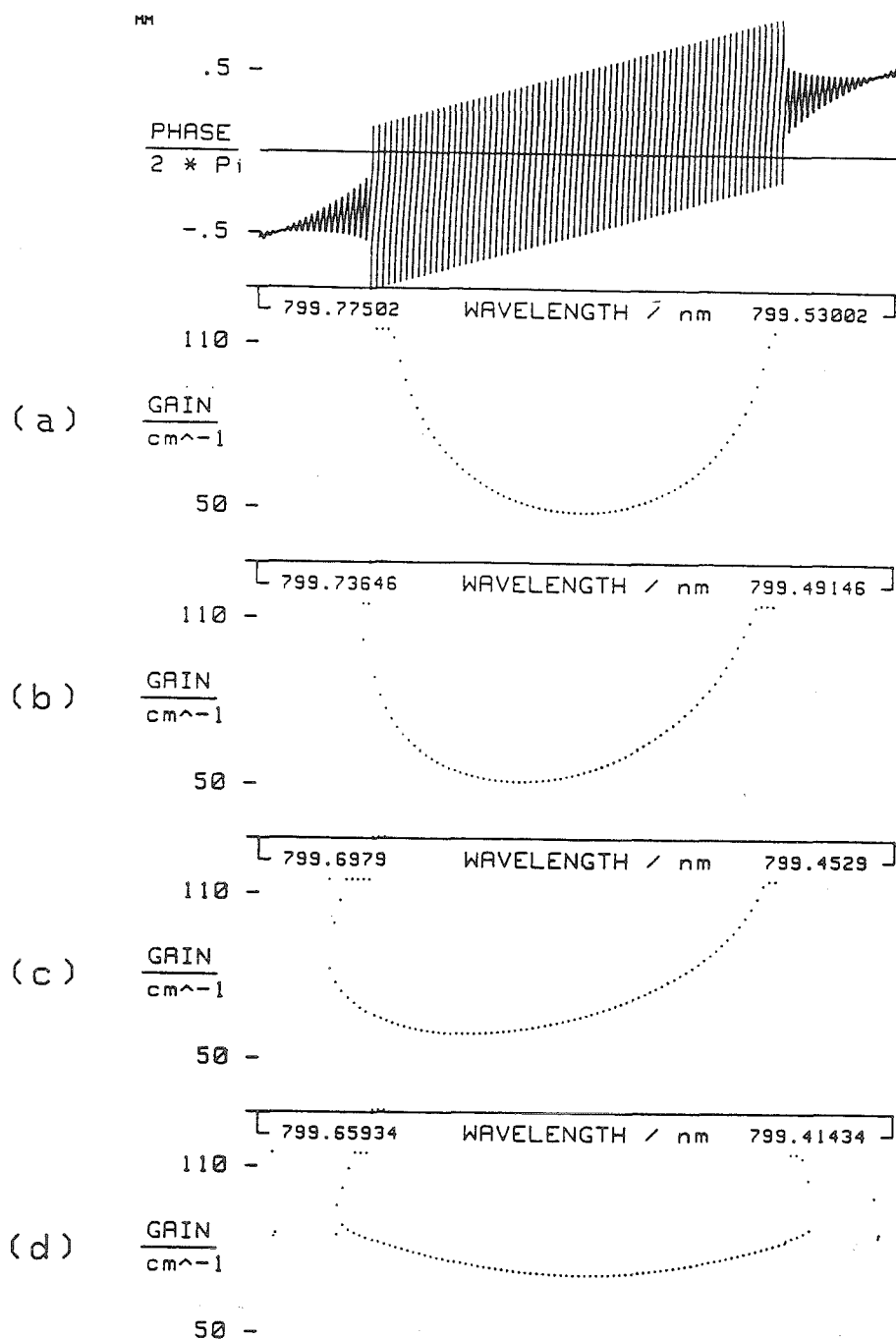
Figure 8.7 Computed gain requirement at the wavelengths around the Littrow wavelength. Case (a) corresponds to the conditions of *Figure 8.6*, while case (b), (c), and (d) correspond to a slightly shifted tuning wavelength to pick up an additional $\frac{\pi}{3}$, $\frac{2\pi}{3}$ and π phase, respectively, in the round trip of the crystal resonator. The minimum gain requirements are 48.5, 50.9, 59.1, and 70.8 $\frac{1}{cm}$, respectively. It should be noted that the minimum gain requirement in (b) and (c) are not at the Littrow wavelength.
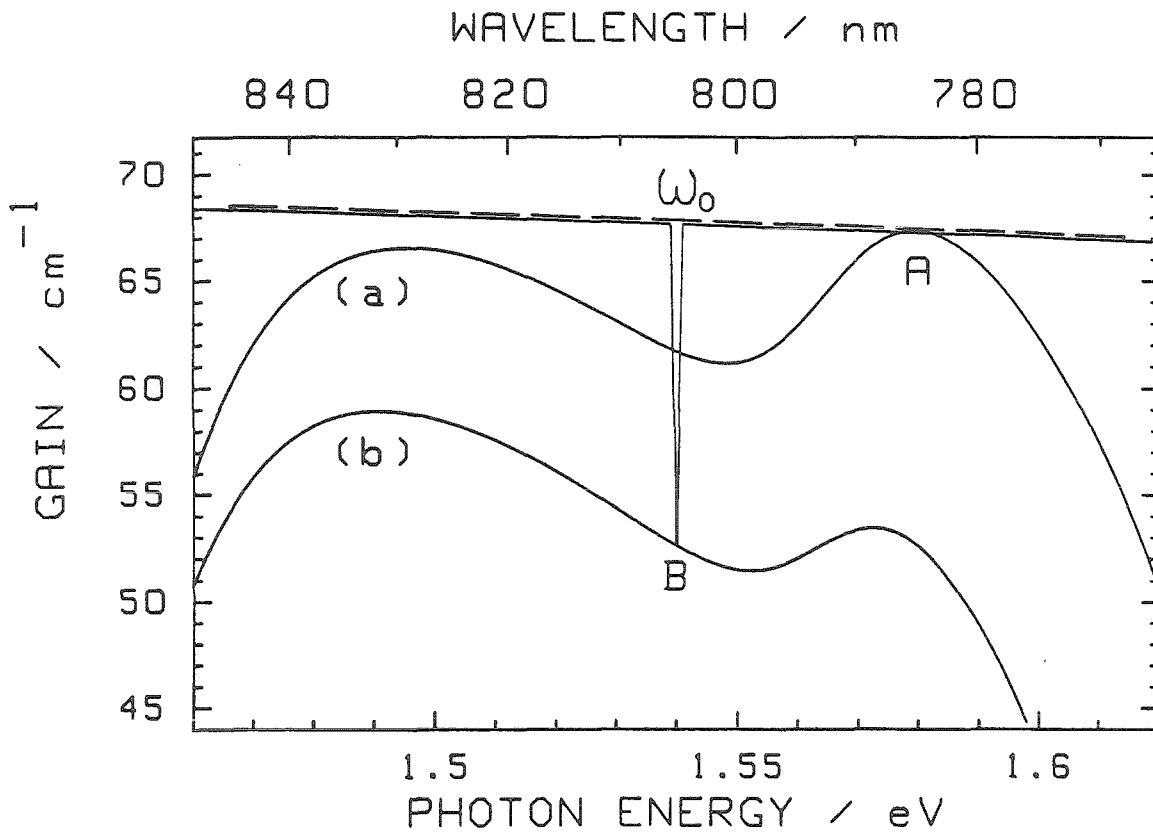
Figure 8.8 Computed minimum gain requirement for the crystal-cavity laser alone (dashed line) and the composite cavity of a grating-tuned external cavity laser (solid line). The gain spectrum (a) corresponding to free-running operation at A and the gain spectrum (b) corresponding to grating-tuned operation at B are shown. The length of the gain region is 190 μm and the structure considered is as indicated in *Figure 8.1*. The round-trip transmission used is $t(\omega_0) = 0.26$ and $\alpha_i = 4\frac{1}{cm}$.

small. *Figure 8.6* shows computed results of a composite cavity under continuous tuning conditions. The case corresponding to the in-phase condition of the crystal-cavity round trip, *Figure 8.6a*, results in a minimum gain requirement of 48.5 $\frac{1}{cm}$ of which 17.7 $\frac{1}{cm}$ are corresponding to the output coupling ($r_o^2 = 0.3$). In *Figure 8.7*, the gain requirement is shown only at the wavelengths where the phase condition is fulfilled (the cases marked by vertical dashed lines in *Figure 8.6b*). *Figure 8.7a* shows the in-phase condition as in *Figure 8.6*. *Figure 8.7 b, c,* and *d* corresponds to a slightly changed tuned wavelength, increasing the phase of the round trip in the crystal resonator by $\frac{\pi}{3}$, $\frac{2\pi}{3}$, and π, respectively. The Littrow wavelength remains at the center of the figure; however, it is not necessarily the wavelength of minimum gain requirement, thus indicating that the linear tuning is not achieved.

8.5 Width of Spectral Tuning Range

For external cavity tuning, the spectral range is determined by the coupling strength of the external cavity and the gain spectrum. Under the assumption that the laser oscillates without the external cavity, the free-running condition with its particular given wavelength is defined. *Figure 8.8* is used to explain the gain and photon energy for the free-running (A) and a grating-tuned operation (B). The dashed line shows the gain requirement of the laser with no grating feedback. In this case, the laser oscillates at a frequency corresponding to point A at a pumping level corresponding to curve (a). Addition of the external cavity tuned to ω_0 reduces the gain requirement in the cases of constructive interference, according to *Equation 8.5*. Oscillation occurs as shown in *Figure 8.8* at point B at a reduced pumping strength corresponding to curve (b). The narrow spike represents the reduction in threshold near ω_0 because of the (constructive) grating feedback. Consequently, as
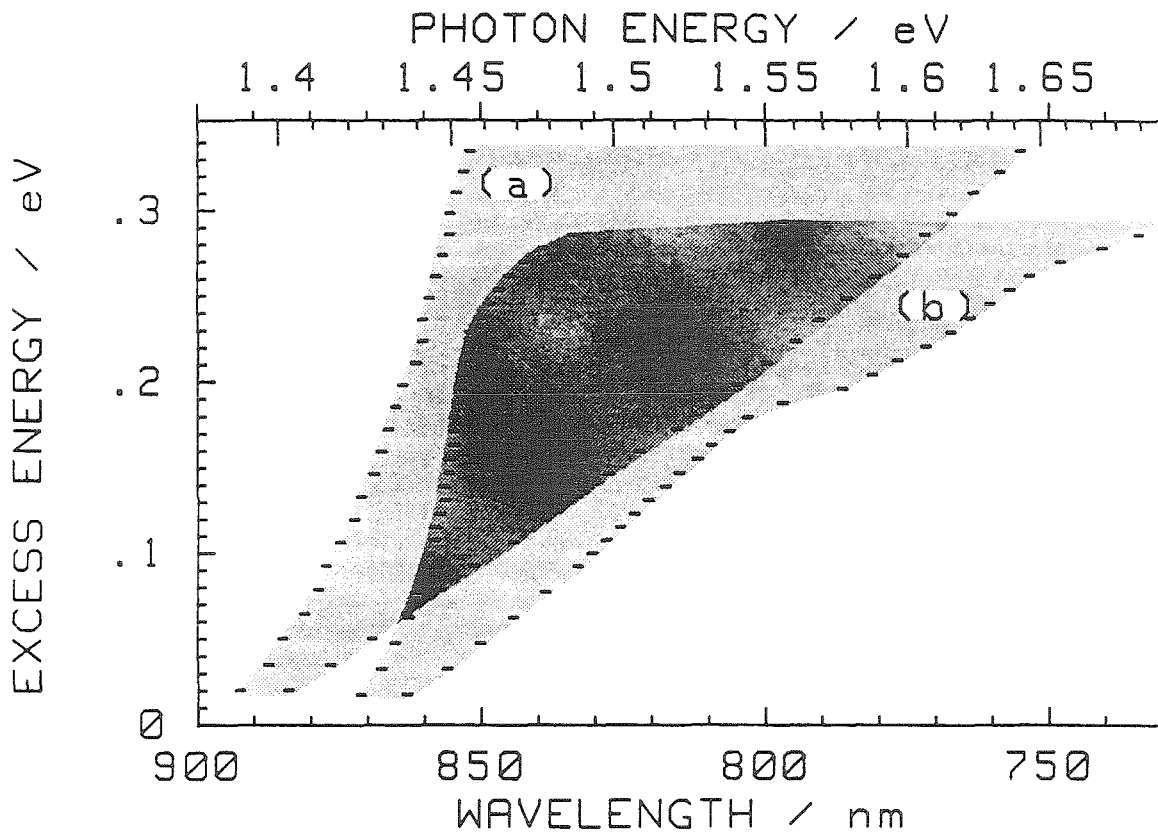
Figure 8.9 Spectral tuning range of (a) conventional double heterostructure and (b) single-quantum-well laser as a function of band filling (refer to text for explanation).

long as point B lies on a gain spectrum (b) corresponding to a reduced pumping requirement, lasing will occur at the grating-selected wavelength.

The reduction in gain requirement by the external cavity was investigated in *Sections 8.3* and *8.4* and found to depend significantly on the composite-cavity parameters; the reduction to 0.80 of the free-running condition is not demanding and is used for the following consideration concerning the tuning range in this section. Apart from a minor correction caused by the spectral dependence of the gain requirement, the tuning range is determined by the spectral width of the gain spectrum over which the gain exceeds 0.8 of the peak gain. The peak gain is in principle a function of pumping strength. If considered as the threshold of lasing, the peak gain is equal to the oscillator gain requirement and therefore depends on the resonator parameters that can be chosen in order to result in a wide range of gain requirements. The pumping strength can be characterized by several parameters: The current density is a parameter closely related to an experimental approach, and band filling is a parameter closely related to a theoretical approach. As a measure for the band filling the "excess energy" is introduced. The excess energy is defined as the sum of the quasi-Fermi energy minus the lowest confinement energy in the conduction band and the valence band. This is a parameter that is directly related to the inversion established in the gain region of the laser. Using this excess energy as a parameter, the calculated tuning ranges of a conventional double-heterostructure laser and the single-quantum-well laser (as introduced in *Figure 8.1*) are shown in *Figure 8.9*. The conventional lasers exhibit a longer wavelength operation and continuous widening of the tuning range. The quantum-well laser operates at a shorter wavelength, and the tuning range as a function of pumping strength exhibits a structure caused by the subbands of the individual quantized states. Apart from these differences, the tuning ranges of the two types of semiconductor lasers are
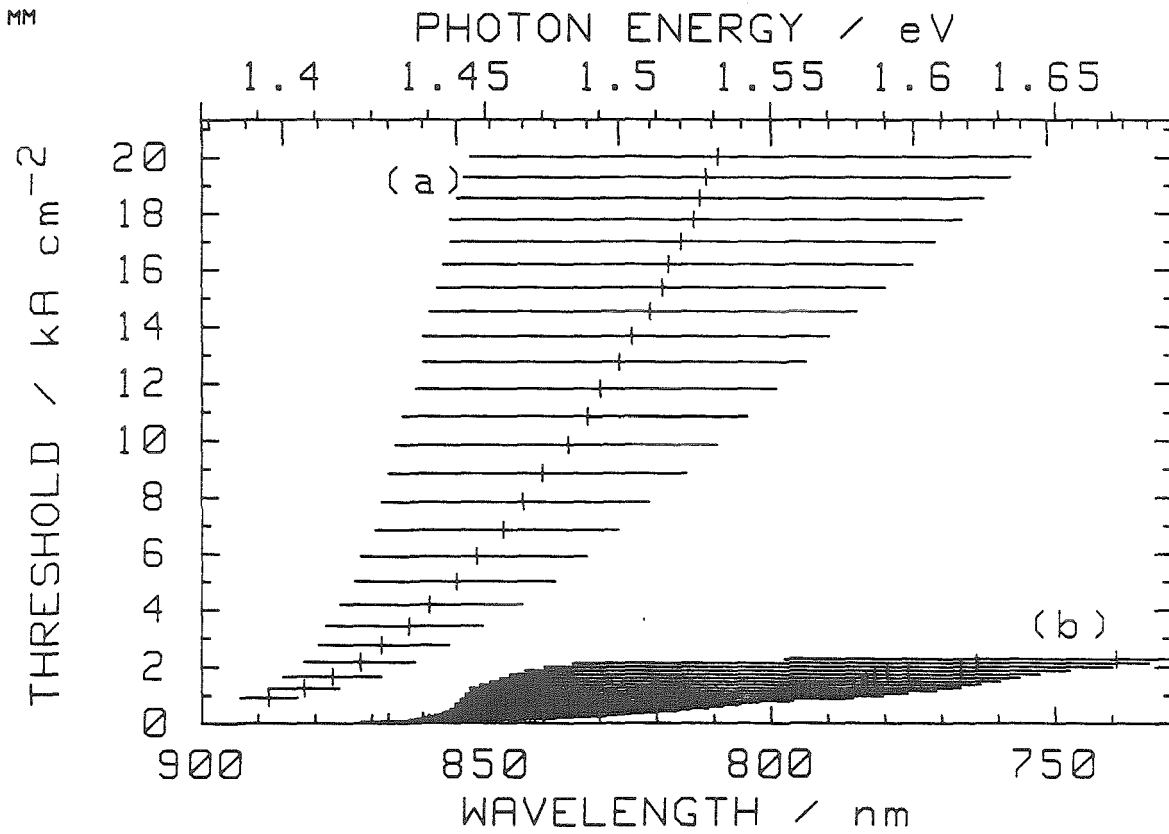
Figure 8.10 Spectral tuning range of (a) conventional double heterostructure and (b) single-quantum-well laser as a function of current density. The calculations for the quantum-well laser are terminated after the gain-flattened condition has been exceeded.

very similar indeed. In both cases, higher band filling leads to a larger tuning range, scaling approximately as 0.6 times of excess energy. The quantum-well laser exhibits only a moderately (smaller or approximately equal to 25%) larger tuning range near the gain-flattened condition. However, if the calculations are done with the current density as a parameter for the pumping strength, the quantum-well laser exhibits a superior tuning range as shown in *Figure 8.10*. At a current density of 2 $\frac{kA}{cm^2}$, which is the gain-flattened condition of the single-quantum-well structure considered, the tuning range of the single-quantum-well laser is five times as large as the tuning range of the conventional, double-heterostructure laser. On the other hand, very high-current densities in double-heterostructure lasers provide large tuning ranges together with very high gain. This very high gain allows designs with very short cavities, so that the calculated threshold current is moderate and is not much larger than the current of a single-quantum-well laser design. The practical issue is that high current densities are undesirable; it is this constraint that determines the superiority of the quantum-well laser.

8.6 Broadband Tuning Experiment

A Hänsch-type tunable laser oscillator is used for the experimental investigation: the wave-guide/air interface at the rear facet of the laser and an f/1.8 14.5 *mm* lens system form a telescope to illuminate a blazed diffraction grating in Littrow orientation. The orientation of the grating is such that the small transverse width of the wave-guide forms the selective element for the dispersed light. The spectral resolution is estimated to be a quarter of a *nm*, and is sufficient to discriminate between adjacent longitudinal modes of the short semiconductor lasers used. Power output from the laser is taken at the front facet.
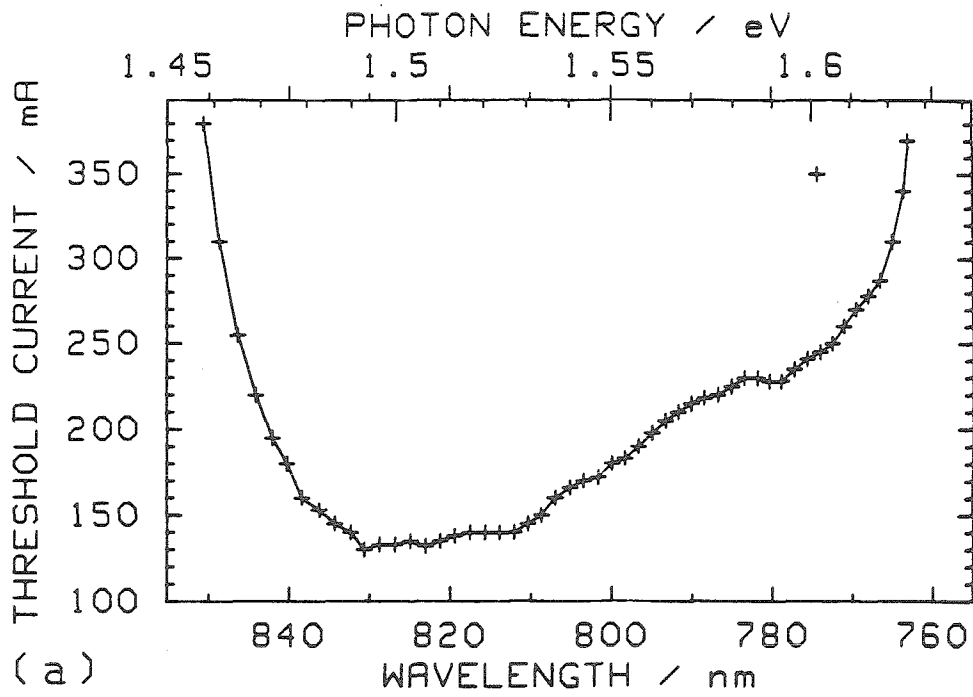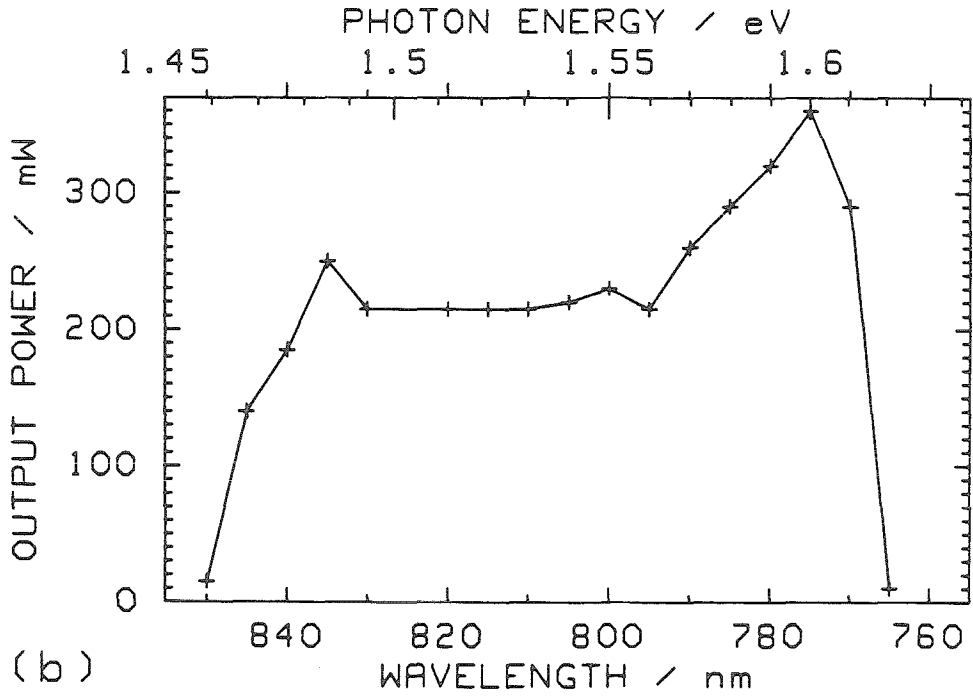
Figure 8.11 (a) Experimental spectral pump current required for threshold, and (b) resulting single-mode output power of an external-cavity, grating-tuned single-quantum-well laser.

The lasers used in the experiments are uncoated, 60 μm wide, oxide-isolated broad-area devices. They were fabricated from a linear, graded-index, separate-confinement heterostructure, single-quantum-well (GRIN SCH-SQW) wafer grown by metalorganic chemical vapor deposition (MOCVD) at Ortel Corporation. For the tuning experiment, devices were cleaved just short enough so that, free-running, they lased from the second quantized state at a wavelength near 770 nm. The total gain requirement for lasing from such 190 μm long devices is close to 65 $\frac{1}{cm}$.

Figure 8.11a shows the threshold current measured as a function of wavelength for over 200 longitudinal laser modes spanning some 85 nm. The lasers were operated pulsed (200 ns, 1 kHz) to alleviate heating. The free-running operation is indicated near 770 nm, at 330 mA. The threshold was determined as described elsewhere [9], *Chapter 5.5*. *Figure 8.11b* indicates the maximum power output as measured at the front facet for grating-tuned modes up to which single-longitudinal mode operation was maintained. Beyond that current, additional lasing was generally observed in a group of longitudinal modes near the free-running wavelength of 770 nm. Over most of the width of the tuning range, in excess of 200 mW output power were measured. Transverse electric polarization was maintained throughout all experiments.

8.7 Conclusion

The theoretical model for the gain spectrum of quantum-well semiconductor lasers was applied to conditions of relatively high pumping levels. The gain-flattened condition was described. The gain requirements for broadband tunability of such devices in an external, wavelength-selective cavity were detailed. A coupled-cavity formalism was employed to examine the necessary requirements for continuous tun-

ing. Calculations indicate that the tuning of single-quantum-well lasers and double heterostructures are very compatible in terms of band filling, but in terms of pump-current densities, the quantum-well lasers can outperform the double heterostructure by a factor of five at the gain-flattened condition.

The feature of gain-flattening in quantum-well structures is general and independent of the material in which the quantum well is constructed. Experimental evidence for the predicted broadband tunability was given: an *uncoated* single-quantum-well, broad-area laser, which emitted free running from the second quantized state, was tuned in an external cavity over a range of 85 *nm* about 800 *nm*.

8.8 References

[1]. Wyatt R., and W.J. Devlin: *"10 KHz linewidth 1.5 μm InGaAsP external cavity laser with 55 nm tuning range."* Electron. Lett. 19:110-112 (1983).

[2]. Wyatt R., K.H. Cameron, and M.R. Matthews: "Tunable narrow line external cavity lasers for coherent optical systems." Br. Telecom. Technol. J. 3(4):5-12(1985).

[3]. Epler J.E., G.S. Jackson, N. Holonyak, Jr., R.L. Thornton, R.D. Burnham, and T.L. Paoli: *"Broadband operation of coupled-stripe multiple quantum well AlGaAs laser diodes."* Appl. Phys. Lett. 47:779-780 (1985).

[4]. Mittelstein M., D. Mehuys, A. Yariv, R. Sarfaty, and J.E. Ungar: *"Broadband tunability of gain-flattened quantum well semiconductor lasers with an external grating."* Optical Society of America, Annual Meeting, Oct. 31 - Nov. 4, 1988, Santa Clara, CA, paper PD6.

[5]. Mehuys D., M. Mittelstein, A. Yariv, R. Sarfaty, and J.E. Ungar: *"Optimized Fabry-Perot (AlGa)As quantum-well lasers tunable over 105 nm."* Electron. Lett. 25(2): 143-145 (1989).

[6]. Mittelstein M., D. Mehuys, A. Yariv, J.E. Ungar, and R. Sarfaty: *"Broadband tunability of gain-flattened quantum well semiconductor lasers with an external grating."* Appl. Phys. Lett. 54(12):1092-1094 (1989).

[7]. The number of frequencies fulfilling the phase condition near each mode of the crystal cavity is about $\frac{2(1-r^2)\,t(\omega_0)\,L_{es}}{nL}$. In our experiment, the number is estimated to be 40.

[8]. Mehuys D., personal communication; December 1988.

[9]. Mittelstein M., Y. Arakawa, A. Larsson, and A. Yariv: *"Second quantized state lasing of a current pumped single quantum well laser."* Appl. Phys. Lett. 49(25):1689-1691 (1986).